

Manuscript Number: JMPG-D-17-00318R1

Title: An Enhanced Understanding of the Basinal Bowland Shale in
Lancashire (UK), through Microtextural and Mineralogical Observations

Article Type: Full Length Article

Keywords: Bowland shale; variability; micro-texture; organic matter;
fractures; microscopy; characterisation

Corresponding Author: Dr. Anne-Laure Fauchille, PhD

Corresponding Author's Institution: The University of Manchester

First Author: Anne-Laure Fauchille, PhD

Order of Authors: Anne-Laure Fauchille, PhD; Lin Ma, PhD; Ernest Rutter,
Professor; Mike Chandler, PhD; Kevin G Taylor, Professor; Peter D Lee,
Professor

Abstract: Variability in the Lower Bowland shale microstructure is investigated here, for the first time, from the centimetre to the micrometre scale using optical and scanning electron microscopy (OM, SEM), X-Ray Diffraction (XRD) and Total Organic Carbon content (TOC) measurements. A significant range of micro-textures, organic-matter particles and fracture styles was observed in rocks of the Lower Bowland shale, together with the underlying Pendleside Limestone and Worston Shale formations encountered the Preese Hall-1 Borehole, Lancashire, UK. Four micro-texture types were identified: unlaminated quartz-rich mudstone; interlaminated quartz- and pyrite-rich mudstone; laminated quartz and pyrite-rich mudstone; and weakly-interlaminated calcite-rich mudstone. Organic matter particles are classified into four types depending on their size, shape and location: multi-micrometre particles with and without macropores: micrometre-size particles in cement and between clay minerals; multi-micrometre layers; and organic matter in large pores. Fractures are categorized into carbonate-sealed fractures; bitumen-bearing fractures; resin-filled fractures; and empty fractures. We propose that during thermal maturation, horizontal bitumen-fractures were formed by overpressuring, stress relaxation, compaction and erosional offloading, whereas vertical bitumen-bearing, resin-filled and empty fractures may have been influenced by weak vertical joints generated during the previous period of veining. For the majority of samples, the high TOC (>2 wt%), low clay content (<20wt%), high proportion of quartz (>50wt%) and the presence of a multi-scale fracture network support the increasing interest in the Bowland Shale as a potentially exploitable oil and gas source. The microtextural observations made in this study highlight preliminary evidence of fluid passage or circulation in the Bowland Shale sequence during burial.

Coverletter

Harwell, 25th July, 2017

Dear Editor,

Please find enclosed a revised version of our manuscript entitled “An Enhanced Understanding of the Basinal Bowland Shale in Lancashire (UK), through Microtextural and Mineralogical Observations” by Anne-Laure Fauchille, Lin Ma, Ernie Rutter, Mike Chandler, Kevin G. Taylor and Peter D. Lee, for publication in *Marine and Petroleum Geology*.

Sincerely,

Dr Anne-Laure Fauchille

Research Associate, Research Complex at Harwell

Response to reviewer's comments, ms JMPG-D-17-00318

All remarks suggested by the reviewer 1 were considered. The whole manuscript was reformulated to be shorter, more concise and clearer, as requested.

Four co-authors are native English speakers but we verified the English language in the whole text and we are satisfied that it is of adequate standard.

The title was also reformulated to “*An Enhanced Understanding of the Basinal Bowland Shale in Lancashire (UK), through Microtextural and Mineralogical Observations*”.

Please find below the responses to comments made by each of the reviewer and the editor. Places where we have modified the text in response to the reviewer 1 are shown in yellow in the revised text.

Initial manuscript (pages, lines)	Revised manuscript (pages, lines)	Comments
3, 56	3, 8	The sentence was reformulated.
3, 59	3, 11	“diagenetic conditions” was added in the text.
3, 61	3, 12-14	The suggested additional references were added.
5, 103	5, 45 and 6, 67	Figure 1 was split in two parts (Figures 1 and 2).
6, 126-128	7, 76	This sentence was deleted.
8, 157-157	8, 102-106	The sentence was corrected and the example XRD patterns were inserted in the manuscript.
8, 164-168	8, 113-117	The numbers were corrected according to Table 1.
9, 183	10, 129-218	This sentence was deleted and the paragraph rewritten. The captions of initial Figures 3 and 4 were also reduced.
11, 198	-	The SEM images have shown that the mean clay content is very low in the Bowland Shale. The EDS analysis has detected kaolinite in the large majority of samples, but sometimes illite was also detected at a few places on SEM observations, especially in organic-rich laminae. As illite was not well-represented on the SEM images, we considered it unsurprising to have no illite on the XRD patterns due to their very low content and poor crystallinity. Ma et al., (2016) have detected both illite and kaolinite in the Bowland Shale from the Swinden borehole. The same technician and the same facilities were used to prepare the samples and to interpret the XRD patterns as used in Ma et al. (2016), so we have no doubt on the technical aspects. At to the resolution of our study, we have written “clays” in Fig. 4i to avoid any confusion.
15, 281	14, 193	Some references were added concerning feldspar alteration and quartz cementation in shale and sandstone.
17, 181-332	10, 130 to 15, 219	The 4.2 part was reduced, as required.
18, 349	17, 234-235	Some references were added.
20, 382	19, 267-268	The sentence was reworked and two references were inserted.
20, 388	19, 274-275	A few chlorite grains were present next to veins. However XRD doesn't show chlorite and illite. As we

		have no doubt concerning the veracity of the XRD results and the technical work, and as these samples are very heterogeneous, we suggest that the heterogeneity can account for variations in the powders done for the XRD measurements for the sample B5 and B8 (interlaminated and laminated samples).
22, 411	20, 292	This sentence was deleted to shorten the manuscript.
22, 424	21, 303	Some references were added.
29, 537-537	28, 413-414	The expressions were moved as required.
29, 541	29, 417	The sentences were reworked.
30, 552-555	28, 427-429	
30, 570	29, 444	
31, 579	29, 453-454	Some references were inserted.
32, 621	31, 493-499	The paragraph 5.4 was reworked to be clearer.
34, 656	33, 537-539	Some references were inserted.
36, 707	35, 588	The beginning of the sentence was reworked. The expression “studied here” can also be used.
36, 716-717	35, 598-624	The whole paragraph on fracture orientation was reworked to be clarify the manuscript.
37, 748	36, 628	The beginning of the sentence was changed.
39, 793	39, 1	The references indicated by the reviewer 1 were added.

The variability of the Bowland shale microstructure was studied for the first time.

There is a high variability of microtextures, organic-matter particles and fractures.

The majority of samples have high TOC, low clay content and high quartz content.

The observations highlight preliminary evidence of fluid passage in Bowland shale.

It supports interest in the Bowland shale as an exploitable oil and gas source.

**An Enhanced Understanding of the Basinal Bowland Shale in Lancashire (UK),
through Microtextural and Mineralogical Observations**

A. L. Fauchille^{1,2*}, L. Ma¹, E. Rutter³, M. Chandler³, P. D. Lee^{1,2} & K. G. Taylor³

¹Manchester X-Ray Imaging Facility, School of Materials, the University of Manchester, Oxford
Road, Manchester M13 9PL, UK.

²Research Complex at Harwell, Rutherford Appleton Laboratory, Didcot Oxon OX11 0FA, UK.

³School of Earth and Environmental Sciences, The University of Manchester, Oxford Road,
Manchester, M13 9PL, UK.

*Corresponding author : al.fauchille.research@gmail.com

Abbreviated title: Microtextural observations of Bowland Shale

Keywords : Bowland shale, variability, micro-texture, organic matter, fractures, microscopy,
characterization

Submitted to Marine and Petroleum Geology

Re-submission in July, 2017

15 Abstract

1
2 16 Variability in the Lower Bowland shale microstructure is investigated here, for the first time, from
3
4
5 17 the centimetre to the micrometre scale using optical and scanning electron microscopy (OM, SEM),
6
7 18 X-Ray Diffraction (XRD) and Total Organic Carbon content (TOC) measurements. A significant
8
9
10 19 range of micro-textures, organic-matter particles and fracture styles was observed in rocks of the
11
12 20 Lower Bowland shale, together with the underlying Pendleside Limestone and Worston Shale
13
14
15 21 formations encountered the Preese Hall-1 Borehole, Lancashire, UK. Four micro-texture types were
16
17 22 identified: unlaminated quartz-rich mudstone; interlaminated quartz- and pyrite-rich mudstone;
18
19 23 laminated quartz and pyrite-rich mudstone; and weakly-interlaminated calcite-rich mudstone.
20
21
22 24 Organic matter particles are classified into four types depending on their size, shape and location:
23
24 25 multi-micrometre particles with and without macropores: micrometre-size particles in cement and
25
26 26 between clay minerals; multi-micrometre layers; and organic matter in large pores. Fractures are
27
28
29 27 categorized into carbonate-sealed fractures; bitumen-bearing fractures; resin-filled fractures; and
30
31
32 28 empty fractures. We propose that during thermal maturation, horizontal bitumen-fractures were
33
34 29 formed by overpressuring, stress relaxation, compaction and erosional offloading, whereas vertical
35
36 30 bitumen-bearing, resin-filled and empty fractures may have been influenced by weak vertical joints
37
38
39 31 generated during the previous period of veining. For the majority of samples, the high TOC (>2
40
41 32 wt%), low clay content (<20wt%), high proportion of quartz (>50wt%) and the presence of a multi-
42
43 33 scale fracture network support the increasing interest in the Bowland Shale as a potentially
44
45 34 exploitable oil and gas source. The microtextural observations made in this study highlight
46
47
48 35 preliminary evidence of fluid passage or circulation in the Bowland Shale sequence during burial.
49
50
51
52
53
54
55
56
57
58
59
60
61
62
63
64
65

1. Introduction

Characterization of the properties of shales is an essential process in the estimation of their gas and oil resource potential. Important shale gas and oil resources are believed to exist in Western Europe (EIA 2013) and in particular in the UK (EIA 2015a). In order to understand and quantify the properties of this potential resource, the geology of the Bowland and Hodder mudstone formations has been investigated throughout the last decades at the basin-scale (Gawthorpe 1987; Davies et al. 1989; Hampson et al. 1997; Fraser & Gawthorpe 2003; Waters & Davies, 2006; Davies et al. 2008; Waters & Condon 2012; Andrews 2013), and more recently at the nanometre scale (Ma et al. 2016). In general, the most commonly investigated properties of shale have been the lithology, sedimentary architecture, total organic matter carbon content (TOC), kerogen type, thermal maturity and oil and gas expulsion potential, the mineralogical composition, diagenetic conditions and the presence of natural fracture networks (Curtis 2002; Rossi et al., 2002; Montgomery et al. 2005; Jarvie et al. 2007; Ross & Bustin 2007, 2008; Perri, 2008; Carraciolo et al., 2013; Jarvie 2014; Abrams et al. 2014; Raji et al. 2015; Perri et al., 2008, 2016). The evaluation of shale resources is complicated because of the heterogeneous nature of the fine-grained strata and their intricate, small-sized pore networks, which are strongly dependent on the above geological factors (Yang & Aplin, 1998; Dewhurst et al. 1999a, b; Ross & Bustin 2007; Chalmers & Bustin 2007; Mckernan et al. 2017). From the millimetre to the nanometre scale, shale gas is stored as free gas in natural fractures, within both intergranular and intra-granular porosity and adsorbed onto kerogen and clay-particle surfaces. It may also be dissolved in kerogen and bitumen (Curtis 2002). The microstructure directly influences the distribution of gas and its transport properties through the porous network. Knowledge of the microstructure of shale is consequently required. However, there is still a very limited understanding of the processes giving rise to pore networks, fractures, and organic and mineral properties in British Shales. In particular, data are sparse for the Bowland and Hodder Shales, despite forming an important potential oil and gas resource. Detailed

petrographic studies of these shales are required to allow a better comparison with other shale formations, especially the relatively well understood shale reservoirs from northern America. The major goal of this study is to present the first multi-scale (centimetre to micrometre) and petrologic characterization of the different microtextures of Bowland shale encountered in the Preese Hall-1 borehole, a significant and recent exploration borehole in Lancashire, NW England, using optical and scanning electron microscopy in combination with XRD and TOC analysis. Due to the coarse resolution of sampling within our study, we recognize that potential stratigraphic variability between samples implies that microtextures other than those identified in our study could potentially be present within the borehole.

2. Geological Settings and Sampling

In this study, eleven centimetric-sized samples of mudstone were collected from the Preese Hall-1 borehole core repository at the British Geological Survey (Nottingham, UK). Preese-Hall-1 is situated in the Carboniferous basin Bowland Shale Formation, which extends across a large part of central Britain (Fig. 1). Drilling of the Preese Hall-1 borehole was initiated in August 2010. It is situated on the Fylde coast of NW Lancashire at 53° 49' 19.006"N; 2° 56' 56.576 W", near to Blackpool, north-west England.

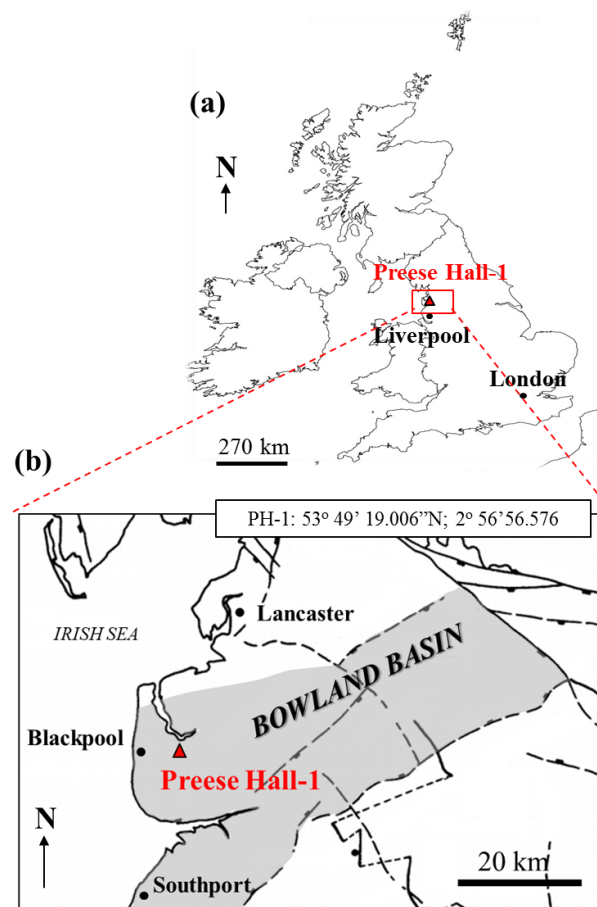


Fig. 1. Location of the Preese Hall-1 borehole in: (a) the United Kingdom and (b) the Bowland Basin (adapted from Evans & Kirby 1999; mapsofworld 2015).

Preese Hall-1 is the first dedicated unconventional shale gas borehole in the UK and Europe (de Pater & Baisch 2011), and was drilled to a depth of 2745 meters. Preliminary hydraulic stimulations of this borehole were performed by Cuadrilla Resources Ltd in 2011 (Eisner et al. 2011; de Pater & Baisch 2011; Clarke et al. 2014).

Within the Bowland basin, the rocks of the Bowland-Hodder group encountered in the Preese Hall-1 borehole are divided into an upper unit characterised by some 150 m of shale (Upper Bowland Shale) and a lower, more variable unit (Lower Bowland Shale) containing almost 500 m of shale interbedded with clastic and carbonate deposits due the influence of glacio-eustatic sea level changes and tectonic events (Gawthorpe 1987; Andrews 2013). The Bowland Shale Formation

(Upper and Lower Bowland shales) corresponds to ages between the end of the Visean (Brigantian) and the beginning of the Namurian (Pendleian) (Waters et al. 2009) (Fig. 2). The Pendleside Limestone Formation lies below the Bowland Shale Formation and marks the bottom of the Bowland Shale sequence (Waters et al. 2009). Beneath, the Worston shale group forms a further 150 m thick unit of shales. The top of the Bowland shale group passes into the Millstone Grit Group (Pendleian). The Bowland shale, Pendleside limestone and Worston shale are all included in the Bowland-Hodder Unit corresponding to the whole Visean period (Andrews, 2013).

The samples used for the present study were taken predominantly (Fig. 2) from the lower Bowland Shale Formation (samples B1 through B10). Sample B11 was taken from the Pendleside limestone Formation and B13 from the lower part of the Worston Shale Formation (there is no B12).

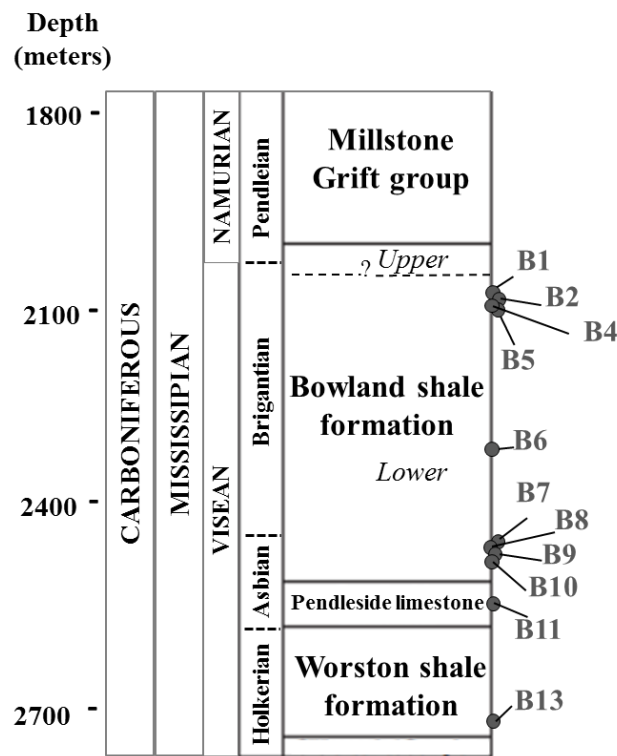


Fig. 2. Bowland basin stratigraphy in the Preese Hall-1 borehole, showing the stratigraphic locations of the samples studied, which lie within the Bowland-Hodder group.

In general, the organic content of the Bowland Shales lies between 1 and 3 wt% (Spears & Amin 1981; USEIA 2011), but can reach 5-8% (iGas 2012; Andrews 2013; EIA 2015).

3. Material Preparation and Methods

The mineralogy of all samples was semi-quantified by X-Ray diffraction (XRD) on a Bruker D8 Advance diffractometer, equipped with a Göbel Mirror and Lynxeye detector. The X-ray tube provided $\text{CuK}_{\alpha 1}$ X-rays with a wavelength of 1.5\AA . Sample preparation involved grinding $\sim 0.1\text{g}$ of sample material mixed with $\sim 1\text{ml}$ of amyl acetate. Samples were scanned between 5 and $70^\circ 2\theta$, with a step size of 0.02° and a count time of 0.2s per step.

Total organic carbon (TOC) was measured with an experimental uncertainty of $\pm 0.02\%$ TOC using 100 mg powder samples in a Leco carbon analyzer (Michigan, United States) at the University of Newcastle (UK), after rock acidification and organic matter combustion.

All samples were vacuum impregnated with epoxy resin and mechanically polished as thin sections for optical and scanning electron microscopy. Optical microscopy was performed using an Olympus SZX16 stereomicroscope to obtain low magnification images of the general textures from cm- to mm-scale . Low magnification observations were also made with a JEOL JSM 6610LV SEM equipped with a back-scattered electron detector and semi-quantitative EDS analyser. The accelerator voltage was 20 kV and the working distance 10mm . To confirm the nature of minerals, EDS point analysis and mapping was used with AZtec© software. High magnification observations were performed with a SEM FEI Quantax FEG 650, with an accelerator voltage of 10 kV . Apart from macropores, pore types are not described here because of the resolution of the study. The differentiation between impregnation resin and organic matter under SEM was achieved using a combination of three criteria:

- (a) the morphology: organics have smooth faces at boundaries, whereas resin has clear boundaries with the material due to its viscosity. The resin contains clear cracks at some places, formed by the local heating by the electron beam at high energy (20 kV).

(b) the peak intensity of carbon in EDS analysis. In our case, the organic matter particles show a peak of carbon for energy much higher than 15 cps.eV^{-1} , in contrast to the resin.

(c) the presence of chloride. Araldite 2020 resin contains a few percent of chloride which is enough to be detected by EDS, in contrast to organic particles.

The small sizes of the samples available for this study precluded the measurement of bulk porosity and permeability.

4. Results

4.1. Bulk composition and TOC

The samples are mainly composed of quartz, calcite, ankerite, muscovite, kaolinite, albite and pyrite, based on XRD quantification (Table 1, Fig. 3). Two examples of the XRD patterns are given in Fig. 3. These mineral assemblages determined by XRD were confirmed by SEM observations, especially for clay minerals.

				Proportions (wt%)								
				Kaolinite	Quartz	Calcite	Ankerite	Pyrite	Muscovite	Albite	TOC	
Samples Depth (meters) Facies												
Bowland-Hodder unit	Lower Bowland shale	B1	2073.34	Unlaminated quartz-rich	0	58	15	13	2	9	3	1.4
		B2	2081.27	Transition un- to interlaminated quartz-rich	5	53	17	1	8	11	5	4.1
		B4	2089.83	Unlaminated quartz-rich	5	65	4	5	4	11	6	1.7
		B5	2091.69	Interlaminated quartz-rich	6	56	12	6	6	10	4	3.2
		B6	2344.70	Unlaminated quartz-rich	7	71	6	2	1	10	3	6.1
		B7	2488.84	Interlaminated quartz-rich	3	68	10	3	2	10	4	1.5
		B8	2495.27	Laminated quartz-rich	18	52	3	11	2	5	9	1.1
		B9	2496.92	Unlaminated quartz-rich	6	52	21	3	5	9	4	2.1
		B10	2500.49	Unlaminated quartz-rich	5	56	18	1	5	10	5	2.0
	P.L ¹	B11	2586.29	Unlaminated Calcite-rich	1	23	69	2	1	2	2	0.5
W.S ²	B13	2710.40	-	5	73	6	0	1	11	4	5.6	

Table 1. Mineral proportion obtained by X-Ray Diffraction and Total Organic Content measurements for all samples (1 : Pendleside limestone, 2 : Worston shale)

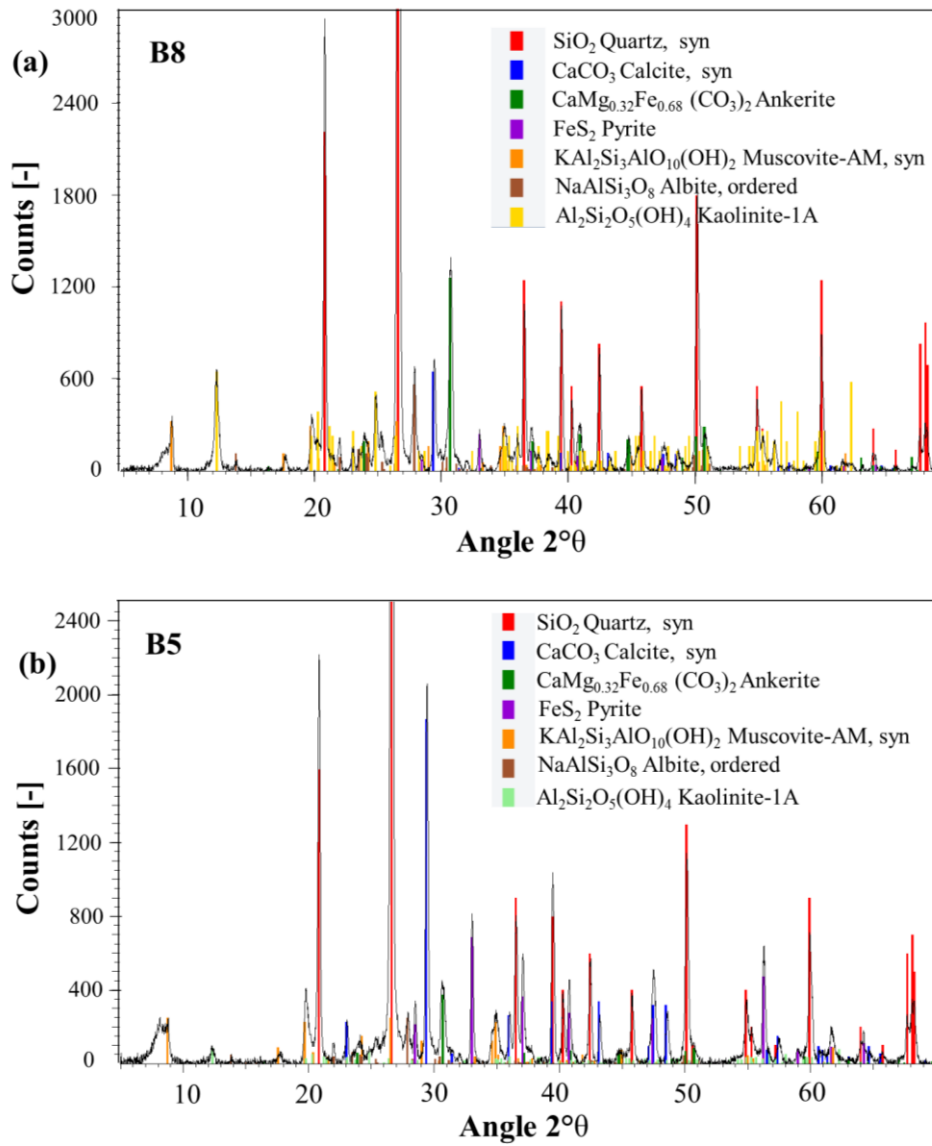


Fig. 3. XRD patterns corresponding to the samples (a) B8 and (b) B5.

All Bowland-Hodder mudstone samples in this study are quartz-rich (>50 wt%) and clay-poor (<20 wt%) in contrast to sample B11, which is calcite-rich (>68wt%) (Table 1). Kaolinite is the only clay mineral detected by XRD across all of the samples. The proportion of kaolinite is very low (<7 wt%) for all samples except B8 (18 wt%). Except for sample B11, all shale samples also contain various proportions of carbonates (from 6 to 71 wt%), such as calcite and ankerite. Quartz and calcite are also the most variable phases, with the least variation being seen in clay minerals (except B8 with 18 % of kaolinite), muscovite, albite and pyrite (Fig. 4a).

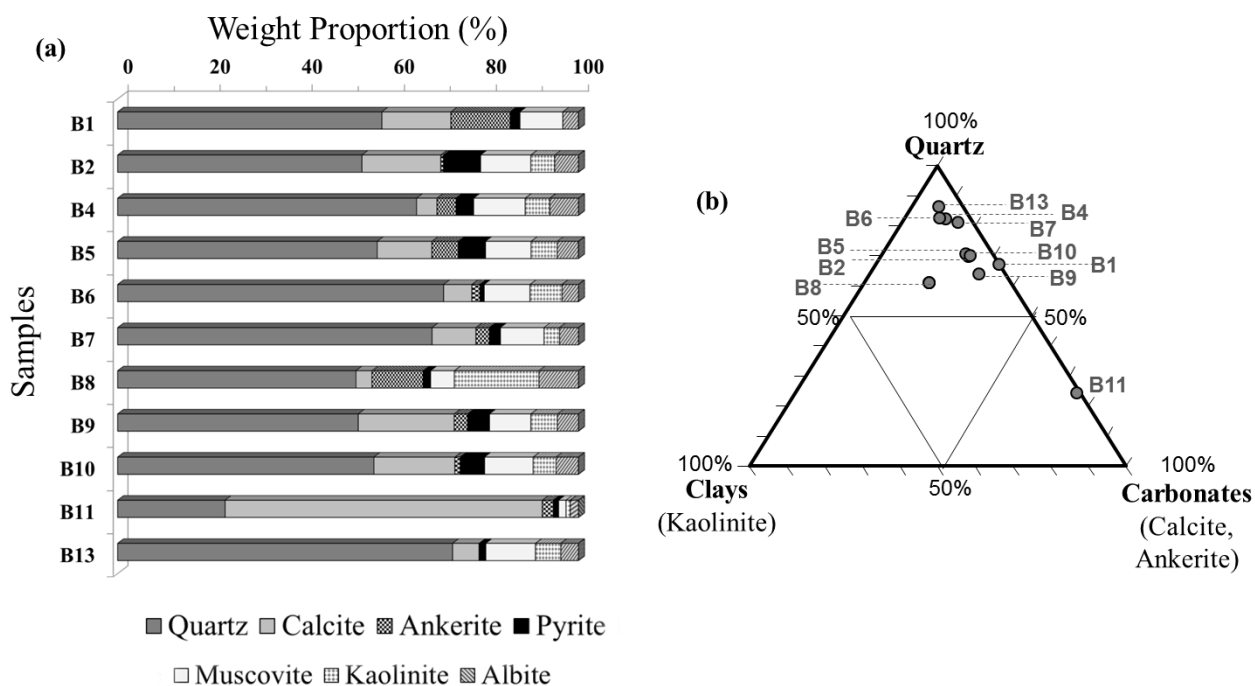


Fig. 4. (a) Variability of mineralogical composition of all samples, and (b) Mineralogy of all samples represented on a ternary diagram plotting proportions of clays, quartz and carbonates.

Despite the variation in mineral proportions (Fig. 4a), all shale samples display quartz-rich and calcite-rich mineralogies, independently of their TOC (Fig. 4b). The TOC values vary from 0.5 to 6.1 wt% for all the shales and the majority of samples have a TOC higher than 2 wt%, which is usually considered the lower level for potential oil and gas plays (Table 1) (Charpentier & Cook 2011). The TOC measurements were performed on centimetre-scale samples and are mean measurements, therefore local variability of organic matter content at smaller scales cannot be excluded.

4.2. Textural variability at the cm to μm scale

Micro-texture types were defined according to the thin section observations, on the basis of (a) the absence or presence of laminae, (b) lamina thickness, (c) grain type (mineralogy), (d) grain properties (e.g. size, orientation) and (e) the structure, content and nature of organic matter particles. Four main types were defined: unlaminated quartz-rich mudstone (type 1), interlaminated

quartz-rich mudstone (type 2), laminated quartz-rich mudstone (type 3) and weakly interlaminated calcite-rich mudstone (type 4). For each micro-texture type, one sample was selected to illustrate the microstructure. At the centimetre scale, the samples present various colors such as dark (B6), light to dark grey (B11, B1, B5, B8) or dark brown (B2), principally reflecting their organic matter contents (Fig. 5).

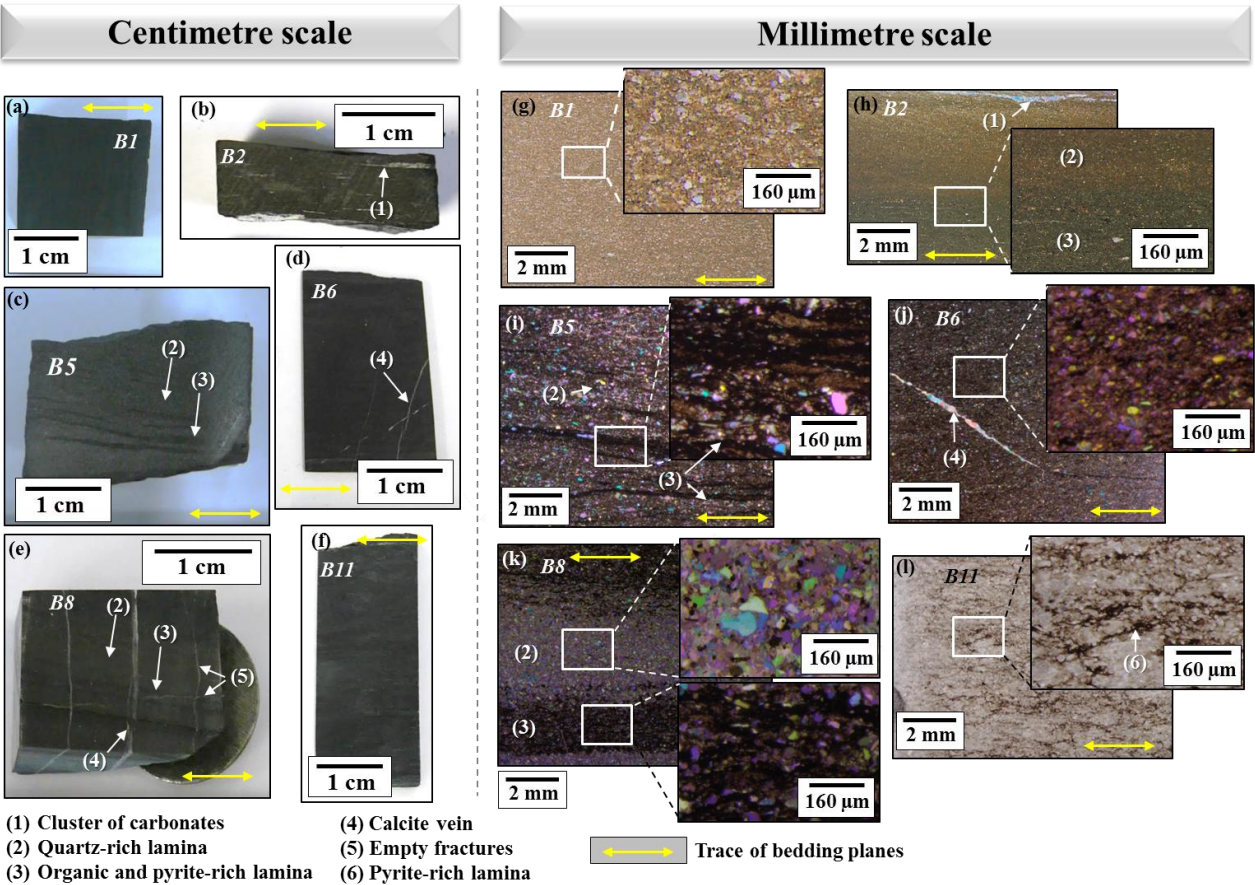


Fig. 5. Variability of mudstone micro-texture types of Bowland Shale from at the cm and mm scales : macroscopic views (a-f) and optical images (g-l).

The samples show variations of texture due to the presence of laminae (B5, B8), fractures sealed by carbonates (B6, B8), carbonate and quartz clusters (B2), and brittleness with open fractures (B8).

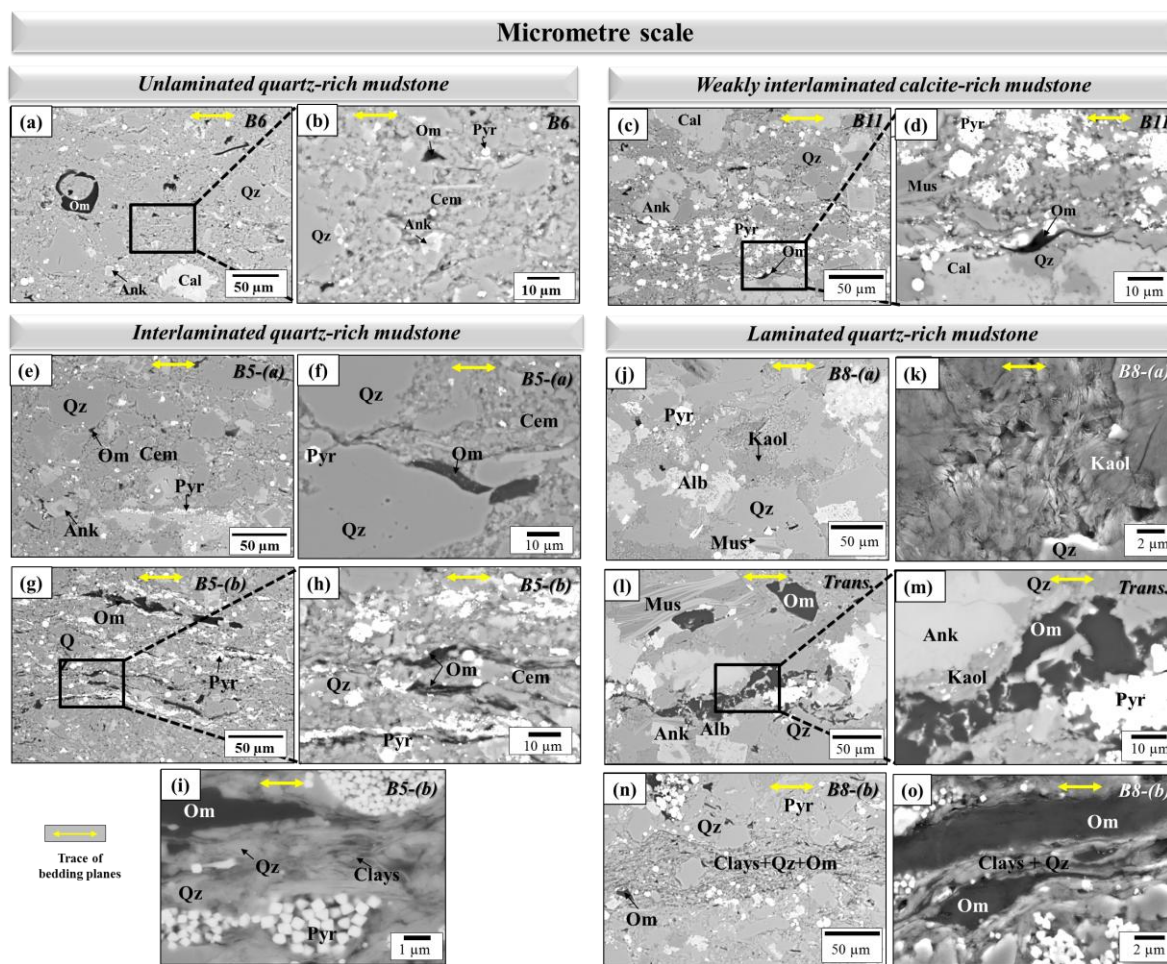


Fig. 6. Variability of mudstone micro-texture types of Bowland Shale at the μm scale by back-scattered electron (BSE) images under SEM : (a,b) unlaminated quartz-rich mudstone, (c,d) weakly interlaminated calcite-rich mudstone, (e-i) interlaminated quartz-rich mudstone, (j-o) laminated quartz-rich mudstone. [Cal: calcite, Qz: quartz, Ank: ankerite, Om: organic matter, Qz: quartz, Pyr: pyrite, Cem: cement, Kaol: kaolinite, Alb: albite].

Micro-texture type 1: Unlaminated quartz-rich mudstone (Samples B1 and B6)

Sample B6 forms a homogeneous unit from the centimetre to the millimetre scales. Calcite veins are present in B6 (Figs 5 d, j and 6 a, b). From the mm to μm scales, the grains of quartz and carbonates are dispersed within a fine crystalline quartz cement. The sizes of clastic grains vary from 10 μm to 50 μm in diameter. The quartz grains are in contact, unlike the carbonates and other grains. They are rounded with irregular shape, in contrast to the ankerite and muscovite grains

which are idiomorphic (Fig. 6 a, b). This micro-texture type contains mainly lithoclasts and does not possess any bioclasts. Quartz grains are divided in two types: the primary quartz in the lithoclasts, which probably results from the deposition of sediment, and the secondary quartz included in the cement and which fills in holes in carbonate grains and organic matter. The organic matter particles are randomly located at the mm scale (Fig. 6b). They are mainly micrometre-scale isolated particles and submicron particles mixed in the cement at the μm scale. Clay minerals (kaolinite) are located between the micrometre grains of quartz in the cement.

Micro-texture type 2: Interlaminated quartz-rich and pyrite-rich mudstone (B5, B2, B7)

At the centimetre scale, the interlaminated quartz-rich mudstone (Fig. 5 e-i) is heterogeneous due to the presence of periodic laminae, and the variation of their thickness and continuity. Two types of laminae are identified: (B5-a) grey quartz-rich lamina of millimetric thickness, and (B5-b) black organic and pyrite-rich lamina of around $100\ \mu\text{m}$ thickness. The thickness of quartz-rich laminae is up to ten times that of the organic-rich laminae.

In B5-a (Fig. 6 e, f), the grains of quartz and carbonate display very various sizes (up to $100\ \mu\text{m}$). Quartz is particularly well-rounded and equant, unlike calcite which shows irregular shapes. Quartz and ankerite do not exhibit any evident shape preferred orientation. The largest calcite ($>50\ \mu\text{m}$) and muscovite grains are elongate and oriented parallel to the bedding planes. The grains are held in a fine quartz cement in which detrital quartz grains are contiguous. Pyrite grains occur in randomly located framboid structures, with some assembled inside and/along the boundaries of calcite grains, parallel to bedding. The cement appears organic matter-poor at the μm scale.

In B5-b (Fig. 6 g-i), the grains of quartz and carbonates have qualitatively similar properties in terms of shape and orientation as B5-a, but their size is significantly smaller (around $10\ \mu\text{m}$). The pyrites are assembled into framboids which form dense and elongate layers hundreds of μm long, and lying parallel to the bedding planes. These assemblages of pyrite are interlaced with elongate micrometric organic matter particles, confirmed by their opacity under crossed polars OM (Fig. 5i).

Many submicron and elongate particles of organic matter are interlaced with submicron grains of quartz and clay minerals (Fig. 6 h, i).

Micro-texture type 3: Laminated quartz-rich mudstone (B8)

From the cm to the mm scales, the laminated quartz-rich mudstone is heterogeneous due to the presence of millimetre-size periodic laminae (Figs 5 e, k and 6 j-o). The laminae are quartz- (B8-a) and organic-rich (B8-b) but their mineralogy is different than the samples B6 and B5, previously described. These laminae are intersected by ankerite and calcite veins that cross-cut the bedding (Fig. 5j). The transition between laminae is progressive or sharp, which could be interpreted as gradual and rapid changes of depositional conditions, respectively.

B8-a is composed of large grains of quartz, feldspars (albite), muscovite, ankerite, calcite and framboidal pyrites. B8-a is strictly a siltstone and lithologically close to a sandstone, with grains of quartz and feldspar with a mean diameter between 50 and 100 μm , within a fine cement of quartz (Fig. 6j). Albite is altered and replaced by kaolinite, and filled by quartz cement, which suggests that this type of quartz is probably diagenetic (Bjorlykke and Egeberg, 1993; Schieber, 1996). B8-a contains large amounts of crystalline kaolinite (with no particular orientation), mixed with quartz and calcite grains in the cement (Fig. 6k). A few idiomorphic ankerite grains are present on and in replacement of calcite in veins. The organic matter is dispersed as submicron particles in the quartz cement, and in micrometric particles on pyrite boundaries. B8-a is organic-matter poor over the mm to μm scales. The concentration of large particles of organic matter increases in the transition of B8a to B8b (Fig. 6 l,m).

B8-b forms a heterogeneous unit with a lower mean quartz grain size ($<30 \mu\text{m}$), and multiple sizes and aspects of organic matter particles (Fig. 6 n, o). B8-b is feldspar-poor. The organic matter particles are present as very large (up to 100 μm) and elongate particles in the cement, orientated parallel to the trace of bedding, and as submicron particles between clay minerals (Fig. 6 n,o). The

clay minerals are arranged into localized and discontinuous elongate lenses approximately 50 μm thick.

Micro-texture type 4: Weakly interlaminated calcite-rich mudstone (B11)

At the cm scale, the weakly interlaminated calcite rich micro-texture type looks homogeneous (Fig. 5f). However, from the mm to the μm scales, irregular and discontinuous laminae are observed: (B11-a) calcite-rich laminae, and (B11-b) pyrite-rich laminae (Fig. 6 c, d). B11-a lamella are approximately millimetre thick and mainly composed of detrital calcite, authigenic calcite cement, ankerite, quartz and pyrite (Fig. 6 c, d). A small amount of clay minerals (kaolinite, but illite was also detected) is also present between the calcite and quartz in the cement. A few submicron organic matter particles are present in the cement without any preferential orientation at the μm scale. B11-b is composed of pyrite, phyllosilicates, quartz cement and orientated submicron-sized organic matter particles parallel to the trace of bedding. The framboidal pyrites form elongate and discontinuous layers, also aligned along the bedding trace with thicknesses varying from a few tens of μm to 100 μm . The quartz grains are divided into roughly equidimensional rounded grains and cement which fills the interstices between calcite grains.

4.3. Characterization of organic matter particles

An inventory of the different types of organic matter particles is shown in Figure 7.

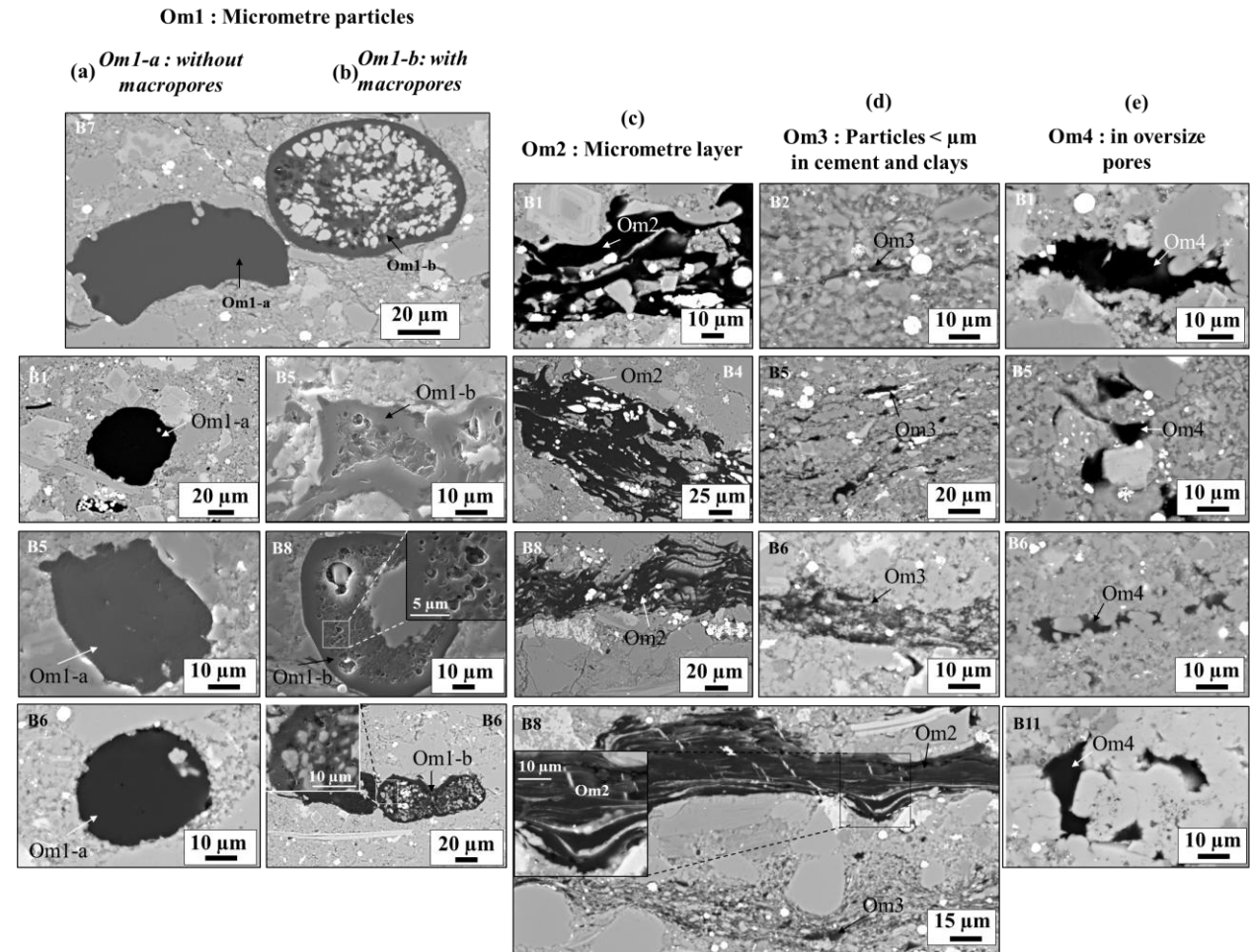


Fig. 7. Various types of organic matter particles in Bowland shale under SEM: (a) micrometric particles of organic matter without macropores (Om1-a); (b) micrometric particles of organic matter with macropores (Om1-b); (c) micrometric layers of organic matter (Om2); (d) Sub-micrometric organic matter particles in cement (Om3); (e) organic matter in oversize pores.

In the range of all mudstone samples, the organic matter particles are divided into four main types, as a function of their size and shape, the presence of macropores and their location:

Om1: micrometric particles. These particles are divided in two sub-types according to the presence or absence of macropores: Om1-a are organic matter particles of micrometric size and mainly equant and rounded, without macropores at the μm scale (Fig. 7a), and Om1-b which are organic matter particles of generally more than 10 μm size, with random shape and macropores at the μm scale (Fig. 7b). They are partially cemented by quartz and calcite. Their shapes and the

presence of macropores suggest that they probably result from primary deposits of algal cysts (Leckie et al., 1990; Schieber, 1996). Om1-b pores are filled by diagenetic quartz (Schieber et al., 2000).

Om2: micrometre layers (Fig. 7c). Om2 is structured in dense layers (20-200 µm) parallel to the bedding trace and divided into a multiple set of lamellar and fibrous structures with a length up to a few hundred µm. It does not contain macropores. Pyrite is commonly present inside and on the boundaries of Om2 layers. Om2 is sometimes combined with Om1-a.

Om3: submicron particles between quartz and clays (Fig. 7 d). Om3 is composed of very small and elongate organic matter particles lying parallel to the bedding trace, in the quartz cement or in the clay matrix. Their orientation and shape suggest that they come from the same primary deposit as Om2.

Om4: organic matter in oversize (larger than average) pores (Fig. 7e). Om4 is present in abnormal and very irregular macropores larger than 10 µm. In samples B5 and B11, the shapes of these features could suggest that they result from mineral dissolution during burial, which allows them to behave as preferential pathways for organic matter during maturation. However, no gradual concentration of particular element deposits were found around these oversize pores to confirm this hypothesis.

4.4. Diagenetic precipitation of carbonate veins

Mineral vein features

Carbonate (calcite and ankerite) veins are present in samples B2, B4, B6 and B8. Most veins lie either perpendicular (B4, B6, B8) or parallel to bedding (B2, B8) (Fig. 8).

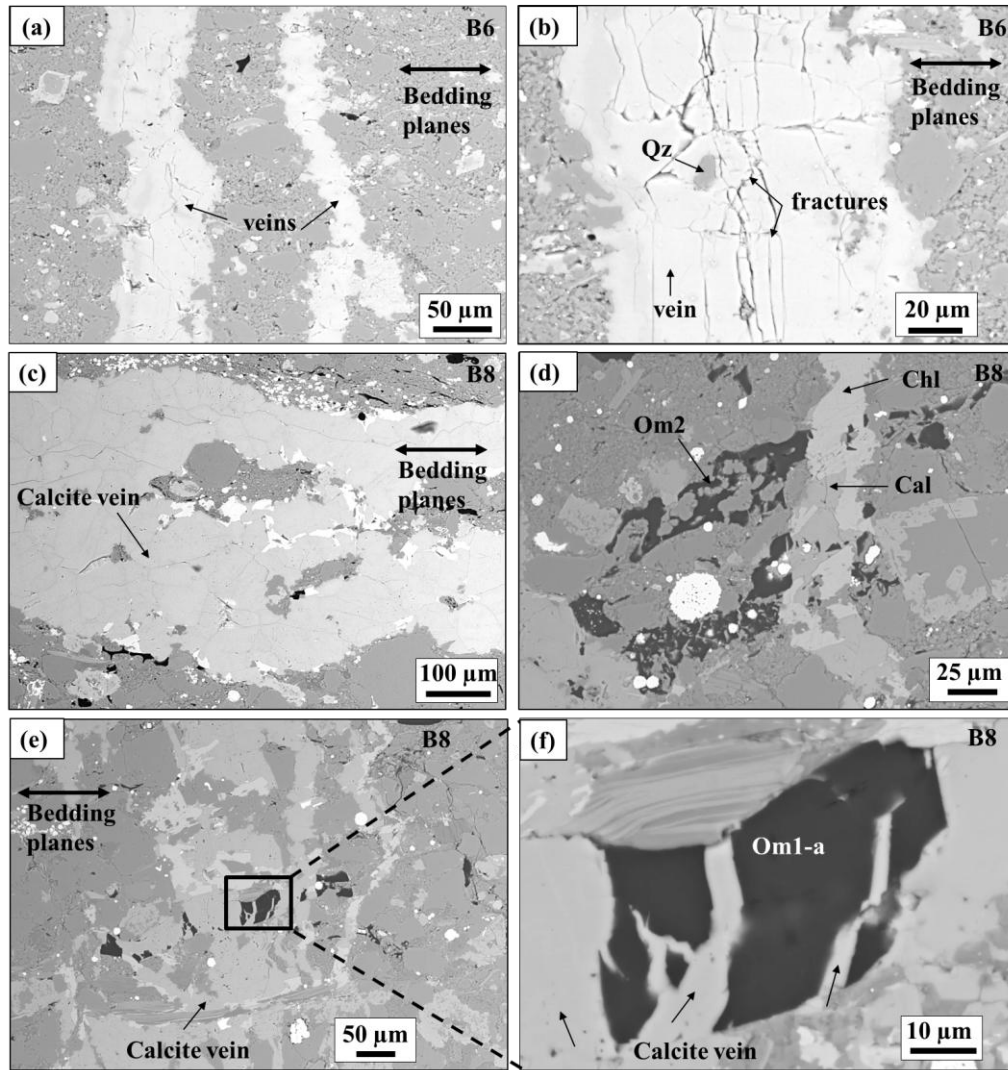


Fig. 8. SEM-BSE images of features attributable to fluid circulation in Bowland shale (examples from samples B6 and B8): (a) two veins of calcite perpendicular to bedding planes in sample B6; (b) fractures in vertical calcite vein in sample B6; (c) horizontal calcite vein in sample B8; (d) and (e) vertical veins of calcite which cross organic Om1-a and Om2 in sample B8; (f) close-up of the organic matter in (e). [Cal: calcite, Qz: quartz].

A few inclined veins are also found in sample B6 (Fig. 5j). These veins are 50 to 300 μm thick and a few centimetres long. Veins occur in a small number of thick fractures in B6 and B2 and in a set of abundant and narrow fractures in sample B8, separated by a few ten μm . The veins contain micrometre vertical and horizontal fractures in sample B6 (Fig. 8b). Figure 8 c-e shows that the calcite veins cross micrometric organic matter particles (Om1).

Ankerite and chlorite have partially replaced calcite in the veins of B8 and B6. Moreover, quartz cement is seen to have filled voids in calcite veins (Fig. 8b), demonstrating that quartz cementation has occurred after veining or that quartz co-precipitated with calcite (Fisher and Byrne, 1987; Fischer et al., 2009). Vein boundaries are sometimes associated with chlorite minerals in the laminated facies (B8) (Fig. 9 a, b).

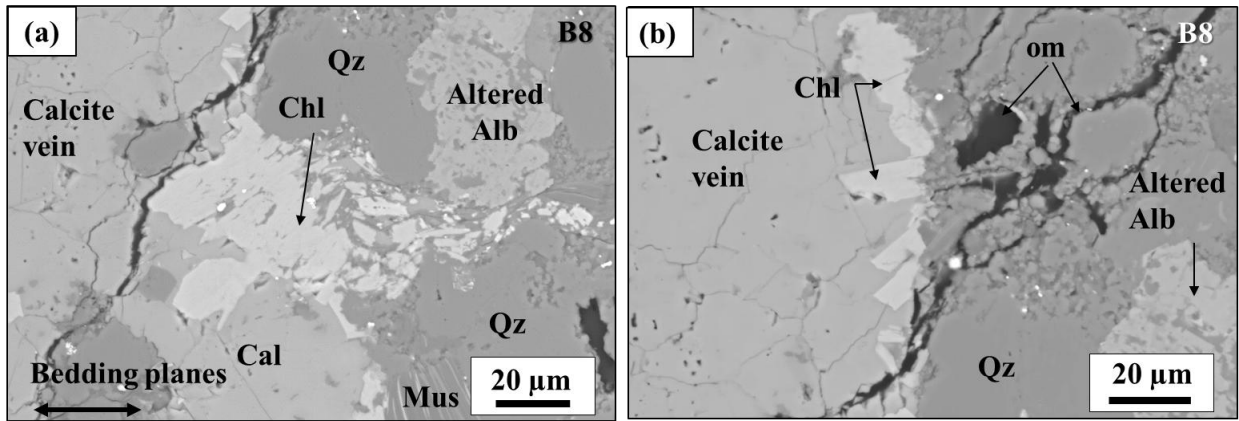


Fig. 9. SEM BSE images of (a) micrometric chlorite and altered albite on the boundaries of a calcite vein ; (b) well-shaped micrometric chlorite on the boundary of a calcite vein. [Chl: chlorite, Alb: albite, Qz: quartz, om :organic matter].

Where present, chlorite occurs as micrometric crystals around the margins of the calcite veins and within the quartz cement between feldspars and kaolinite (Fig. 9 a, b). The crystals are most commonly oriented parallel to the bedding planes. Their location around the veins suggests a formation subsequent to or contemporary with veining.

The calcite veins are partially filled by metal oxide deposits such as rutile, especially in sample B8 where the frequency of calcite veins is highest (Fig. 10 a, b).

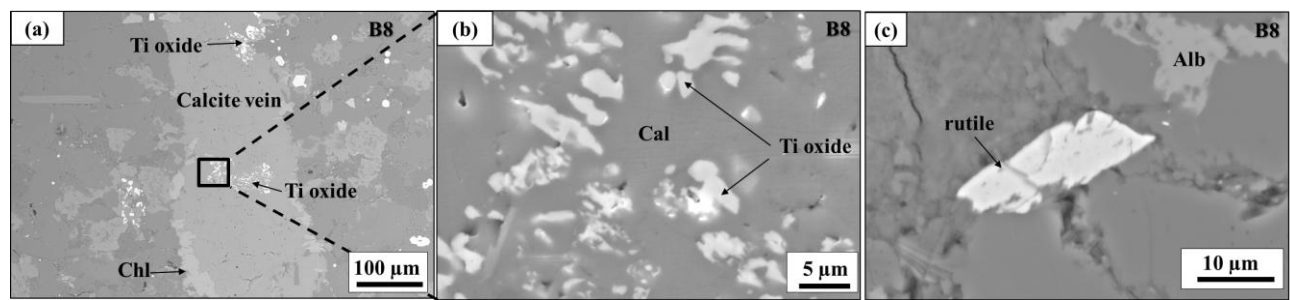


Fig. 10. SEM BSE images of (a) rutile inclusions in a calcite vein perpendicular to bedding planes in B8 at low magnification; (b) enlarged area of a) at high magnification ; (c) detrital rutile grain [Chl: chlorite, Alb: albite, Qz: quartz].

The rutile inclusions have irregular and smooth shapes with diameters varying between 2 and 10 μm (Fig. 10b). These inclusions are also present on the boundaries of veins, in the quartz cement around the veins and as trace minerals within aluminosilicates, especially in kaolinite. Titanium is also present as detrital rutile minerals in the cement (Fig. 10c). The presence of such titanium inclusions in calcite veins proves an authigenic formation by precipitation after veining. These vein inclusions also suggest that Ti-bearing fluid transport event occurred.

4.5. Mineral alteration and neoformation

Association of crystalline kaolinite and altered albite

Primary deposits of clays in shale are usually oriented with basal planes sub-parallel to the trace of bedding planes due to sedimentation and compaction. However, the kaolinite in sample B8 has no preferred orientation and displays large crystalline assemblages (greater than 10 μm) that are often associated with feldspars and quartz cement in quartz-rich laminae (Fig. 11 a, b).

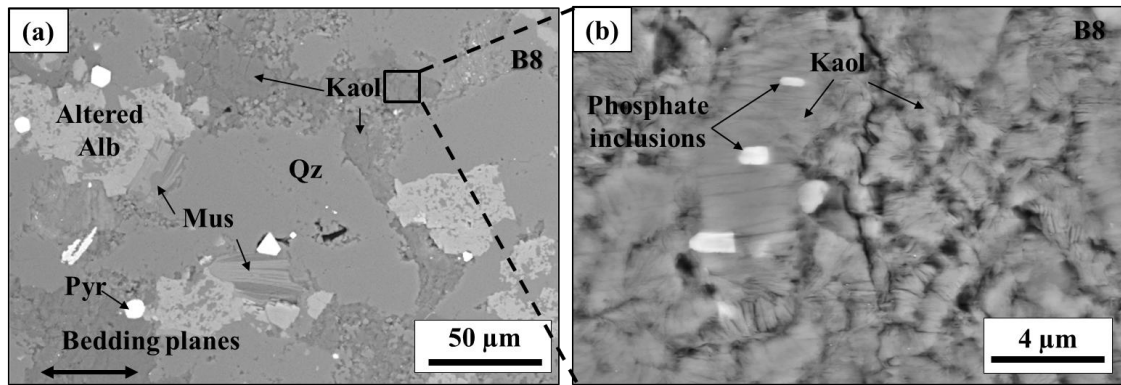


Fig. 11. (a) Randomly orientated kaolinite and muscovite mixed with albite and quartz; (d) large crystalline assemblage of kaolinite with phosphate inclusions in the quartz-rich laminae of B8. [Kaol: kaolinite, Alb: albite, Mus: muscovite, Cal: calcite, Qz: quartz, om: organic matter].

Albites are typically heavily altered, contain many holes partially filled by authigenic quartz, and are bordered by multi-micrometre “booklets” of kaolinite and muscovite. The frequent association of altered albite with authigenic kaolinite and quartz suggests the neoformation of kaolinite from the alteration of albite during burial (Oberlin and Couty, 1970; Boles and Franks 1979).

Idiomorphic ankerite

All shale samples except B2 contain, in various proportions and sizes, very well-formed crystallites of ankerite within the quartz cement, and mixed with calcite in veins. An example from sample B1 is shown in Figure 12a. The size of the ankerite crystals qualitatively varies from a few µm (B7, B8) to 20 µm (B1, B6, B5, B9, B10). The strongly idiomorphic shapes of ankerite and their random orientations suggest that they developed authigenically. Moreover, they crosscut the calcite veins, demonstrating that the ankerite crystals were formed subsequent to veining (Fig. 12 b, c). Quartz cement composed of multi-micrometric grains of quartz partially fills the calcite veins, and crosscuts or surrounds ankerite (Fig. 12 a, d), suggesting that ankerite formation was probably followed by a period of quartz cementation.

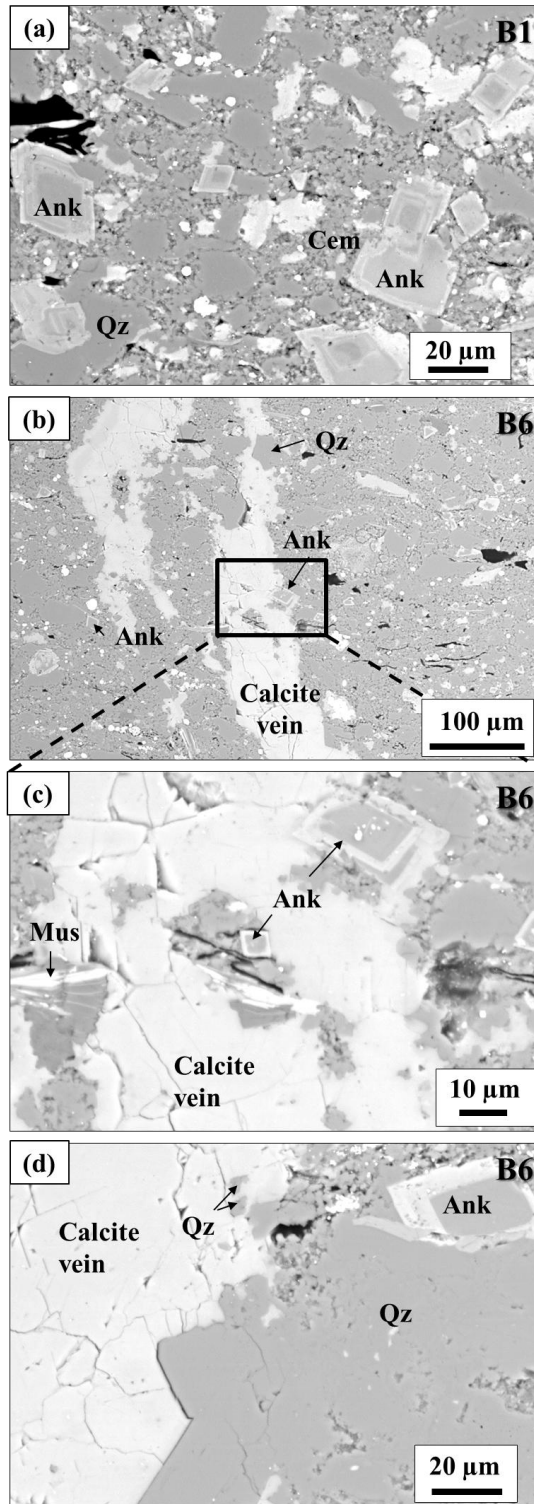


Fig. 12. SEM BSE images of: (a) well-formed ankerite crystallites in the quartz cement of B1; (b) ankerite crossing calcite vein in B6 sample ; (c) magnified view of of b) ; (d) quartz cement crossing well-formed ankerite crystallites and a calcite vein in B6 . [Kaol: kaolinite, Ank: ankerite, Mus: muscovite, Cal: calcite, Qz: quartz, Cem: cement].

319 **4.6. Variability of fractures**

1
2320 Knowledge of the fracture network is important for effective hydraulic treatment design (Gale and
3
4
5321 Holder, 2010). Natural fractures and mechanical discontinuities in general can affect the
6
7322 propagation of hydraulic fractures through delamination for example, which eventually causes
8
9
10323 opening of pathways under high pressure (Warpinski and Teufel 1987; Zhang et al. 2007; Gale et
11
12324 al. 2007; Gale and Holder, 2010).

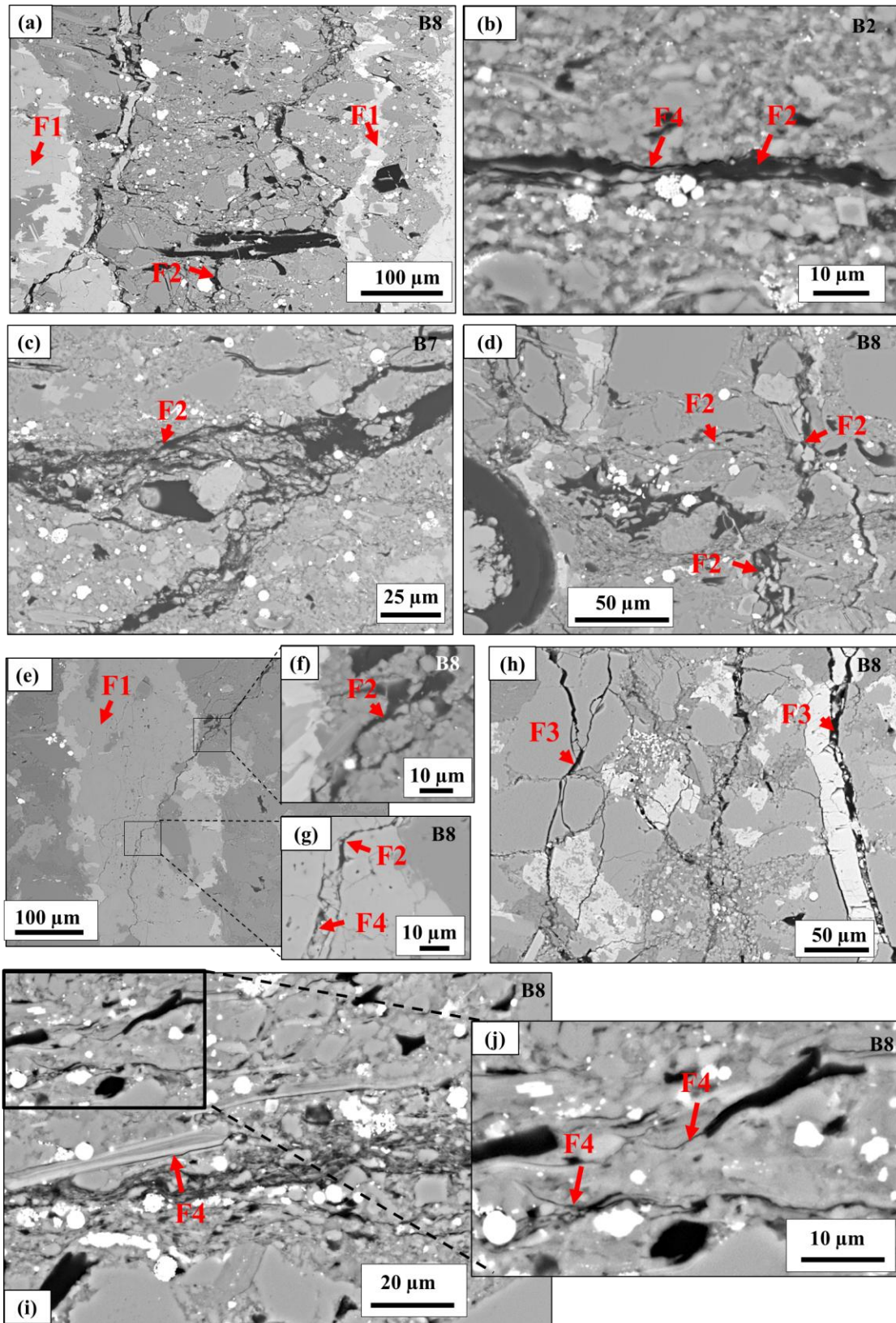


Fig. 13. Fractures (arrows) in Bowland shale. BSE images of : (a) calcite-sealed fracture F1; (b) horizontal bitumen-filled fracture (F2) and empty fracture (F4) along F2; (c) assemblage of thin F2; (d) horizontal and vertical F2; (e) F1 crossed by a bitumen-filled and empty fractures ; (f) inclined

F2 crossing F1 corresponding to the magnified view of (e); (g) vertical empty fracture in F1 in the continuity of F2; (h) resin-filled fractures (F3); (i) empty fractures along organic matter and micas; (j) empty fractures at the extremities of organic matter particles (Om3) in quartz cement.

In this study, four types of fractures were found in Bowland shale:

F1: Mineral-sealed fractures (Figs 8 and 13a). During post-compaction diagenesis, veins were formed as fractures filled with precipitated solids. In this case, the vein-filling phase is mainly calcite and ankerite, and can be termed calcite-sealed fractures. Note that the calcite veins previously described and the calcite-sealed fractures correspond to the same features. The majority of these sealed fractures lie perpendicular to bedding planes but inclined and horizontal fractures are also present. Gale and Holder (2010) showed that Barnett and New Albany shale (USA) samples with natural calcite-sealed fractures display tensile strengths less than 50% of that measured in samples without veins, and will always tend to fail along available fracture planes. Lee et al. (2015) also demonstrated that fractures preferentially refract in the middle of calcite veins during semicircular bending tests on Marcellus Shale. Calcite-sealed fractures are considered to be weak joints because calcite grows between non-carbonate grains without any cement with the border grains (Gale and Holder, 2010; Lee et al. 2015). Despite this tendency, Montgomery et al. (2005) considered that natural calcite-sealed fractures are insignificant for production in the Barnett shale (USA). Shales have usually undergone large amounts of compaction and porosity loss during progressive burial. Thus when vertical planar veins crosscut bedding their formation must have occurred post-compaction strain, when the rock became sufficiently brittle to host fractures.

F2: Natural fractures partially filled by organic matter (Fig. 13 a, b, c, d). The majority of these fractures lie parallel to bedding planes (Fig. 13 b, c), although a significant proportion is inclined or vertical (Fig. 13 a, d, e, f). The horizontal fractures are present in the cement along the boundaries of quartz, calcite, feldspar and mica grains, sometimes crosscutting calcite grains and detrital muscovite. They occur either as discontinuous thin, individual fractures from 1-2 μ m aperture,

continuous and individual fractures of 5-6 μm aperture (Fig. 13 b), or as a set of thin fractures forming a multi-micrometre fracture assemblage (Fig. 13 c) in the prepared samples. Sample B8 contains the greatest number of calcite veins examined, and a significant number of vertical fractures partially filled by bitumen and impregnation resin (Fig. 13 e-g). The bitumen-bearing fractures mostly lie within the organic-rich laminae, but some are also located along and inside calcite veins in the quartz-rich laminae (Fig. 13 e-g). Their aperture is very variable, from $<1\mu\text{m}$ to approximately 25 μm at the studied scales. A small number of fractures show brecciated aspects with a locally higher concentration of small grains of quartz and broken grains of micas, ankerite and calcite (Fig. 13 d).

F3: Fractures filled by resin (Fig. 13 h). These fractures are located in and on the boundaries of calcite veins, and in the quartz cement. Some of these fractures cut quartz and feldspars, and show brecciated aspects. These fractures transect calcite veins in sample B2, demonstrating that their formation was subsequent to veining. Because they became filled by resin and the sample was cut after impregnation, they could have been formed whilst the rock at depth. They are also likely to have been formed by release of in-situ stresses during extraction from the borehole. Their apertures are generally larger (several micrometres) and more homogeneous than the bitumen-filled fractures. Many of these fractures are connected (Fig. 13 h).

F4: “Empty” fractures (Fig. 13 b, g, i, j). Many of these fractures are horizontal, but vertical empty fractures are also observed. The horizontal empty fractures are located alongside or at the ends of organic matter particles (Om3) in the cement (Fig. 13 b), and at the boundaries of quartz or micas (Fig. 13 i, j). Their aperture is generally less than 1 μm . Figure 11 j shows a high rate of occurrence of these fractures in the cement of B8, but they appear discontinuous and unconnected in 2D. Empty fractures also occur as a continuation of bitumen-filled fractures (Fig. 13 e, g), following the direction of pre-existing fractures and cleavages in calcite veins. They may have been produced by stress release during sample recovery from depth, or during handling, but were too small to give easy access to the impregnation resin.

5. Interpretation and Discussion

5.1. Variability of microtexture

Implications for anisotropy and mechanical properties

The samples analyzed in this study display heterogeneous microstructures in terms of mineralogy, texture and TOC (Table 1, Figs 3,4). Even though the mean mineral proportions determined by XRD may be similar for all shale samples studied (e.g. all are quartz-rich), they have very variable microstructures owing to the presence of variable developments of periodic laminae from the μm to mm scale, which should be expected to cause strong and variable mechanical anisotropy. The comparison between the XRD, TOC, OM and SEM results thus emphasises the fact that XRD results alone are insufficient to classify the different shale samples. Petrographic observations can sometimes be superior to bulk analyses because the local variability of a range of parameters can be evaluated (Hackley and Cardott 2016). Key properties such as organic content, gas content and strength depend on such local variations of individual sedimentary facies (Cuss et al. 2015).

It is relatively well-known that the mechanical properties (strength, elastic properties, dilatancy, creep...) of shale are dependent on several parameters such as mineralogy, grain shape and orientation, or porosity related to the orientation of bedding (Bjørlykke and Høeg 1997), and become apparent during unconfined or triaxial compression testing, or during thermal stimulation (Niandou et al. 1989; Ibanez and Kronenberg 1993; Naumann et al. 2007; Gutierrez et al. 2008; Sone and Zoback, 2013; Masri et al. 2014; Cuss et al. 2015; Bonnelye et al. 2016 a,b; Keller et al., 2017). The samples of Lower Bowland shale studied here are very anisotropic with a mineralogic banding plus shape and crystallographic preferred orientation of clays (organic-rich laminae), pyrite and individual organic particles, contrasting with silica-rich laminae. Furthermore, the development of a vertical spatial variability of micro-texture types with variable mineralogy and texture in the sequence of Lower Bowland Shale also induces a coarser vertical degree of development of anisotropy. The laminae have different thickness, from the μm to mm, and may be continuous or

discontinuous, which can lead to local variations of mechanical behavior. Laminae and micro-texture changes induce discontinuities and weak regions that can focus stress concentrations according to corresponding variations in elastic moduli (Lan et al. 2010, Amann et al. 2011), and may provide preferential ways for fracture growth. Variable degrees of development of clay mineral preferred orientation were observed, especially in the laminated micro-texture, ranging from kaolinite mineral grains that are randomly and horizontally arranged in quartz-rich and organic-rich laminae of the laminated mudstones, to laminae in which clay crystallites are strongly oriented as a result of mechanical compaction.

The studied Lower Bowland shale samples therefore display very anisotropic microstructures, but the degree of anisotropy varies with the micro-texture, mainly manifested as a variability of clay orientation and the thickness of laminae.

Primary depositional variability

The Lower Bowland shale samples correspond to hybrid shale in which elements of organic-pyrite-rich mudstone, organic sandstone (quartz-rich laminae of B8 for example) and organic siltstone are intimately interlayered. Turbidite facies have also been found in samples of Bowland shale retrieved from other boreholes (Waters and Davies 2006; Gross et al. 2015). The description of Lower Bowland microfacies herein has shown a wide variation of clastic and carbonate particle sizes and modal proportions, and also of TOC values. These observations reflect a primary variability of depositional controls within the basin, arising from glacio-eustatic fluctuations and tectonic events (Gross et al. 2015; Gawthorpe 1987; Holdsworth and Collinson 1988; Fraser and Gawthorpe 2003; Waters and Condon 2012; Gross et al. 2015).

5.2. High TOC and TOC variability in Lower Bowland shale

The majority of the studied shale samples have TOC higher than 2 wt%, between 1.1 and 6.1 wt% and with an average of 2.88 wt%. The presence of organic matter-rich samples confirms analyses reported in other recent studies (DECC 2010a; Charpentier and Cook 2011; iGas 2012; Andrews

2013). However, the alternation between organic matter-rich and -poor laminae probably acts to decrease the mean value of TOC and clay content at the cm and larger scales. As a consequence, the laminated samples (B7, B8) are classified as low TOC (<2 wt%) shales despite the presence of organic matter-rich laminae. In the same way, the local TOC values at the mm scale could be much higher than the results obtained by bulk TOC measurements at the cm scale for the samples displaying interlaminated facies (B5). SEM observations highlight the fact that the Bowland shale samples in this study contain narrow units (<1 mm) of higher-than-background TOC (but not quantified in this paper) from the μm to the mm scale, and qualitatively confirms the conclusions of Andrews (2013). Similarly, Maynard et al. (1991) measured TOC of two thin Namurian shales from the Upper Carboniferous basin of Northern England with local TOC up to 10 to 13 wt%, but these bands were interbedded within strata of 2 to 3 wt% TOC, which leads to a lower mean TOC.

5.3. *Quartz-rich and clay-poor Lower Bowland shale*

In this study, all shale samples examined are quartz-rich and clay-poor in comparison with some other samples of Bowland shales (ARI 2013; Andrews 2013; EIA 2015; Gross et al. 2015; Ma et al. 2016). Moreover, the clay minerals detected here are mainly kaolinite, whereas other Bowland shale samples may also contain a significant quantity of illite (Gross et al. 2015; Ma et al. 2016) and mixed layer minerals (Gross et al. 2015). In general, shale is predominantly composed of very fine grained particles within an indurated matrix, with or without laminations (Spears 1980; Bates and Jackson 1984; Jackson et al. 2007; Passey et al. 2010; Sondergeld et al. 2010a). Shale is formed by the compaction of clay minerals together with mud or silt-sized framework minerals (Bates and Jackson 1984), and associated with a substantial loss of porosity and development of fissility. A simple definition of shale for gas plays refers to a productive fissile rock containing a significant amount of organic matter from fine-grained rocks which can be carbonate, silica or clay-rich rocks such as the Haynesville, Barnett, Woodford, and Marcellus shales (USA) (Milner et al., 2010; Hammes et al., 2011; Chalmers et al., 2012). Loucks and Ruppel (2007) described shales

containing less than one-third clay minerals as siliceous mudrocks. Various definitions are found in the literature (e.g. Ougier-Simonin and Renard 2016) and the finest grains do not necessarily correspond solely to clay minerals. In the present study, the fine and detrital microstructure of all samples also includes various types of organic matter particles, giving mean whole-rock TOC higher than 2 wt%. Our samples were thus considered as shales even if their clay contents were to be less than 20 wt%. In these rocks, the detrital grains are mixed in a quartz cement rather than a clay matrix, although lenses of clays were also identified in some samples (B5, B8). A low proportion of clay minerals (<35%) is considered to be an advantage to facilitate hydraulic fracturing and gas extraction, because high proportions of tectosilicates (quartz), carbonates and other non-swelling minerals act to limit the rock ductility and to enhance brittleness (Jarvie 2014; Raji et al. 2015). However, Montgomery et al. (2005) and Ross and Bustin (2008) find an inverse relation between silica content and porosity in some areas of Muskwa and Besa River shales, demonstrating that silica content and ability to fracture should be considered alongside other characteristics while estimating potential resource capacities.

Canadian shale from the Muskwa and the Lower Besa River shales in northern British Columbia display similar bulk mineralogy to the Bowland samples used in this study (Ross and Bustin 2008). They are silica-rich (from 58 to 93 wt%), TOC-rich (up to 5 %), and the lowest quartz contents are associated with carbonates such as dolomite (around 40 wt%). Moreover, clay minerals represent only 1 to 25 wt%. As with Besa River and Muskwa shales, Bowland shale samples are composed substantially of detrital silica, but subsequent cementation and replacement crystallization of quartz can make the identification of primary silica grains difficult. Consequently, the origin of some of the silica (quartz) is difficult to explain for the Bowland shale samples presented here. The presence of organic matter derived from algal cysts demonstrates a marine depositional environment, but the absence of siliceous fossils such as radiolaria and other microfossils suggests that the high quartz content is not due to biogenic activity.

5.4. Fluid passage and temperature-driven reactions during burial

Using the cross-cutting principle, different events identified can be qualitatively ordered in time sequence. There are (a) feldspar alteration and neoformation of kaolinite, (b) calcite veining, (c) ankeritization of calcite, (d) quartz cementation and (e) organic matter migration through fractures. These features demonstrate a likely late or post diagenetic circulation within or passage of fluids through these Bowland shale samples, accompanied by veining and mineral alteration at low temperatures. It was followed by a second circulation of hydrocarbon-bearing fluids at higher temperatures. These events were not necessarily followed precisely one by the other, but could be partially concurrent in some cases. The description of these events (below) provides preliminary qualitative data on the burial conditions and maturation of Bowland shale in the Preese-Hall-1 borehole, but these conditions must be further studied on a significant quantity of samples from various locations before being generalized for the Bowland shale basin.

Veining episode

Calcite-veins (F1) crosscut all types of laminae, indicating a displacement of fluids subsequent to primary sediment deposition and compaction. Silica-bearing fluids are presumably expelled from greater depths in the sediment pile as a result of the final stages of compaction and diagenetic reactions. The general planar orientation of veins normal to the compaction fabric demonstrates that the veining occurred in the fully-compacted and indurated host-rock. Experimental observations of mechanical compaction and study of natural shale-bearing basins shows that most compaction is completed by much less than 1 km of burial (Rutter et al. 2017). The orientations observed of the calcite veins suggest a simple, transversely isotropic stress field arising from compaction under the weight of overburden. In the range of samples studied, the majority of veins lie perpendicular to bedding planes, forming a vertical polygonal network (although some horizontal and inclined veins are present), indicating that the maximal principal stress arose from the vertical load. Compaction-induced pore fluid overpressuring occurs when the fluid pressure rises to become very close or equal to the least principal stress during burial. In transversely isotropic loading there is little

difference between the least and the intermediate principal stresses in the horizontal plane. In low permeability rock such as shale, fluid cannot be rapidly expelled from the pores, therefore pore pressure may rise sufficiently to cause vertical hydrofracture formation, perhaps assisted by horizontal crystallization pressure if minerals grow in the veins from locally supersaturated solutions. The possibility of penecontemporaneous fracture along bedding planes can also arise, allowing the formation of horizontal calcite veins in shale owing to the lower fracture toughness for bedding-parallel fracture. It can result of the bedding anisotropy coupled with a low differential stress as a consequence of creep deformation, also promoted by a high pore fluid pressure (Stoneley 1983). However, the absence of organic matter inside the calcite veins (at the μm scale), and the dominance of vertical veins suggest that a relatively high vertical principal stress suppressed significant formation of bedding-parallel veins. Horizontal calcite veins can also form in rocks via the Poisson ratio effect when differential stresses have been relaxed by creep and there is a degree of vertical depressurization through an erosional episode.

The Visean shales of the Bowland basin were deposited during the syn-rift stage of a Lower Carboniferous back-arc basin, and are restricted to graben and half-graben separated by platforms and tilt-block highs (Leeder 1982, 1988; Warr 2000; Waters and Davies 2006). The Namurian shales were deposited in the subsequent thermal subsidence stage (Leeder 1988; Waters and Davies 2006), which is emphasized at small scales with localized extension and compression episodes in the Pennine Basin in Northern England (Waters et al. 1994). Rocks of the Craven group, which includes Visean and Namurian shales in the Bowland sequence elsewhere in the basin, was subjected to tectonic activity during the late Chadian to early Arundian and from the late Asbian until the early Brigantian stages. Evidence of hydrothermal precipitation is very poorly documented within the scientific literature on the Bowland sequence, and it is difficult to discern how long after deposition the carbonate veining occurred. Isotopic and dating measurements of calcite minerals would be required to resolve this question.

In shales, the formation of calcite veins usually occurs at temperatures between 20 and 60°C at shallow to intermediate burial depths (up to hundreds of meters deep) (Al-Aasm et al. 1992), but formation of calcareous mineralization at up to 2.3 km depth has been inferred for some shale formations, such as the middle Devonian shale from the Appalachian plateau (USA) (Evans 1995).

Clay minerals

Quartz-rich laminae within laminated facies contain significant quantities of altered albite, together with micrometric kaolinite with “booklet” shapes. Alteration of detrital albite to authigenic kaolinite in shale is commonly due to a temperature-dependent reaction and pore fluid interactions during burial (Boles and Franks, 1979; Tieh et al., 1986). This reaction occurred in Wilcox shale at temperatures between 100 to 120 °C (Boles and Franks 1979). In the present study, the samples show that a first type of kaolinite resulted from primary deposition (oriented crystals in organic-rich laminae) and a second type (randomly oriented authigenic kaolinite in quartz-rich laminae) that corresponds to the alteration of feldspars (albite).

Ankerite neoformation and quartz cementation

At temperatures higher than 100 °C, iron and magnesium in solution may react with kaolinite to produce chlorite, and/or with calcite to produce ankerite (Boles and Franks 1979). Iron and magnesium generally originate from illitization. Ma et al. (2016) found 23 wt% of illite and 2 wt% of kaolinite in Bowland shale sourced from the Swinden borehole in the west of the Bowland basin. Illite is not present in the XRD analyses of the samples studied here, whereas a few illite grains are seen in a small number of SEM images (in B5 for example). As a result, the sources of iron and magnesium are not yet understood. In general, ankerite is more abundant in sequences of thin sandstones associated with thick shale layers, than it is in thick sandstone layers (Boles and Franks 1979). This generalization was confirmed to be the case for the Bowland shale in Preese Hall-1 by the laminated and interlaminated micro-texture types, and agrees with the observations and inferences of Waters and Davis (2006) and Andrews (2013). Their strong crystallographic forms

and their location in veins as a calcite substitute suggest an authigenic origin and formation subsequent to veining.

Quartz cement partially infills calcite veins and crosscuts authigenic ankerite minerals, revealing that quartz cementation was a late event, occurring after veining and ankerite formation. The presence of veins, crystalline quartz cement and crystalline kaolinite, plus Ti and Fe oxides inside veins, may also imply a passage or circulation of fluids through these laminae, and may partially explain the feldspar alteration to kaolinite.

The quartz cementation is particularly present in quartz-rich laminae of the laminated mudstones which are siltstone to sandstone according to their grain size, and in the unlaminated mudstone samples. In relatively porous, quartz-rich sandstones, large volumes of water can pass through the pore system, permitting cementation in areas where pressure solution is absent (Boles and Franks 1979). Siltstone, sandstone and mudstone are usually studied independently but in our case, they are dispersed periodically and vertically throughout the sample set. In the Wilcox sequence in Texas (USA), the majority of pore waters derived from the original compaction of shale moved through the (more permeable) interbedded sandstones, despite shales representing the majority of the stratigraphic section (Burst 1969). Waters passing from shales to siltstone and sandstones during diagenesis should facilitate chemical component transfers, which may enable the formation of sandstone cement (Curtis 1978; Boles and Franks 1979). The laminated mudstone microtextures of the Bowland shale samples presented here are composed of organic-rich laminae, wherein detrital grains are mixed in a fine cement of quartz and clay lenses, interbedded with quartz-rich laminae, which appear similar to quartz-cemented siltstone and sandstones. These quartz-rich laminae are composed of large grains of quartz cemented by fine-grained quartz grains. Following a hypothesis of Curtis (1978), water could pass from the organic-rich to quartz-rich laminae and its transfer could facilitate the quartz cementation. The very low clay content in Bowland shale samples allows us to admit this hypothesis as possible. However, a low content of primary clay minerals does not necessarily mean that porosity and permeability are high enough to permit this

process. Porosity and permeability data are few for Bowland shale (Andrews 2013), but are commonly very low in shale formations (e.g. Rutter and Mecklenburgh 2017), hence the latter hypothesis could also explain the quartz cementation. The SEM observations suggest that the quartz cementation occurs late, after the veining and ankerite formation (if there is only one period of cementation).

5.5. Organic matter migration during thermal maturation

Migration through fractures

The samples studied here show a high variability of fracture types, in terms of their content (carbonate, bitumen, resin, empty), orientation and size. The opening of fractures generated by the expansion of organic matter is traditionally thought to be caused by pore fluid overpressuring through organic decomposition and petroleum generation, which happens in the 80-150 °C temperature range (Bjørlykke 2010; Kobchenko et al., 2011; Goultly et al., 2012). Very low heating rates between 1-2 °C/Ma have been inferred, but sometimes reaching as high as 10 °C/Ma (Bjørlykke 2010). The late bitumen-filled fractures F2 crosscut the shale microfabric, ankerite grains, quartz cement and carbonate veins, showing the migration of organic-matter occurred subsequently to the formation of all these features.

Fracture orientation

In shales in general, bitumen-bearing horizontal fractures are significantly more common than vertical fractures. For example, horizontal bitumen-filled fractures are found in the clay matrix of organic-rich laminae in the lower half of the Upper Devonian Dunkirk Shale alongside a smaller population of vertical bitumen-filled fractures (Lash and Engelder 2005). These fracture populations also typify the Oligocene Frio shale (Capuano 1993) and Upper Devonian Strachan shale in the Alberta basin (Marquez and Mountjoy 1996) in the USA. The majority of their bitumen-filled fractures are oriented parallel to the bedding planes. This is an important initial

anisotropy caused by the horizontal laminae and clay grain fabric and by many kerogen grains lying flattened parallel to bedding, which can correspond to Om2 and Om3 in our case. When interconnected, these horizontal fractures may aid the migration of hydrocarbons into reservoir rocks (Momper 1978; du Rouchet 1981; Talukdar et al. 1987; Ozkaya 1988; Capuano 1993; Marquez and Mountjoy 1996; Lash and Engelder 2005).

The Upper Devonian Strachan shale in the Alberta basin (USA) and the black shale of the Bluefish basin (Canada) also feature many horizontal fractures (Al-Aasm et al. 1992; Marquez and Mountjoy 1996). Diagenesis generates vertical compaction and smaller induced horizontal stresses during burial, but the horizontal stresses may become larger than the vertical stress as a result of differential stress relaxation during creep, coupled with removal of overburden through erosion, which will facilitate the formation of late horizontal fractures along bedding planes (Turcotte and Schubert 2002; du Rouchet 1981; Spencer 1987).

The Bowland shale samples contain horizontal bitumen-filled (F2) and empty fractures (F4) which are very similar to those observed by Lash and Engelder (2005). However, the samples also contain a significant number of vertical bitumen-filled fractures, especially in dense calcitic-vein areas as in sample B8, and unlike the North American shales described above. Moreover, the vertical bitumen-bearing fractures (F2) systematically crosscut calcite veins and isolated calcite grains in the cement. These late, radially distributed, vertical bitumen-bearing fractures were interpreted to have formed from fractures branching from pre-existing calcite veins owing to reduced fracture toughness at their margins.

6. Conclusions

In this study the variability of the microstructure of the Lower Bowland shale was highlighted from the cm to μm scale using the traditional techniques of microscopy combined with XRD and TOC measurements. The samples show a high variability of : (i) micro-texture types (unlaminated, interlaminated and laminated quartz-rich mudstones and weakly interlaminated calcite-rich

mudstone), (ii) mineralogy, (iii) TOC (from 0.5 to 6.1 wt%), (iv) organic-matter particles (micrometric particles with and without macropores, multi-micrometre layers, submicrometre particles in the cement and particles in oversize pores), and (v) fractures which are organized in a complex network (calcite-sealed, bitumen-filled, empty and resin-filled fractures). The planar geometry of the vertical veins means that the rock was compacted and lithified prior to the formation of the carbonate-sealed fractures. The vertical bitumen-bearing fractures were interpreted as being due to the influence of weak joints generated by the previous carbonate veining episode, which increases the brittleness of the shale. Moreover, the microstructural and mineralogical heterogeneities in areas heavily affected by veins may preferentially facilitate formation of open fractures (resin-filled and empty) during specimen recovery and handling.

The majority of samples are quartz-rich and high TOC (>2 wt%). Some samples have low overall TOC but their microstructure shows local cyclicity between organic-rich and organic-poor laminae. This confirms the presence of narrow (<1 mm) and periodic, qualitatively organic-rich deposits in Bowland shale as has been previously suggested in the literature. The low clay content (<20wt%), the high detrital and cemented quartz content (>50wt%), and the presence of a complex and multi-scale fracture network support the developing interest in the Lower Bowland shale as a potential hydrocarbon resource.

The planar geometry of the vertical calcite veins means that the rock was already compacted and lithified before the carbonate-sealed fractures could form. Subsequently, mineral replacements and authigenic growths of clay minerals and secondary carbonate grains (calcite and ankerite) formed. Later, horizontal bitumen-bearing fractures provided routes for hydrocarbon migration and may have formed as maximum principal stress became horizontal as a result of stress relaxation during creep coupled with erosional offloading. The vertical bitumen-bearing fractures were interpreted as being due to the influence of weak joints generated by the previous carbonate veining episode, which increases the brittleness of the shale. The microstructural and mineralogical heterogeneities

in areas heavily affected by veins may have preferentially facilitated formation of open fractures (resin-filled and empty) during specimen recovery and handling.

The identification of various micro-texture types and their heterogeneities in terms of mineralogy and structure (fractures, laminae) will aid the selection of specific types of samples for 2D and 3D high-resolution imaging in the cement and clay lenses, and for geomechanical characterization. In the same way, the description of the various organic matter particles should guide the selection of key particles for characterization of the pore network within kerogen and bitumen-filled fractures. Evidence of a range of geological episodes such as carbonate-veining, feldspar alteration to kaolinite, ankerite neoformation and bitumen-driven fracturing highlight periods of fluid passage or circulation within the Bowland sequence and temperature-driven reactions occurring during burial, for over the temperature range between approximately 30 and 150 °C. The evidence presented here provides new aspects to aid understanding of the geological history of the Lower Bowland sequence, which should aid in the development of a more generalized understanding of the sequence through future studies across larger sample quantities.

In future studies of Lower Bowland Shale microstructure, a regular separation distance between the samples should be taken and further observations of the cement should be made to evaluate the connectivity of the various fractures, especially the numerous horizontal micrometer-scale empty fractures F4, and to make a better estimation of mineralogy and modal fraction of clays present.

Acknowledgments

The following people contributed to the completion of this paper: Dr Katie Cunnea, Dr Alex C. Leung, Dr Sara Nonni and Mr Paul Waters. We thank the British Geological Survey (Nottingham, UK) for the Bowland Shale samples. This project has received funding from the European Union's Horizon 2020 716 Research and Innovation Programme under the ShaleXenvironment project, (grant no. 640979), with facilities and support also provided by the Research Complex at Harwell,

680 funded in part by NERC (NE/M001458/1) and EPSRC (EP/I02249X/1). Data Statement:
1
2 681 representative research data is presented in the images and graphs in this manuscript.
3
4
5
6
7
8
9
10
11
12
13
14
15
16
17
18
19
20
21
22
23
24
25
26
27
28
29
30
31
32
33
34
35
36
37
38
39
40
41
42
43
44
45
46
47
48
49
50
51
52
53
54
55
56
57
58
59
60
61
62
63
64
65

References

- Abrams, M.A. 2014. Petroleum System Charge Analysis for Liquid-Rich Unconventional Plays. *Unconventional Resources Technology Conference (URTEC)*.
- Al-Aasm, I.S., Muir, I. and Morad, S. 1992. Diagenetic conditions of fibrous calcite vein formation in black shales: petrographic, chemical and isotopic evidence. *Bulletin of Canadian Petroleum Geology*, **41(1)**, 45-56.
- Amann, F., Button, E.A., Evans, K.F., Gischig, V.S. and Blümel, M. 2011. Experimental study of the brittle behavior of clay shale in rapid unconfined compression. *Rock mechanics and rock engineering*, **44(4)**, 415-430.
- Andrews, I. J. 2013. The Carboniferous Bowland Shale gas study: geology and resource estimation. *NERC report*.
- Bates, R. L., and Jackson, J. A. 1984. Dictionary of geological terms. Third Edition. *Anchor Books*, New York.
- Bjørlykke, K. and Høeg, K. 1997. Effects of burial diagenesis on stresses, compaction and fluid flow in sedimentary basins. *Marine and Petroleum Geology*, **14(3)**, 267–276.
- Bjørlykke, K. (2010), *Petroleum Geoscience: From Sedimentary Environments to Rock Physics*, Springer, Berlin, Germany.
- Boles, J.R., and Franks, S.G. 1979. Clay diagenesis in Wilcox sandstones of southwest Texas: implications of smectite diagenesis on sandstone cementation. *Journal of Sedimentary Research*, **49**.
- Bonnelye, A., Schubnel, A., David, C., Henry, P., Guglielmi, Y., Gout, C., Fauchille, A.L. and Dick, P. 2016. Strength anisotropy of shales deformed under uppermost-crustal conditions. *Journal of Geophysical Research* **131**, doi : 10.1002/2016JB013040.

- Bonnelye, A., Schubnel, A., David, C., Henry, P., Guglielmi, Y., Gout, C., Fauchille, A.L. and
 1
 2
 3
 4
 5
 6
 7
 8
 9
 10
 11
 12
 13
 14
 15
 16
 17
 18
 19
 20
 21
 22
 23
 24
 25
 26
 27
 28
 29
 30
 31
 32
 33
 34
 35
 36
 37
 38
 39
 40
 41
 42
 43
 44
 45
 46
 47
 48
 49
 50
 51
 52
 53
 54
 55
 56
 57
 58
 59
 60
 61
 62
 63
 64
 65
- Dick, P., 2016. Elastic wave velocity evolution of shales deformed under uppermost - crustal
 conditions. *Journal of Geophysical Research: Solid Earth* **131**, doi : 10.1002/2016JB013540.
- Borer, J.M. and Harris, P.M. 1991. Lithofacies and cyclicity of the Yates Formation; Permian
 Basin: implications for reservoir heterogeneity. *AAPG Bulletin*, **75(4)**, 726–779.
- Burst, J.F. 1969. Diagenesis of Gulf Coast clayey sediments and its possible relation to petroleum
 migration. *AAPG bulletin*, **53(1)**, 73-93.
- Capuano, R. M. 1993. Evidence of fluid flow in microcracks in geopressed shales. *AAPG
 Bulletin*, **77(8)**, 1303–1314.
- Caracciolo L., Arribas J., Ingersoll R.V. and Critelli S. 2013. The diagenetic destruction of porosity
 in plutoniclastic petrofacies: The Miocene Diligencia and Eocene Maniobra formations,
 Orocopia Mountains, southern California, USA. In: Scott, R. A., Smyth, H. R., Morton, A. C.
 & Richardson, N. (eds) *Sediment Provenance Studies in Hydrocarbon Exploration and
 Production*. Geological Society, London, Special Publications, 386.
- Chalmers, G.R.L. and Bustin, R.M. 2007. The organic matter distribution and methane capacity of
 the Lower Cretaceous strata of northeastern British Columbia, *Int. J. Coal Geol.*, **70(1)**, 223–
 239.
- Chalmers, G.R., Bustin, R.M. and Power, I.M. 2012. Characterization of gas shale pore systems by
 porosimetry, pycnometry, surface area, and field emission scanning electron
 microscopy/transmission electron microscopy image analyses: Examples from the Barnett,
 Woodford, Haynesville, Marcellus, and Doig units. *AAPG bulletin*, **96(6)**, 1099-1119.
- Charpentier, R.R. and Cook, T.A. 2011. USGS Methodology for Assessing Continuous Petroleum
 Resources. *U.S. Geological Survey Open-File Report*.

- Clarke, H., Eisner, L., Styles, P., and Turner, P. 2014. Felt seismicity associated with shale gas hydraulic fracturing: The first documented example in Europe. *Geophysical Research Letters*, **41(23)**, 8308-8314.
- Curtis, C.D. 1978. Possible links between sandstone diagenesis and depth-related geochemical reactions occurring in enclosing mudstones. *Jour. Geol. Soc. London*, **135(1)**, 107-117.
- Curtis, J.B. 2002. Fractured shale-gas systems. *AAPG bulletin*, **86(11)**, 1921-1938.
- Cuss, R.J., Wiseall, A.C., Hennissen, J.A.I., Waters, C.N., Kemp, S.J., Ougier-Simonin, A., Holyoake, S. and Haslam, R.B. 2015. Hydraulic-fracturing: a review of theory and field experience, *European M4ShaleGas Consortium*.
- Davies, J. R., Riley, N. J., and Wilson, D. 1989. The distribution of Chadian and earliest Arundian strata in North Wales: implications for Dinantian (Carboniferous) lithostratigraphy and palaeogeography. *Geological Journal*, **24(1)**, 31-47.
- Davies, S.J. 2008. The record of Carboniferous sea-level change in low-latitude sedimentary successions from Britain and Ireland during the onset of the late Paleozoic ice age. *Geological Society of America Special Papers*, **441**, 187-204.
- DECC, 2010. The unconventional hydrocarbon resources of Britain's onshore basins - shale gas. *DECC Promote website of December 2010*.
- De Pater, C.J. and Baisch, S. 2011. Geomechanical Study of Bowland shale seismicity, *synthesis report 57. Cuadrilla resources*.
- Dewhurst, D.N., Aplin, A.C. and Sarda, J.P. 1999a. Influence of clay fraction on pore-scale properties and hydraulic conductivity of experimentally compacted mudstones, *J. Geophys. Res.*, **104(B12)**, 29261–29274.

- Dewhurst, D.N., Yang, Y. and Aplin, A.C. 1999b. Permeability and fluid flow in natural mudstones, A.C. Aplin, A.J. Fleet, J.H.S. Macquaker (Eds.), *Muds and Mudstones: Physical and Fluid Flow Properties. Geological Society, London, Special Publications*, 125–136.
- EIA, (US) 2013. Technically recoverable shale oil and shale gas resources: an assessment of 137 shale formations in 41 countries outside the United States. *Report June 2013*.
- EIA, (US) 2015a. Technically recoverable shale oil and shale gas resources: United Kingdom. *Report September 2015*.
- EIA, (US) 2015b. *Annual Energy Outlook 2015. Department of Energy*.
- Eisner, L., Janská, E. , Opršal, I. and Matoušek, P. 2011. Seismic analysis of the events in the vicinity of the Preese Hall well, *Report from Seismik to Cuadrilla Resources Ltd*.
- Evans, M.A. 1995. Fluid inclusions in veins from the Middle Devonian shales: A record of deformation1 conditions and fluid evolution in the Appalachian Plateau. *Geological Society of America Bulletin*, **107(3)**, 327-339.
- Evans, D.J., and Kirby, G.A. 1999. The architecture of concealed Dinantian carbonate sequences over the Central Lancashire and Holme highs, northern England. *Proceedings of the Yorkshire Geological Society*, **52(3)**, 297-312.
- Fischer, M.P., Higuera-Díaz, I.C., Evans, M.A., Perry, E.C. and Lefticariu, L. 2009. Fracture-controlled paleohydrology in a map-scale detachment fold: Insights from the analysis of fluid inclusions in calcite and quartz veins. *Journal of Structural Geology*, **31(12)**, 1490-1510.
- Fisher, D. and Byrne, T., 1987. Structural evolution of underthrust sediments, Kodiak Islands, Alaska. *Tectonics*, **6(6)**, 775-793.
- Fraser, A.J., and Gawthorpe, R. L. 2003. An Atlas of Carboniferous basin evolution in northern England. *Geological Society Memoir*, **28**, 79.

- Gale, J.F.W., Reed, R. M. and Holder, J. 2007. Natural fractures in the Barnett Shale and their importance for hydraulic fracture treatments. *American Association of Petroleum Geologists Bulletin*, **91**(4), 603–622.
- Gale, J.F.W. and Holder, J. 2010. Natural fractures in some US shales and their importance for gas production. *Geological Society, London, Petroleum Geology Conference Series*, **7**, 1131-1140.
- Gawthorpe, R.L. 1987. Tectono-sedimentary evolution of the Bowland Basin, northern England, during the Dinantian. *Journal of the Geological Society (London)*, **144**(1), 59-71.
- Charpentier, R.R. and Cook, T.A. 2011. USGS Methodology for Assessing Continuous Petroleum Resources. U.S. *Geological Survey Open-File Report 2011*, 1167.
- Goult, N.R., Ramdhan, A.M. and Jones, S.J. 2012. Chemical compaction of mudrocks in the presence of overpressure. *Petroleum Geoscience*, **18**(4), 471-479.
- Gross, D., Sachsenhofer, R.F., Bechtel, A., Pytlak, L., Rupprecht, B. and Wegerer, E. 2015. Organic geochemistry of Mississippian shales (Bowland Shale Formation) in central Britain: Implications for depositional environment, source rock and gas shale potential, *Marine and Petroleum Geology*, **59**, 1-21.
- Gutierrez, M., Nygård, R., Høeg, K., and Berre, T. 2008. Normalized undrained shear strength of clay shales. *Engineering Geology*, **99**(1), 31-39.
- Hackley, P.C. and Cardott, B.J. 2016. Application of organic petrography in North American shale petroleum systems: a review, *International Journal of Coal Geology*, **163**, 8-51.
- Hammes, U., Hamlin, H.S. and Ewing, T.E., 2011. Geologic analysis of the Upper Jurassic Haynesville Shale in east Texas and west Louisiana. *AAPG bulletin*, **95**(10), 1643-1666.
- Hampson, G.J., Elliott, T., and Davies, S.J. 1997. The application of sequence stratigraphy to Upper Carboniferous fluvio-deltaic strata of the onshore UK and Ireland: implications for the southern North Sea. *Journal of the Geological Society*, **154**(4), 719-733.

- Ibanez, W.D., and Kronenberg, A.K. 1993. Experimental deformation of shale: Mechanical properties and microstructural indicators of mechanisms. *International journal of rock mechanics and mining sciences*, **30(7)**, 723-734.
- IGas, 2012. Results presentation and shale update. *Online presentation*.
www.igasplc.com/uploads/analystpresentationjune2012final.pdf.
- Jackson, J.A., Mehl, J.P., Neuendorf, K.K.E. and American Geological Institute 2007. *Glossary of geology*. In: Springer (ed.). American Geological Institute, Alexandria, Va.
- Jarvie, D.M., Hill, R.J., Ruble, T.E. and Pollastro, R.M. 2007. Unconventional shale gas systems: the Mississippian Barnett Shale of north-central Texas as one model for thermogenic shale gas assessment, *Am. Assoc. Pet. Geol. Bull.*, **91(4)**, 475–499.
- Jarvie, D.M. 2014. Components and processes affecting producibility and commerciality of shale resource systems, *Special Publication Geologica Acta*, **12(4)**, 307–325.
- Keller, L.M., Schwiedrzik, J.J., Gasser, P. and Michler, J. 2017. Understanding Anisotropic Mechanical Properties Of Shales At Different Length Scales: In-Situ Micropillar Compression Combined With Finite Element Calculations. *Journal of Geophysical Research: Solid Earth*.
- Lan, H., Martin, C.D. and Hu, B. 2010. Effect of heterogeneity of brittle rock on micromechanical extensile behavior during compression loading. *Journal of Geophysical Research: Solid Earth*, **115 (B1)**.
- Lash, G.G. and Engelder, T. 2005. An analysis of horizontal microcracking during catagenesis: Example from the Catskill delta complex. *AAPG bulletin*, **89(11)**, 1433-1449.
- Leckie, D.A., Singh, C., Goodarzi, F. and Wall, J.H. 1990. Organic-rich, radioactive marine shale: a case study of a shallow-water condensed section, Cretaceous Shaftesbury Formation, Alberta, Canada. *Journal of Sedimentary Research*, **60(1)**.

- Lee, H.P., Olson, J.E., Holder, J., Gale, J.F., and Myers, R.D. 2015. The interaction of propagating opening mode fractures with preexisting discontinuities in shale. *Journal of Geophysical Research: Solid Earth*, **120**(1), 169-181.
- Leeder, M.R. 1982. Upper Palaeozoic basins of the British Isles—Caledonide inheritance versus Hercynian plate margin processes. *Journal of the Geological Society*, **139**(4), 479-491.
- Leeder, M.R. 1988. Recent developments in Carboniferous geology: a critical review with implications for the British Isles and NW Europe. *Proceedings of the Geologists' Association*, **99**(2), 73-100.
- Loucks, R. G. and Ruppel, S. C. 2007. Depositional setting and lithofacies of the Mississippian Deepwater Barnett Shale in the Forth Worth Basin, Texas. *American Association of Petroleum Geologists Bulletin*, **91**(4), 579– 601.
- Ma, L., Taylor, K.G., Lee, P.D., Dobson, K.J., Dowey, P.J., and Courtois, L. 2016. Novel 3D centimetre-to nano-scale quantification of an organic-rich mudstone: The Carboniferous Bowland Shale, Northern England. *Marine and Petroleum Geology*, **72**, 193-205.
- Marquez, X.M., and Mountjoy, E.W. 1996. Microcracks due to overpressures caused by thermal cracking in well-sealed Upper Devonian reservoirs, deep Alberta basin. *AAPG Bulletin*, **80**(4), 570–588.
- Masri, M., Sibai, M., Shao, J.F. and Mainguy, M., 2014. Experimental investigation of the effect of temperature on the mechanical behaviour of Tournemire shale, *International Journal of Rock Mechanics and Mining Science*, **70**, 185-191.
- Maynard, J.R., Wignall, P.B. and Varker, W.J. 1991. A 'hot' new shale facies from the Upper Carboniferous of Northern England. *Journal of the Geological Society*, **148**(5), 805-808.
- Mckernan R., Mecklenburgh, J., Rutter, E. and Taylor, K.G. 2017. Microstructural controls on the pressure-dependent permeability of Whitby mudstone. In: (E. Rutter, J. Mecklenburgh and K.

- Taylor, eds) Geomechanical and Petrophysical Properties of Mudrocks, *Geological Society of London Special Publication*, **454**, doi:.org/10.1144/SP454 (in press).
- Milner, M., McLin, R. and Petriello, J. 2010. Imaging texture and porosity in mudstones and shales: Comparison of secondary and ion-milled backscatter SEM methods. In *Canadian Unconventional Resources and International Petroleum Conference*. Society of Petroleum Engineers.
- Montgomery, S.L., Jarvie, D.M., Bowker, K.A., and Pollastro, R.M. 2005. Mississippian Barnett Shale, Fort Worth basin, north-central Texas: Gas-shale play with multi-trillion cubic foot potential. *AAPG bulletin*, **89(2)**, 155-175.
- Naumann, M., Hunsche, U. and Schulze, O. 2007. Experimental investigations on anisotropy in dilatancy, failure and creep of Opalinus Clay. *Physics and Chemistry of the Earth, Parts A/B/C*, **32(8)**, 889-895.
- Niandou, H., Shao, J.F., Henry, J.P. and Fourmaintraux, D. 1989. Laboratory Investigation of the mechanical behaviour of Tournemire shale, *International Journal of Rock Mechanics and Mining Science*, **34(1)**, 3-16.
- Oberlin, A. and Couty, R. 1970. Conditions of kaolinite formation during alteration of some silicates by water at 200 C. *Clays and Clay minerals*, **18**, 347-356.
- Ougier-Simonin, A., and Renard, F. 2016. Microfracturing and microporosity in shales, *Earth Science Reviews*, **162**, 198-226.
- Ozkaya, I. 1988. A simple analysis of oil-induced fracturing in sedimentary rocks. *Marine and Petroleum Geology*, **5(3)**, 293-297.
- Passey, Q.R., Bohacs, K.M., Esch, W.L., Klimentidis, R. and Sinha, S. 2010. From Oil-Prone Source Rock to Gas-Producing Shale Reservoir - Geologic and Petrophysical. Characterization

- of Unconventional Shale Gas Reservoirs. *Petroleum Engineers Unconventional Gas Conference*, Pittsburgh, Pennsylvania.
- Perri, F. 2008. Clay mineral assemblage of the Middle Triassic-Lower Jurassic mudrocks from Western-Central Mediterranean Alpine Chains. *Periodico di Mineralogia*, **77**, 23-40.
- Perri, F., Cirrincione, R., Critelli, S., Mazzoleni, P. and Pappalardo, A. 2008. Clay mineral assemblages and sandstone compositions of the Mesozoic Longobucco Group (north-eastern Calabria): implication for burial history and diagenetic evolution. *International Geology Review*, **50**, 1116-1131.
- Perri F., Caracciolo L., Cavalcante F., Corrado S., Critelli S., Muto F. and Dominici R. 2016. Sedimentary and thermal evolution of the Eocene-Oligocene mudrocks from the southwestern Thrace Basin (NE Greece). *Basin Research*, **28**, 319-339.
- Raji, M., Grocke, D., Greenwell, H.C., Gluyas, J.G. and Cornford, C. 2015. The effect of interbedding on shale reservoir properties. *Marine and Petroleum Geology*, **67**, 154-169.
- Rouchet (du), J. 1981. Stress fields, a key to oil migration, *AAPG Bulletin*, **65**(1), 445–459.
- Ross, D.J.K. and Bustin, R.M. 2007. Shale gas potential of the Lower Jurassic Gordondale Member, northeastern British Columbia, Canada, *Bull. Can. Pet. Geol.*, **55**(1), 51–75.
- Ross, D.J.K. and Bustin, R.M. 2008. Characterizing the shale gas resource potential of Devonian–Mississippian strata in the Western Canada sedimentary basin: Application of an integrated formation evaluation. *AAPG bulletin*, **92**(1), 87-125.
- Rossi, C., Kalin, O., Arribas, J., Tortosa, A. 2002. Diagenesis, provenance and reservoir quality of Triassic Tagi sandstones from Ourhoud Field, Berkine (Ghadames) Basin, Algeria. *Marine and Petroleum Geology*, **19**, 117- 142.
- Rutter, E. H., Mecklenburgh, J. and Taylor, K. G. 2017. Geomechanical and petrophysical properties of mudrocks: introduction In: Rutter, E. H., Mecklenburgh, J. & Taylor, K. G.

- (eds) Geomechanical and Petrophysical Properties of Mudrocks. *Geological Society, London, Special Publications*, **454**.
- Rutter, E.H. and Mecklenburgh, J. 2017. Hydraulic conductivity of bedding-parallel cracks in shale as a function of shear and normal stress. In: Rutter, E.H., Mecklenburgh, J. & Taylor, K.G. (eds) Geomechanical and Petrophysical Properties of Mudrocks. *Geological Society, London, Special Publications*, **454**.
- Schieber, J., 1996. Early diagenetic silica deposition in algal cysts and spores: a source of sand in black shales? *Journal of Sedimentary Research*, **66**(1).
- Schieber, J., Krinsley, D. and Riciputi, L. 2000. Diagenetic origin of quartz silt in mudstones and implications for silica cycling. *Nature*, **406**(6799), 981-985.
- Sone, H. and Zoback, M.D. 2013. Mechanical properties of shale-gas reservoir rocks—Part 1: Static and dynamic elastic properties and anisotropy. *Geophysics*, **78** (5), D381-392.
- Spears, D.A. 1980. Towards a classification of shales. *Journal of the Geological Society*, **137**(2), 125-129.
- Spears, D.A. and Amin, M.A. 1981. Geochemistry and mineralogy of marine and non-marine Namurian black shales from the Tansley borehole. *Sedimentology*, **28**(3), 407-417.
- Spencer, C. W. 1987. Hydrocarbon generation as a mechanism for overpressuring in Rocky Mountain region. *AAPG Bulletin*, **71**(4), 368–388.
- Stoneley, R. 1983. Fibrous calcite veins, overpressures, and primary oil migration. *AAPG Bulletin*, **67**(9), 1427-1428.
- Talukdar, S., Gallango, O., Vallejos, C., and Ruggiero, A. 1987. Observations on the primary migration of oil in the La Luna source rocks of the Maracaibo Basin, Venezuela. *B. Doligez, Eds., Migration of hydrocarbons in sedimentary basins: Paris, Editions Technip*, 59–78.

- Tieh, T.T., Berg, R.R., Popp, R.K., Brasher, J.E. and Pike, J.D. 1986. Deposition and diagenesis of upper Miocene arkoses, Yowlumne and Rio Viejo fields, Kern County, California. *AAPG Bulletin*, **70(8)**, 953-969.
- U.S. Energy Information Administration (USEIA) 2011. World Shale Gas Resources: an initial assessment of 14 regions outside the United States. *Report prepared by Advanced Resources International Inc.* www.eia.gov/analysis/studies/worldshalegas/.
- Warpinski, N.R. and Teufel, L.W. 1987. Influence of geologic discontinuities on hydraulic fracture propagation. *Journal of Petroleum Technology*, **39(02)**, 209–220.
- Warr, L.N. 2000. The Variscan Orogeny: The welding of Pangea, in Woodcock, N. and Strachan, R. eds, *Geological History of Britain and Ireland*: Blackwell, Oxford, 271–391.
- Waters, C.N., Glover, B.W., and Powell, J.H. 1994. Structural synthesis of S Staffordshire, UK: implications for the Variscan evolution of the Pennine Basin. *Journal of the Geological Society*, **151(4)**, 697-713.
- Waters, C.N. and Davies, S.J. 2006. Carboniferous: extensional basins, advancing deltas and coal swamps. *The geology of England and Wales/edited by PJ Brenchley and PF Rawson. London: Geological Society of London 2006*, 173-223.
- Waters, C.N., Waters, R.A., Barclay, W.J. and Davies, J.R. 2009. A lithostratigraphical framework for the Carboniferous successions of southern Great Britain (onshore). *British Geological Survey Research Report RR/09/01*.
- Waters, C.N. and Condon, D.J. 2012. Nature and timing of Late Mississippian to MidPennsylvanian glacio-eustatic sea-level changes of the Pennine Basin, UK. *Journal of Geological Society*, **169(1)**, 37-51.

Figure captions

Fig. 1. Location of the Preese Hall-1 borehole in: (a) the United Kingdom and (b) the Bowland Basin (adapted from Evans & Kirby 1999; mapsofworld 2015).

Fig. 2. Bowland basin stratigraphy in the Preese Hall-1 borehole, showing the stratigraphic locations of the samples studied, which lie within the Bowland-Hodder group.

Fig. 3. XRD patterns corresponding to the samples (a) B8 and (b) B5.

Fig. 4. (a) Variability of mineralogical composition of all samples, and (b) Mineralogy of all samples represented on a ternary diagram plotting proportions of clays, quartz and carbonates.

Fig. 5. Variability of mudstone micro-texture types of Bowland Shale from at the cm and mm scales : macroscopic views (a-f) and optical images (g-l).

Fig. 6. Variability of mudstone micro-texture types of Bowland Shale at the μm scale by back-scattered electron (BSE) images under SEM : (a,b) unlaminated quartz-rich mudstone, (c,d) weakly interlaminated calcite-rich mudstone, (e-i) interlaminated quartz-rich mudstone, (j-o) laminated quartz-rich mudstone. [Cal: calcite, Qz: quartz, Ank: ankerite, Om: organic matter, Qz: quartz, Pyr: pyrite, Cem: cement, Kaol: kaolinite, Alb: albite].

Fig. 7. Various types of organic matter particles in Bowland shale under SEM: (a) micrometric particles of organic matter without macropores (Om1-a); (b) micrometric particles of organic matter with macropores (Om1-b); (c) micrometric layers of organic matter (Om2); (d) Sub-micrometric organic matter particles in cement (Om3); (e) organic matter in oversize pores.

Fig. 8. SEM-BSE images of features attributable to fluid circulation in Bowland shale (examples from samples B6 and B8): (a) two veins of calcite perpendicular to bedding planes in sample B6; (b) fractures in vertical calcite vein in sample B6; (c) horizontal calcite vein in sample B8; (d) and (e) vertical veins of calcite which cross organic Om1-a and Om2 in sample B8; (f) close-up of the organic matter in (e). [Cal: calcite, Qz: quartz].

Fig. 9. SEM BSE images of (a) micrometric chlorite and altered albite on the boundaries of a calcite vein ; (b) well-shaped micrometric chlorite on the boundary of a calcite vein. [Chl: chlorite, Alb: albite, Qz: quartz, om :organic matter].

Fig. 10. SEM BSE images of (a) rutile inclusions in a calcite vein perpendicular to bedding planes in B8 at low magnification; (b) enlarged area of a) at high magnification ; (c) detrital rutile grain [Chl: chlorite, Alb: albite, Qz: quartz].

Fig. 11. (a) Randomly orientated kaolinite and muscovite mixed with albite and quartz; (d) large crystalline assemblage of kaolinite with phosphate inclusions in the quartz-rich laminae of B8. [Kaol: kaolinite, Alb: albite, Mus: muscovite, Cal: calcite, Qz: quartz, om: organic matter].

Fig. 12. SEM BSE images of: (a) well-formed ankerite crystallites in the quartz cement of B1; (b) ankerite crossing calcite vein in B6 sample ; (c) magnified view of of b) ; (d) quartz cement crossing well-formed ankerite crystallites and a calcite vein in B6 . [Kaol: kaolinite, Ank: ankerite, Mus: muscovite, Cal: calcite, Qz: quartz, Cem: cement].

Fig. 13. Fractures (arrows) in Bowland shale. BSE images of : (a) calcite-sealed fracture F1; (b) horizontal bitumen-filled fracture (F2) and empty fracture (F4) along F2; (c) assemblage of thin F2; (d) horizontal and vertical F2; (e) F1 crossed by a bitumen-filled and empty fractures ; (f) inclined F2 crossing F1 corresponding to the magnified view of (e); (g) vertical empty fracture in F1 in the continuity of F2; (h) resin-filled fractures (F3); (i) empty fractures along organic matter and micas; (j) empty fractures at the extremities of organic matter particles (Om3) in quartz cement.

Table 1. Mineral proportion obtained by X-Ray Diffraction and Total Organic Content measurements for all samples (1 : Pendleide limestone, 2 : Worston shale).

**An Enhanced Understanding of the Basinal Bowland Shale in Lancashire (UK),
through Microtextural and Mineralogical Observations**

A. L. Fauchille^{1,2*}, L. Ma¹, E. Rutter³, M. Chandler³, P. D. Lee^{1,2} & K. G. Taylor³

¹Manchester X-Ray Imaging Facility, School of Materials, the University of Manchester, Oxford
Road, Manchester M13 9PL, UK.

²Research Complex at Harwell, Rutherford Appleton Laboratory, Didcot Oxon OX11 0FA, UK.

³School of Earth and Environmental Sciences, The University of Manchester, Oxford Road,
Manchester, M13 9PL, UK.

*Corresponding author : al.fauchille.research@gmail.com

Abbreviated title: Microtextural observations of Bowland Shale

Keywords : Bowland shale, variability, micro-texture, organic matter, fractures, microscopy,
characterization

Submitted to Marine and Petroleum Geology

Re-submission in July, 2017

Abstract

Variability in the Lower Bowland shale microstructure is investigated here, for the first time, from the centimetre to the micrometre scale using optical and scanning electron microscopy (OM, SEM), X-Ray Diffraction (XRD) and Total Organic Carbon content (TOC) measurements. A significant range of micro-textures, organic-matter particles and fracture styles was observed in rocks of the Lower Bowland shale, together with the underlying Pendleside Limestone and Worston Shale formations encountered the Preese Hall-1 Borehole, Lancashire, UK. Four micro-texture types were identified: unlaminated quartz-rich mudstone; interlaminated quartz- and pyrite-rich mudstone; laminated quartz and pyrite-rich mudstone; and weakly-interlaminated calcite-rich mudstone. Organic matter particles are classified into four types depending on their size, shape and location: multi-micrometre particles with and without macropores; micrometre-size particles in cement and between clay minerals; multi-micrometre layers; and organic matter in large pores. Fractures are categorized into carbonate-sealed fractures; bitumen-bearing fractures; resin-filled fractures; and empty fractures. We propose that during thermal maturation, horizontal bitumen-fractures were formed by overpressuring, stress relaxation, compaction and erosional offloading, whereas vertical bitumen-bearing, resin-filled and empty fractures may have been influenced by weak vertical joints generated during the previous period of veining. For the majority of samples, the high TOC (>2 wt%), low clay content (<20wt%), high proportion of quartz (>50wt%) and the presence of a multi-scale fracture network support the increasing interest in the Bowland Shale as a potentially exploitable oil and gas source. The microtextural observations made in this study highlight preliminary evidence of fluid passage or circulation in the Bowland Shale sequence during burial.

1. Introduction

Characterization of the properties of shales is an essential process in the estimation of their gas and oil resource potential. Important shale gas and oil resources are believed to exist in Western Europe (EIA 2013) and in particular in the UK (EIA 2015a). In order to understand and quantify the properties of this potential resource, the geology of the Bowland and Hodder mudstone formations has been investigated throughout the last decades at the basin-scale (Gawthorpe 1987; Davies et al. 1989; Hampson et al. 1997; Fraser & Gawthorpe 2003; Waters & Davies, 2006; Davies et al. 2008; Waters & Condon 2012; Andrews 2013), and more recently at the nanometre scale (Ma et al. 2016). In general, the most commonly investigated properties of shale have been the lithology, sedimentary architecture, total organic matter carbon content (TOC), kerogen type, thermal maturity and oil and gas expulsion potential, the mineralogical composition, diagenetic conditions and the presence of natural fracture networks (Curtis 2002; Rossi et al., 2002; Montgomery et al. 2005; Jarvie et al. 2007; Ross & Bustin 2007, 2008; Perri, 2008; Carraciolo et al., 2013; Jarvie 2014; Abrams et al. 2014; Raji et al. 2015; Perri et al., 2008, 2016). The evaluation of shale resources is complicated because of the heterogeneous nature of the fine-grained strata and their intricate, small-sized pore networks, which are strongly dependent on the above geological factors (Yang & Aplin, 1998; Dewhurst et al. 1999a, b; Ross & Bustin 2007; Chalmers & Bustin 2007; Mckernan et al. 2017). From the millimetre to the nanometre scale, shale gas is stored as free gas in natural fractures, within both intergranular and intra-granular porosity and adsorbed onto kerogen and clay-particle surfaces. It may also be dissolved in kerogen and bitumen (Curtis 2002). The microstructure directly influences the distribution of gas and its transport properties through the porous network. Knowledge of the microstructure of shale is consequently required. However, there is still a very limited understanding of the processes giving rise to pore networks, fractures, and organic and mineral properties in British Shales. In particular, data are sparse for the Bowland and Hodder Shales, despite forming an important potential oil and gas resource. Detailed

petrographic studies of these shales are required to allow a better comparison with other shale formations, especially the relatively well understood shale reservoirs from northern America. The major goal of this study is to present the first multi-scale (centimetre to micrometre) and petrologic characterization of the different microtextures of Bowland shale encountered in the Preese Hall-1 borehole, a significant and recent exploration borehole in Lancashire, NW England, using optical and scanning electron microscopy in combination with XRD and TOC analysis. Due to the coarse resolution of sampling within our study, we recognize that potential stratigraphic variability between samples implies that microtextures other than those identified in our study could potentially be present within the borehole.

2. Geological Settings and Sampling

In this study, eleven centimetric-sized samples of mudstone were collected from the Preese Hall-1 borehole core repository at the British Geological Survey (Nottingham, UK). Preese-Hall-1 is situated in the Carboniferous basin Bowland Shale Formation, which extends across a large part of central Britain (Fig. 1). Drilling of the Preese Hall-1 borehole was initiated in August 2010. It is situated on the Fylde coast of NW Lancashire at 53° 49' 19.006"N; 2° 56' 56.576 W", near to Blackpool, north-west England.

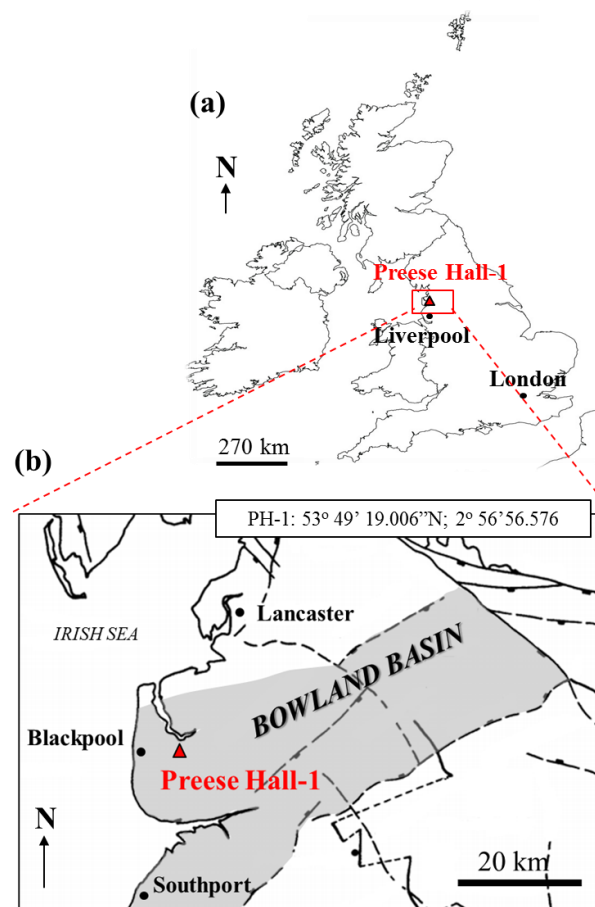


Fig. 1. Location of the Preese Hall-1 borehole in: (a) the United Kingdom and (b) the Bowland Basin (adapted from Evans & Kirby 1999; mapsofworld 2015).

Preese Hall-1 is the first dedicated unconventional shale gas borehole in the UK and Europe (de Pater & Baisch 2011), and was drilled to a depth of 2745 meters. Preliminary hydraulic stimulations of this borehole were performed by Cuadrilla Resources Ltd in 2011 (Eisner et al. 2011; de Pater & Baisch 2011; Clarke et al. 2014).

Within the Bowland basin, the rocks of the Bowland-Hodder group encountered in the Preese Hall-1 borehole are divided into an upper unit characterised by some 150 m of shale (Upper Bowland Shale) and a lower, more variable unit (Lower Bowland Shale) containing almost 500 m of shale interbedded with clastic and carbonate deposits due the influence of glacio-eustatic sea level changes and tectonic events (Gawthorpe 1987; Andrews 2013). The Bowland Shale Formation

(Upper and Lower Bowland shales) corresponds to ages between the end of the Visean (Brigantian) and the beginning of the Namurian (Pendleian) (Waters et al. 2009) (Fig. 2). The Pendleside Limestone Formation lies below the Bowland Shale Formation and marks the bottom of the Bowland Shale sequence (Waters et al. 2009). Beneath, the Worston shale group forms a further 150 m thick unit of shales. The top of the Bowland shale group passes into the Millstone Grit Group (Pendleian). The Bowland shale, Pendleside limestone and Worston shale are all included in the Bowland-Hodder Unit corresponding to the whole Visean period (Andrews, 2013).

The samples used for the present study were taken predominantly (Fig. 2) from the lower Bowland Shale Formation (samples B1 through B10). Sample B11 was taken from the Pendleside limestone Formation and B13 from the lower part of the Worston Shale Formation (there is no B12).

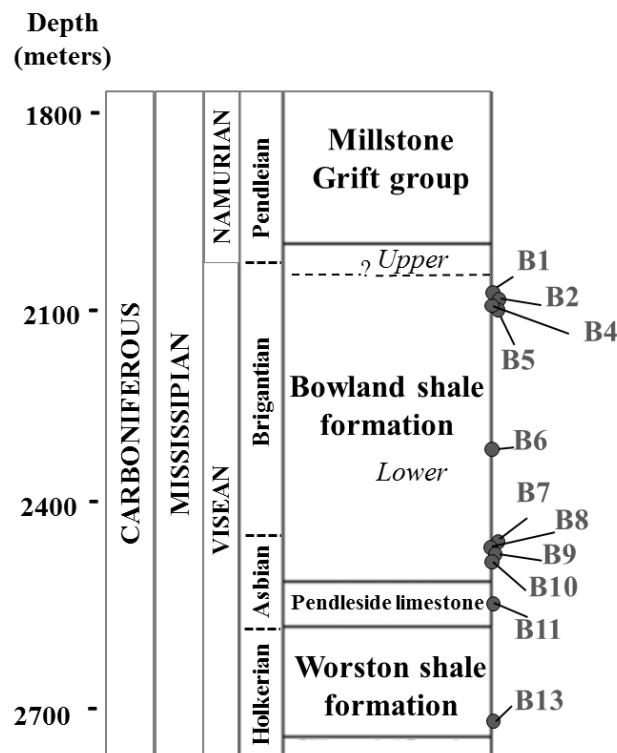


Fig. 2. Bowland basin stratigraphy in the Preese Hall-1 borehole, showing the stratigraphic locations of the samples studied, which lie within the Bowland-Hodder group.

In general, the organic content of the Bowland Shales lies between 1 and 3 wt% (Spears & Amin 1981; USEIA 2011), but can reach 5-8% (iGas 2012; Andrews 2013; EIA 2015).

3. Material Preparation and Methods

The mineralogy of all samples was semi-quantified by X-Ray diffraction (XRD) on a Bruker D8 Advance diffractometer, equipped with a Göbel Mirror and Lynxeye detector. The X-ray tube provided $\text{CuK}_{\alpha 1}$ X-rays with a wavelength of 1.5\AA . Sample preparation involved grinding $\sim 0.1\text{g}$ of sample material mixed with $\sim 1\text{ml}$ of amyl acetate. Samples were scanned between 5 and $70^\circ 2\theta$, with a step size of 0.02° and a count time of 0.2s per step.

Total organic carbon (TOC) was measured with an experimental uncertainty of $\pm 0.02\%$ TOC using 100 mg powder samples in a Leco carbon analyzer (Michigan, United States) at the University of Newcastle (UK), after rock acidification and organic matter combustion.

All samples were vacuum impregnated with epoxy resin and mechanically polished as thin sections for optical and scanning electron microscopy. Optical microscopy was performed using an Olympus SZX16 stereomicroscope to obtain low magnification images of the general textures from cm- to mm-scale . Low magnification observations were also made with a JEOL JSM 6610LV SEM equipped with a back-scattered electron detector and semi-quantitative EDS analyser. The accelerator voltage was 20 kV and the working distance 10mm . To confirm the nature of minerals, EDS point analysis and mapping was used with AZtec© software. High magnification observations were performed with a SEM FEI Quantax FEG 650, with an accelerator voltage of 10 kV . Apart from macropores, pore types are not described here because of the resolution of the study. The differentiation between impregnation resin and organic matter under SEM was achieved using a combination of three criteria:

- (a) the morphology: organics have smooth faces at boundaries, whereas resin has clear boundaries with the material due to its viscosity. The resin contains clear cracks at some places, formed by the local heating by the electron beam at high energy (20 kV).

(b) the peak intensity of carbon in EDS analysis. In our case, the organic matter particles show a peak of carbon for energy much higher than 15 cps.eV^{-1} , in contrast to the resin.

(c) the presence of chloride. Araldite 2020 resin contains a few percent of chloride which is enough to be detected by EDS, in contrast to organic particles.

The small sizes of the samples available for this study precluded the measurement of bulk porosity and permeability.

4. Results

4.1. Bulk composition and TOC

The samples are **mainly** composed of quartz, calcite, ankerite, muscovite, kaolinite, albite and pyrite, based on XRD quantification (Table 1, Fig. 3). Two examples of the XRD patterns are given in Fig. 3. These mineral assemblages determined by XRD were confirmed by SEM observations, especially for clay minerals.

				Proportions (wt%)								
				Kaolinite	Quartz	Calcite	Ankerite	Pyrite	Muscovite	Albite	TOC	
Bowland-Hodder unit	Lower Bowland shale	Samples	Depth (meters)	Facies								
		B1	2073.34	Unlaminated quartz-rich	0	58	15	13	2	9	3	1.4
		B2	2081.27	Transition un- to interlaminated quartz-rich	5	53	17	1	8	11	5	4.1
		B4	2089.83	Unlaminated quartz-rich	5	65	4	5	4	11	6	1.7
		B5	2091.69	Interlaminated quartz-rich	6	56	12	6	6	10	4	3.2
		B6	2344.70	Unlaminated quartz-rich	7	71	6	2	1	10	3	6.1
		B7	2488.84	Interlaminated quartz-rich	3	68	10	3	2	10	4	1.5
		B8	2495.27	Laminated quartz-rich	18	52	3	11	2	5	9	1.1
		B9	2496.92	Unlaminated quartz-rich	6	52	21	3	5	9	4	2.1
	B10	2500.49	Unlaminated quartz-rich	5	56	18	1	5	10	5	2.0	
P.L ¹	B11	2586.29	Unlaminated Calcite-rich	1	23	69	2	1	2	2	0.5	
W.S ²	B13	2710.40	-	5	73	6	0	1	11	4	5.6	

Table 1. Mineral proportion obtained by X-Ray Diffraction and Total Organic Content measurements for all samples (1 : Pendleside limestone, 2 : Worston shale)

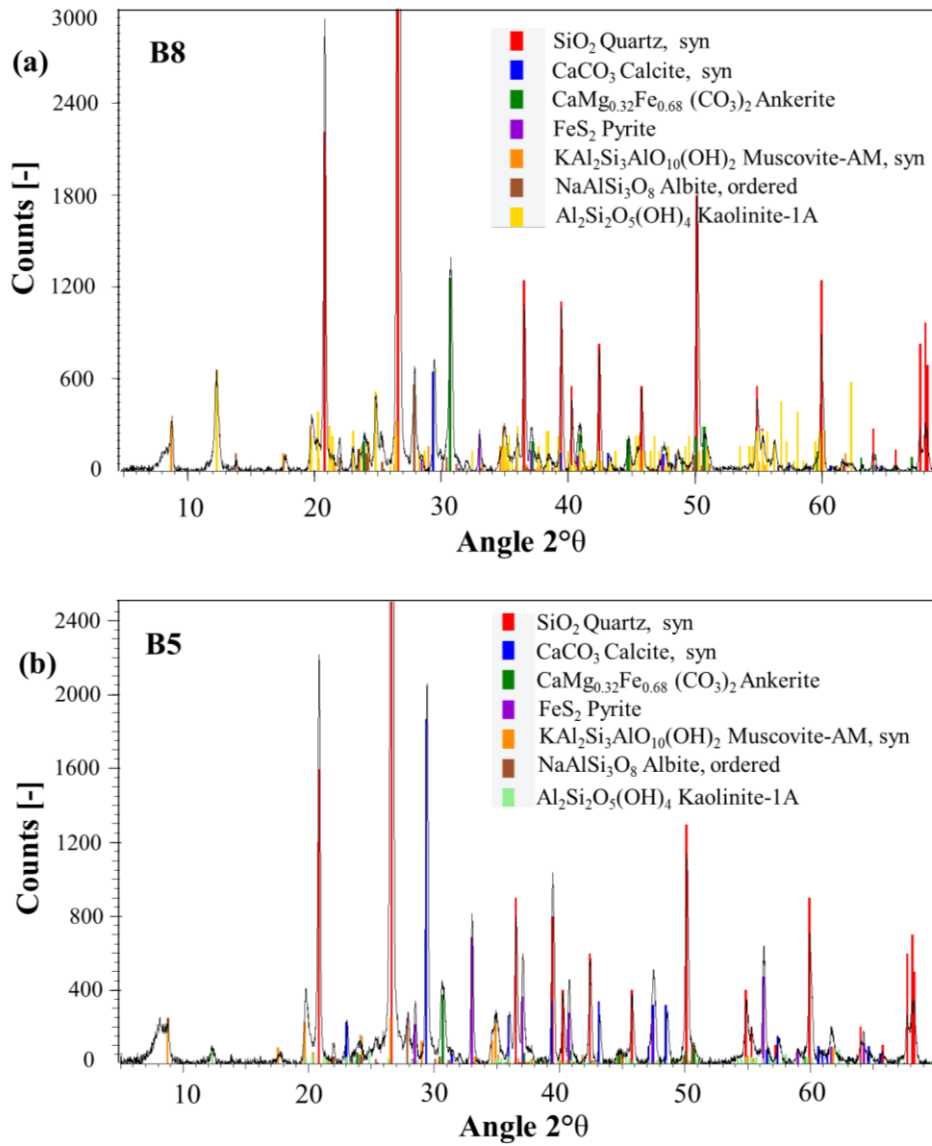


Fig. 3. XRD patterns corresponding to the samples (a) B8 and (b) B5.

All Bowland-Hodder mudstone samples in this study are quartz-rich (>50 wt%) and clay-poor (<20 wt%) in contrast to sample B11, which is calcite-rich (>68wt%) (Table 1). Kaolinite is the only clay mineral detected by XRD across all of the samples. The proportion of kaolinite is very low (<7 wt%) for all samples except B8 (18 wt%). Except for sample B11, all shale samples also contain various proportions of carbonates (from 6 to 71 wt%), such as calcite and ankerite. Quartz and calcite are also the most variable phases, with the least variation being seen in clay minerals (except B8 with 18 % of kaolinite), muscovite, albite and pyrite (Fig. 4a).

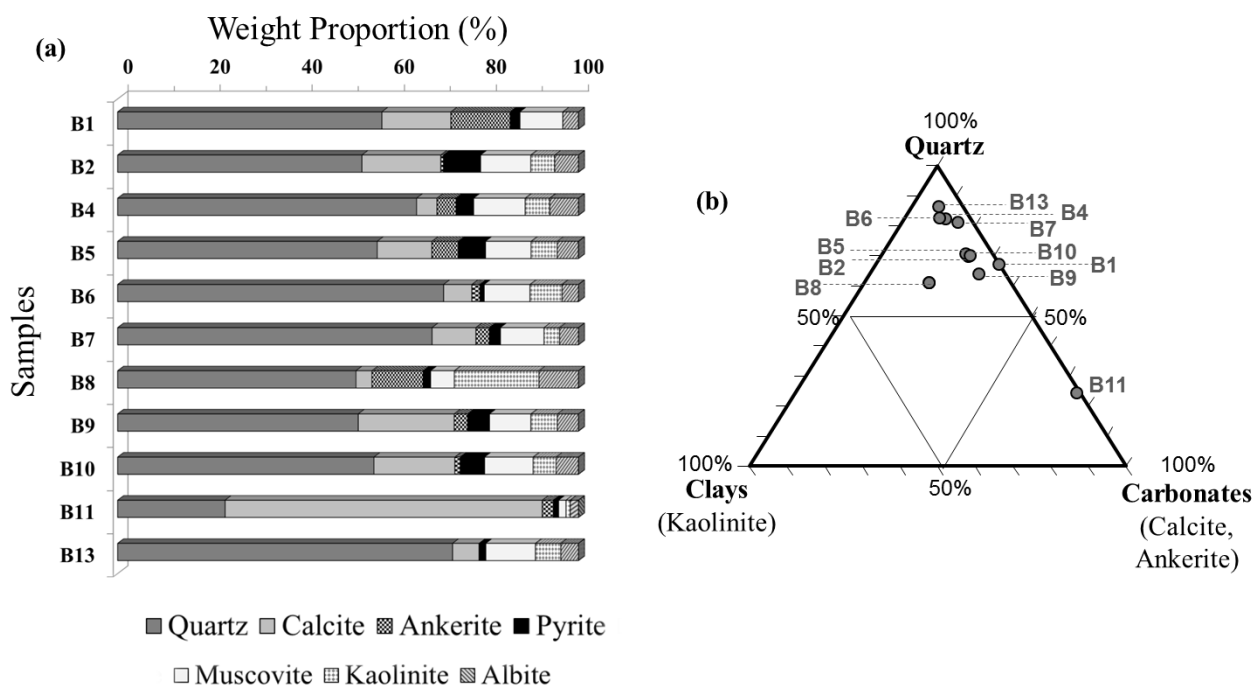


Fig. 4. (a) Variability of mineralogical composition of all samples, and (b) Mineralogy of all samples represented on a ternary diagram plotting proportions of clays, quartz and carbonates.

Despite the variation in mineral proportions (Fig. 4a), all shale samples display quartz-rich and calcite-rich mineralogies, independently of their TOC (Fig. 4b). The TOC values vary from 0.5 to 6.1 wt% for all the shales and the majority of samples have a TOC higher than 2 wt%, which is usually considered the lower level for potential oil and gas plays (Table 1) (Charpentier & Cook 2011). The TOC measurements were performed on centimetre-scale samples and are mean measurements, therefore local variability of organic matter content at smaller scales cannot be excluded.

4.2. Textural variability at the cm to μm scale

Micro-texture types were defined according to the thin section observations, on the basis of (a) the absence or presence of laminae, (b) lamina thickness, (c) grain type (mineralogy), (d) grain properties (e.g. size, orientation) and (e) the structure, content and nature of organic matter particles. Four main types were defined: unlaminated quartz-rich mudstone (type 1), interlaminated

quartz-rich mudstone (type 2), laminated quartz-rich mudstone (type 3) and weakly interlaminated calcite-rich mudstone (type 4). For each micro-texture type, one sample was selected to illustrate the microstructure. At the centimetre scale, the samples present various colors such as dark (B6), light to dark grey (B11, B1, B5, B8) or dark brown (B2), principally reflecting their organic matter contents (Fig. 5).

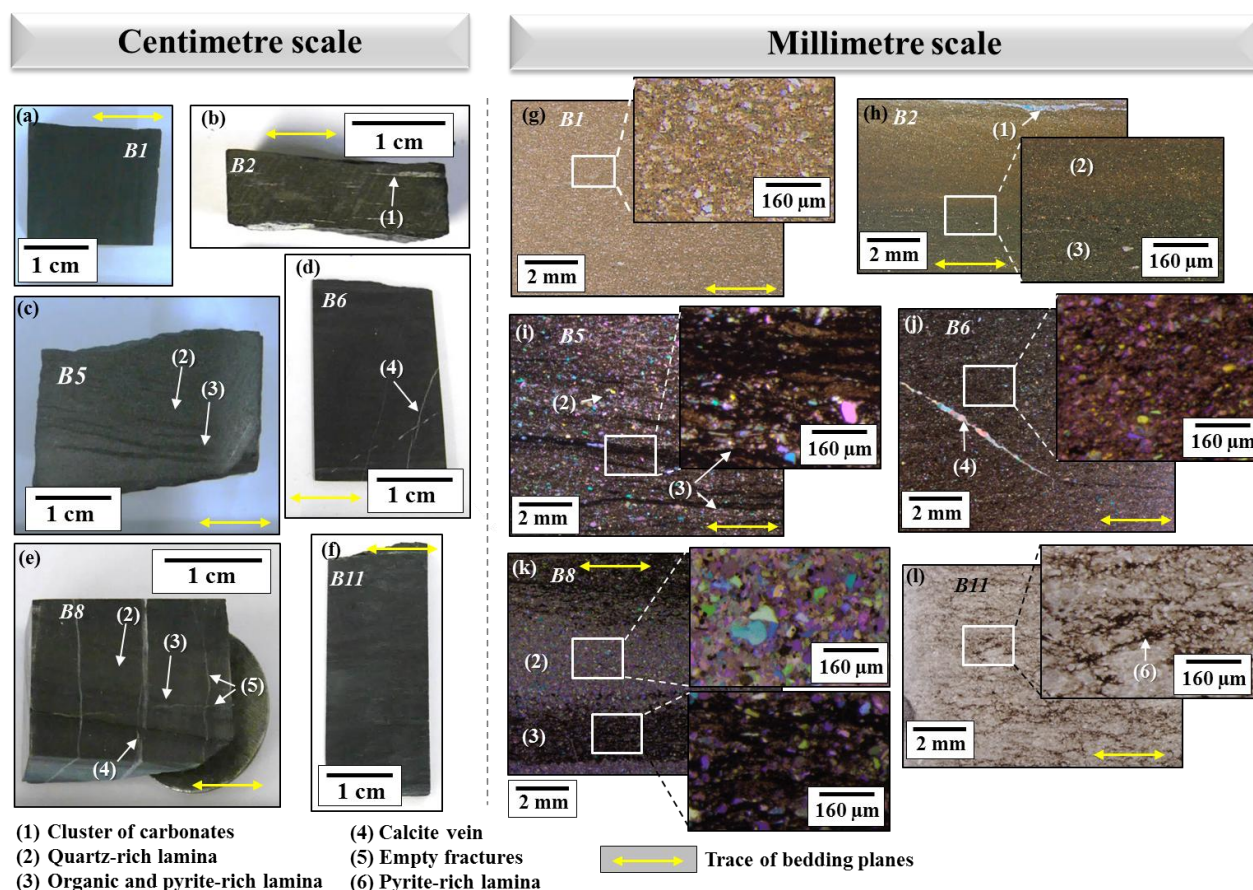


Fig. 5. Variability of mudstone micro-texture types of Bowland Shale from at the cm and mm scales : macroscopic views (a-f) and optical images (g-l).

The samples show variations of texture due to the presence of laminae (B5, B8), fractures sealed by carbonates (B6, B8), carbonate and quartz clusters (B2), and brittleness with open fractures (B8).

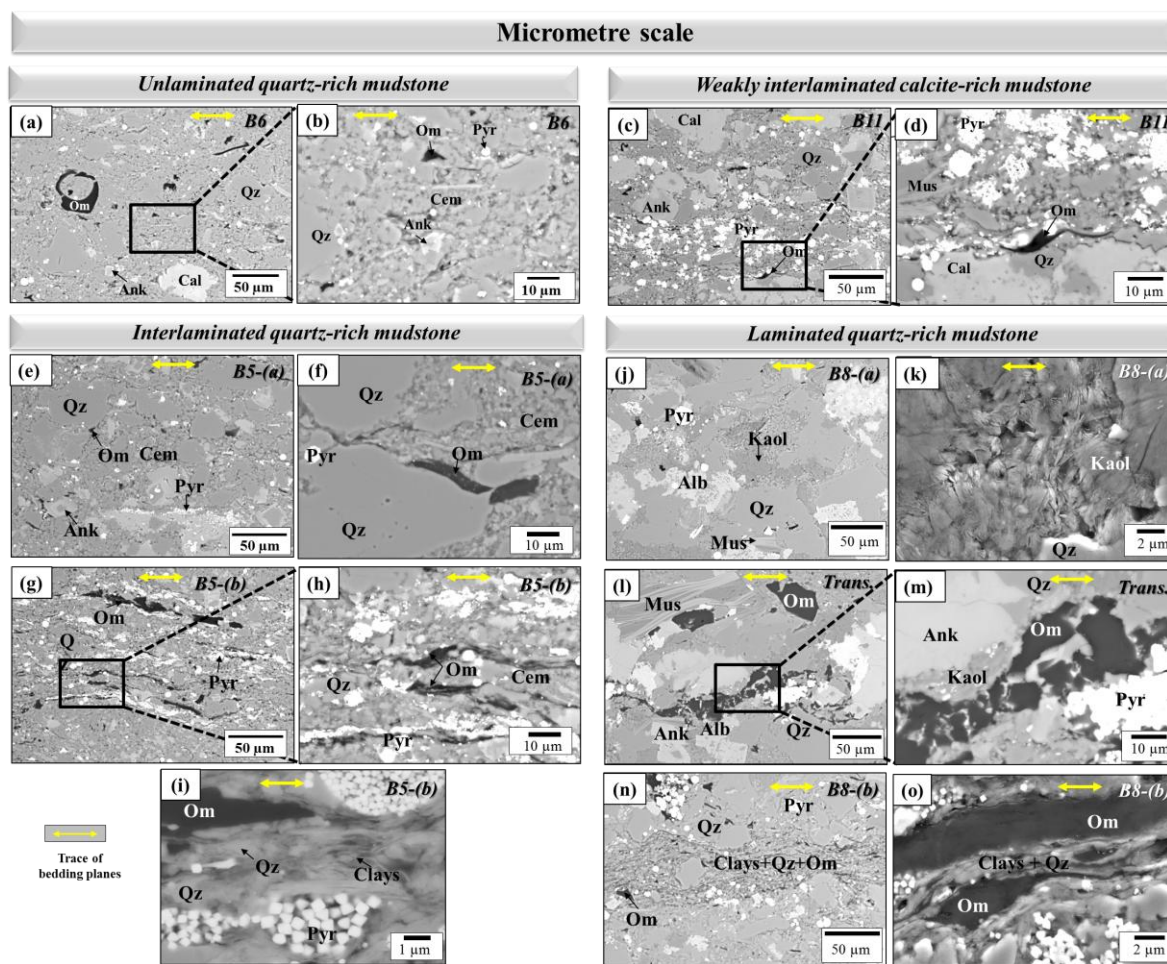


Fig. 6. Variability of mudstone micro-texture types of Bowland Shale at the μm scale by back-scattered electron (BSE) images under SEM : (a,b) unlaminated quartz-rich mudstone, (c,d) weakly interlaminated calcite-rich mudstone, (e-i) interlaminated quartz-rich mudstone, (j-o) laminated quartz-rich mudstone. [Cal: calcite, Qz: quartz, Ank: ankerite, Om: organic matter, Qz: quartz, Pyr: pyrite, Cem: cement, Kaol: kaolinite, Alb: albite].

Micro-texture type 1: Unlaminated quartz-rich mudstone (Samples B1 and B6)

Sample B6 forms a homogeneous unit from the centimetre to the millimetre scales. Calcite veins are present in B6 (Figs 5 d, j and 6 a, b). From the mm to μm scales, the grains of quartz and carbonates are dispersed within a fine crystalline quartz cement. The sizes of clastic grains vary from 10 μm to 50 μm in diameter. The quartz grains are in contact, unlike the carbonates and other grains. They are rounded with irregular shape, in contrast to the ankerite and muscovite grains

which are idiomorphic (Fig. 6 a, b). This micro-texture type contains mainly lithoclasts and does not possess any bioclasts. Quartz grains are divided in two types: the primary quartz in the lithoclasts, which probably results from the deposition of sediment, and the secondary quartz included in the cement and which fills in holes in carbonate grains and organic matter. The organic matter particles are randomly located at the mm scale (Fig. 6b). They are mainly micrometre-scale isolated particles and submicron particles mixed in the cement at the μm scale. Clay minerals (kaolinite) are located between the micrometre grains of quartz in the cement.

Micro-texture type 2: Interlaminated quartz-rich and pyrite-rich mudstone (B5, B2, B7)

At the centimetre scale, the interlaminated quartz-rich mudstone (Fig. 5 e-i) is heterogeneous due to the presence of periodic laminae, and the variation of their thickness and continuity. Two types of laminae are identified: (B5-a) grey quartz-rich lamina of millimetric thickness, and (B5-b) black organic and pyrite-rich lamina of around 100 μm thickness. The thickness of quartz-rich laminae is up to ten times that of the organic-rich laminae.

In B5-a (Fig. 6 e, f), the grains of quartz and carbonate display very various sizes (up to 100 μm). Quartz is particularly well-rounded and equant, unlike calcite which shows irregular shapes. Quartz and ankerite do not exhibit any evident shape preferred orientation. The largest calcite (>50 μm) and muscovite grains are elongate and oriented parallel to the bedding planes. The grains are held in a fine quartz cement in which detrital quartz grains are contiguous. Pyrite grains occur in randomly located framboid structures, with some assembled inside and/along the boundaries of calcite grains, parallel to bedding. The cement appears organic matter-poor at the μm scale.

In B5-b (Fig. 6 g-i), the grains of quartz and carbonates have qualitatively similar properties in terms of shape and orientation as B5-a, but their size is significantly smaller (around 10 μm). The pyrites are assembled into framboids which form dense and elongate layers hundreds of μm long, and lying parallel to the bedding planes. These assemblages of pyrite are interlaced with elongate micrometric organic matter particles, confirmed by their opacity under crossed polars OM (Fig. 5i).

Many submicron and elongate particles of organic matter are interlaced with submicron grains of quartz and clay minerals (Fig. 6 h, i).

Micro-texture type 3: Laminated quartz-rich mudstone (B8)

From the cm to the mm scales, the laminated quartz-rich mudstone is heterogeneous due to the presence of millimetre-size periodic laminae (Figs 5 e, k and 6 j-o). The laminae are quartz- (B8-a) and organic-rich (B8-b) but their mineralogy is different than the samples B6 and B5, previously described. These laminae are intersected by ankerite and calcite veins that cross-cut the bedding (Fig. 5j). The transition between laminae is progressive or sharp, which could be interpreted as gradual and rapid changes of depositional conditions, respectively.

B8-a is composed of large grains of quartz, feldspars (albite), muscovite, ankerite, calcite and framboidal pyrites. B8-a is strictly a siltstone and lithologically close to a sandstone, with grains of quartz and feldspar with a mean diameter between 50 and 100 μm , within a fine cement of quartz (Fig. 6j). Albite is altered and replaced by kaolinite, and filled by quartz cement, which suggests that this type of quartz is probably diagenetic (Bjorlykke and Egeberg, 1993; Schieber, 1996). B8-a contains large amounts of crystalline kaolinite (with no particular orientation), mixed with quartz and calcite grains in the cement (Fig. 6k). A few idiomorphic ankerite grains are present on and in replacement of calcite in veins. The organic matter is dispersed as submicron particles in the quartz cement, and in micrometric particles on pyrite boundaries. B8-a is organic-matter poor over the mm to μm scales. The concentration of large particles of organic matter increases in the transition of B8a to B8b (Fig. 6 l,m).

B8-b forms a heterogeneous unit with a lower mean quartz grain size ($<30 \mu\text{m}$), and multiple sizes and aspects of organic matter particles (Fig. 6 n, o). B8-b is feldspar-poor. The organic matter particles are present as very large (up to 100 μm) and elongate particles in the cement, orientated parallel to the trace of bedding, and as submicron particles between clay minerals (Fig. 6 n,o). The

clay minerals are arranged into localized and discontinuous elongate lenses approximately 50 μm thick.

Micro-texture type 4: Weakly interlaminated calcite-rich mudstone (B11)

At the cm scale, the weakly interlaminated calcite rich micro-texture type looks homogeneous (Fig. 5f). However, from the mm to the μm scales, irregular and discontinuous laminae are observed: (B11-a) calcite-rich laminae, and (B11-b) pyrite-rich laminae (Fig. 6 c, d). B11-a lamella are approximately millimetre thick and mainly composed of detrital calcite, authigenic calcite cement, ankerite, quartz and pyrite (Fig. 6 c, d). A small amount of clay minerals (kaolinite, but illite was also detected) is also present between the calcite and quartz in the cement. A few submicron organic matter particles are present in the cement without any preferential orientation at the μm scale. B11-b is composed of pyrite, phyllosilicates, quartz cement and orientated submicron-sized organic matter particles parallel to the trace of bedding. The framboidal pyrites form elongate and discontinuous layers, also aligned along the bedding trace with thicknesses varying from a few tens of μm to 100 μm . The quartz grains are divided into roughly equidimensional rounded grains and cement which fills the interstices between calcite grains.

4.3. Characterization of organic matter particles

An inventory of the different types of organic matter particles is shown in Figure 7.

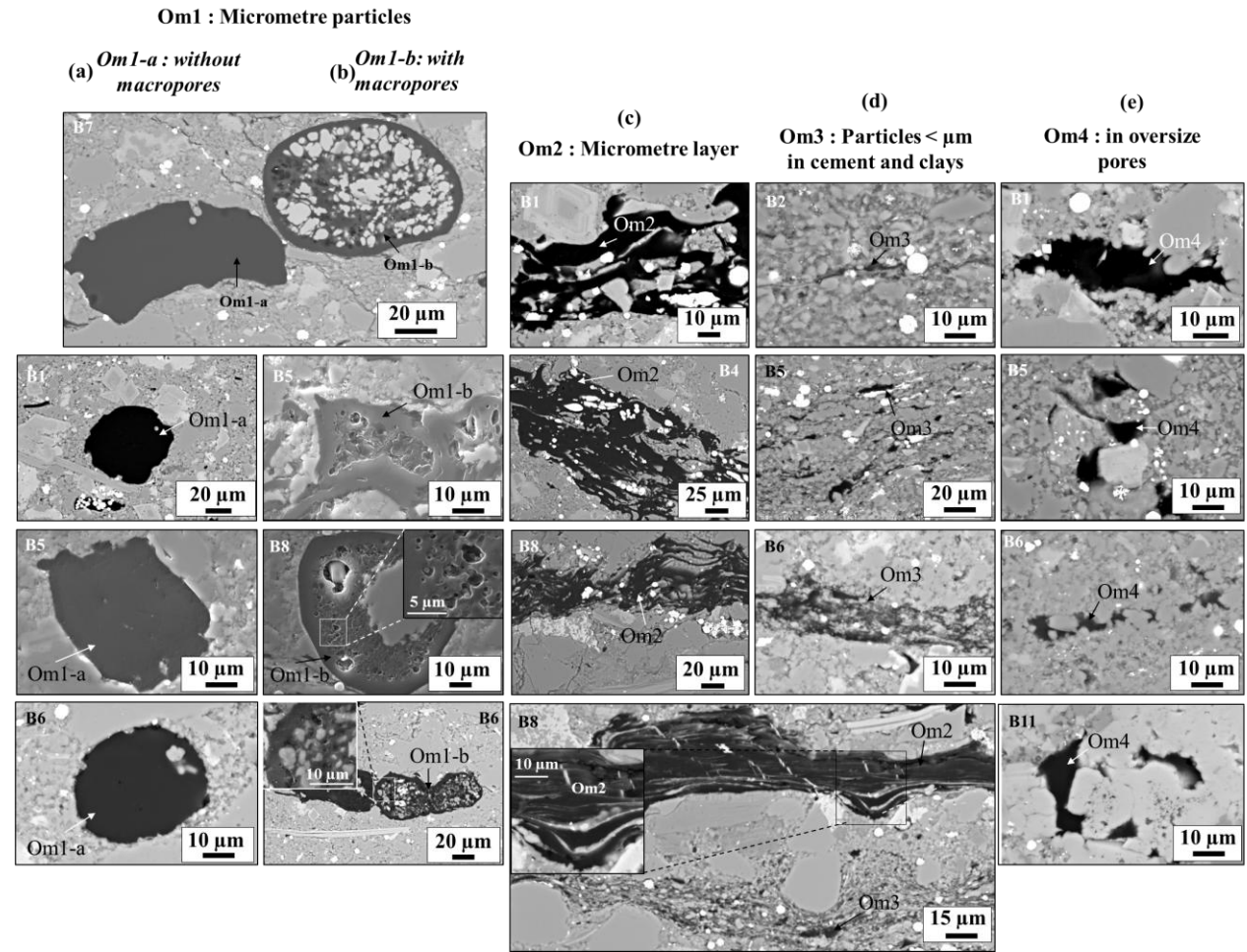


Fig. 7. Various types of organic matter particles in Bowland shale under SEM: (a) micrometric particles of organic matter without macropores (Om1-a); (b) micrometric particles of organic matter with macropores (Om1-b); (c) micrometric layers of organic matter (Om2); (d) Sub-micrometric organic matter particles in cement (Om3); (e) organic matter in oversize pores.

In the range of **all mudstone samples**, the organic matter particles are divided into four main types, as a function of their size and shape, the presence of macropores and their location:

Om1: micrometric particles. These particles are divided in two sub-types according to the presence or absence of macropores: **Om1-a** are organic matter particles of micrometric size and mainly equant and rounded, without macropores at the μm scale (Fig. 7a), and Om1-b which are organic matter particles of generally more than $10\ \mu\text{m}$ size, with random shape and macropores at the μm scale (Fig. 7b). They are partially cemented by quartz and calcite. Their shapes and the

presence of macropores suggest that they probably result from primary deposits of algal cysts (Leckie et al., 1990; Schieber, 1996). Om1-b pores are filled by diagenetic quartz (Schieber et al., 2000).

Om2: micrometre layers (Fig. 7c). Om2 is structured in dense layers (20-200 µm) parallel to the bedding trace and divided into a multiple set of lamellar and fibrous structures with a length up to a few hundred µm. It does not contain macropores. Pyrite is commonly present inside and on the boundaries of Om2 layers. Om2 is sometimes combined with Om1-a.

Om3: submicron particles between quartz and clays (Fig. 7 d). Om3 is composed of very small and elongate organic matter particles lying parallel to the bedding trace, in the quartz cement or in the clay matrix. Their orientation and shape suggest that they come from the same primary deposit as Om2.

Om4: organic matter in oversize (larger than average) pores (Fig. 7e). Om4 is present in abnormal and very irregular macropores larger than 10 µm. In samples B5 and B11, the shapes of these features could suggest that they result from mineral dissolution during burial, which allows them to behave as preferential pathways for organic matter during maturation. However, no gradual concentration of particular element deposits were found around these oversize pores to confirm this hypothesis.

4.4. Diagenetic precipitation of carbonate veins

Mineral vein features

Carbonate (calcite and ankerite) veins are present in samples B2, B4, B6 and B8. Most veins lie either perpendicular (B4, B6, B8) or parallel to bedding (B2, B8) (Fig. 8).

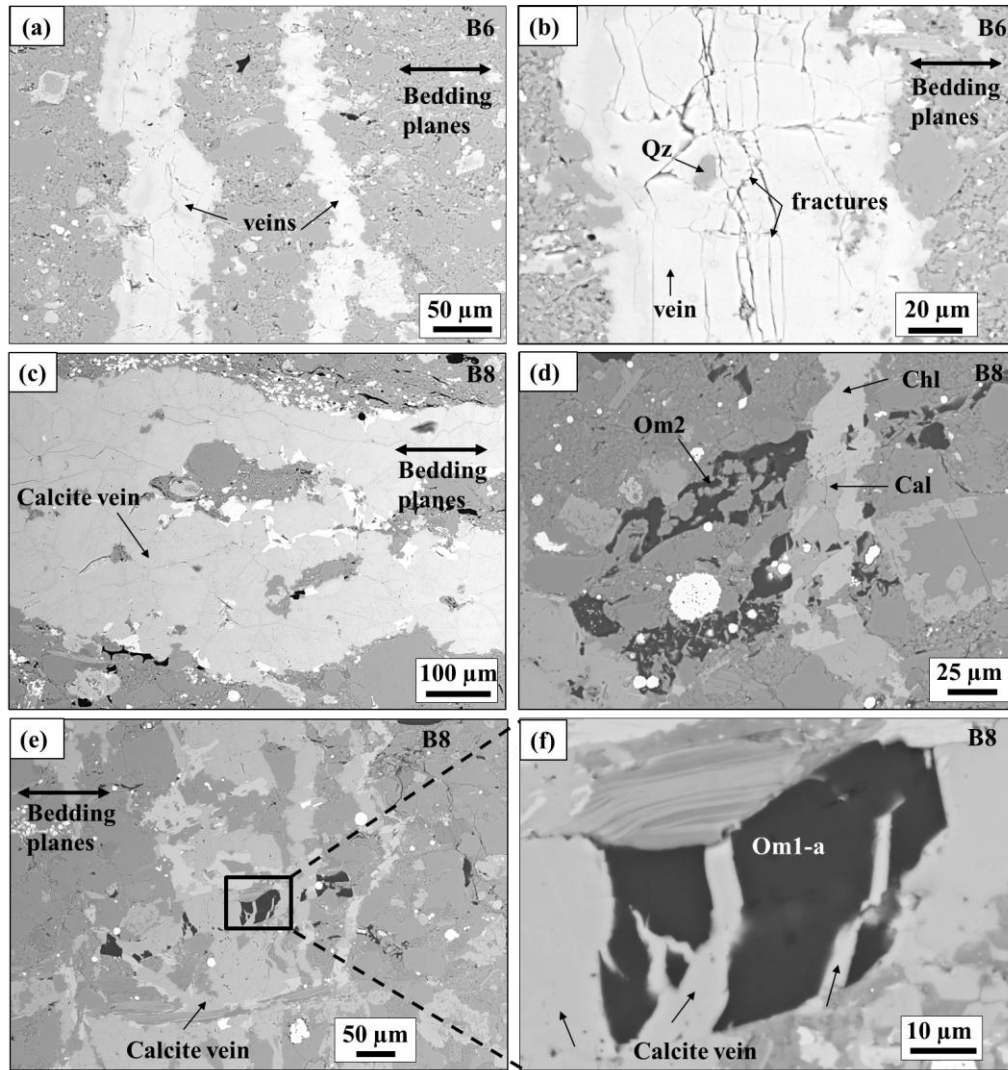


Fig. 8. SEM-BSE images of features attributable to fluid circulation in Bowland shale (examples from samples B6 and B8): (a) two veins of calcite perpendicular to bedding planes in sample B6; (b) fractures in vertical calcite vein in sample B6; (c) horizontal calcite vein in sample B8; (d) and (e) vertical veins of calcite which cross organic Om1-a and Om2 in sample B8; (f) close-up of the organic matter in (e). [Cal: calcite, Qz: quartz].

A few inclined veins are also found in sample B6 (Fig. 5j). These veins are 50 to 300 μm thick and a few centimetres long. Veins occur in a small number of thick fractures in B6 and B2 and in a set of abundant and narrow fractures in sample B8, separated by a few ten μm. The veins contain micrometre vertical and horizontal fractures in sample B6 (Fig. 8b). Figure 8 c-e shows that the calcite veins cross micrometric organic matter particles (Om1).

Ankerite and chlorite have partially replaced calcite in the veins of B8 and B6. Moreover, quartz cement is seen to have filled voids in calcite veins (Fig. 8b), demonstrating that quartz cementation has occurred after veining or that quartz co-precipitated with calcite (Fisher and Byrne, 1987; Fischer et al., 2009). Vein boundaries are sometimes associated with chlorite minerals in the laminated facies (B8) (Fig. 9 a, b).

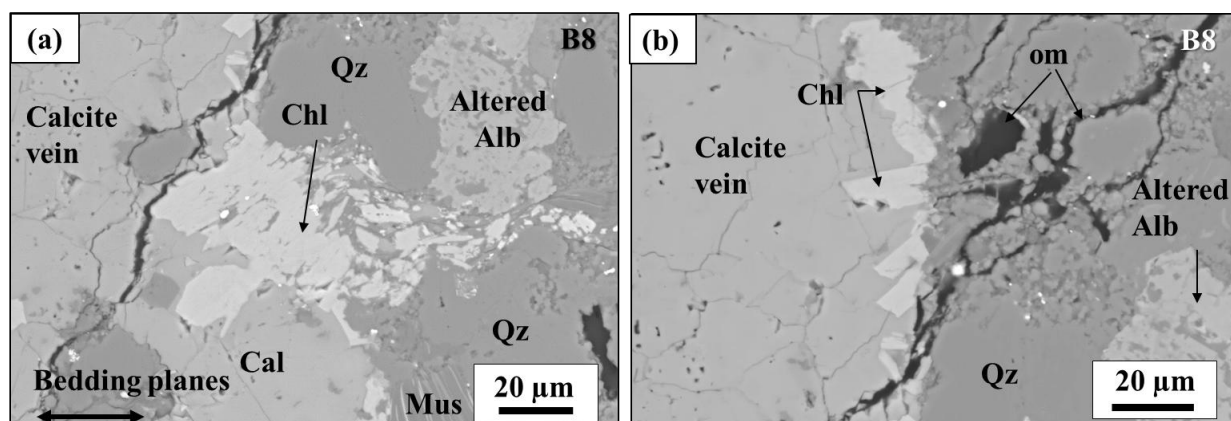


Fig. 9. SEM BSE images of (a) micrometric chlorite and altered albite on the boundaries of a calcite vein ; (b) well-shaped micrometric chlorite on the boundary of a calcite vein. [Chl: chlorite, Alb: albite, Qz: quartz, om :organic matter].

Where present, chlorite occurs as micrometric crystals around the margins of the calcite veins and within the quartz cement between feldspars and kaolinite (Fig. 9 a, b). The crystals are most commonly oriented parallel to the bedding planes. Their location around the veins suggests a formation subsequent to or contemporary with veining.

The calcite veins are partially filled by metal oxide deposits such as rutile, especially in sample B8 where the frequency of calcite veins is highest (Fig. 10 a, b).

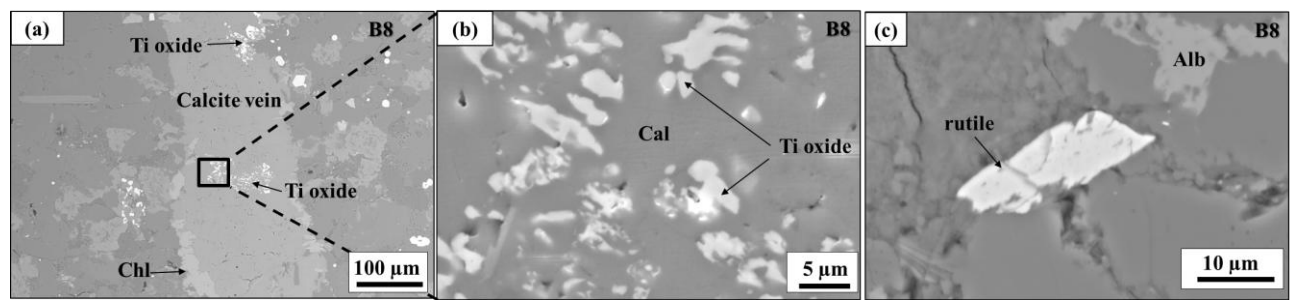


Fig. 10. SEM BSE images of (a) rutile inclusions in a calcite vein perpendicular to bedding planes in B8 at low magnification; (b) enlarged area of a) at high magnification ; (c) detrital rutile grain [Chl: chlorite, Alb: albite, Qz: quartz].

The rutile inclusions have irregular and smooth shapes with diameters varying between 2 and 10 µm (Fig. 10b). These inclusions are also present on the boundaries of veins, in the quartz cement around the veins and as trace minerals within aluminosilicates, especially in kaolinite. Titanium is also present as detrital rutile minerals in the cement (Fig. 10c). The presence of such titanium inclusions in calcite veins proves an authigenic formation by precipitation after veining. These vein inclusions also suggest that Ti-bearing fluid transport event occurred.

4.5. Mineral alteration and neoformation

Association of crystalline kaolinite and altered albite

Primary deposits of clays in shale are usually oriented with basal planes sub-parallel to the trace of bedding planes due to sedimentation and compaction. However, the kaolinite in sample B8 has no preferred orientation and displays large crystalline assemblages (greater than 10 µm) that are often associated with feldspars and quartz cement in quartz-rich laminae (Fig. 11 a, b).

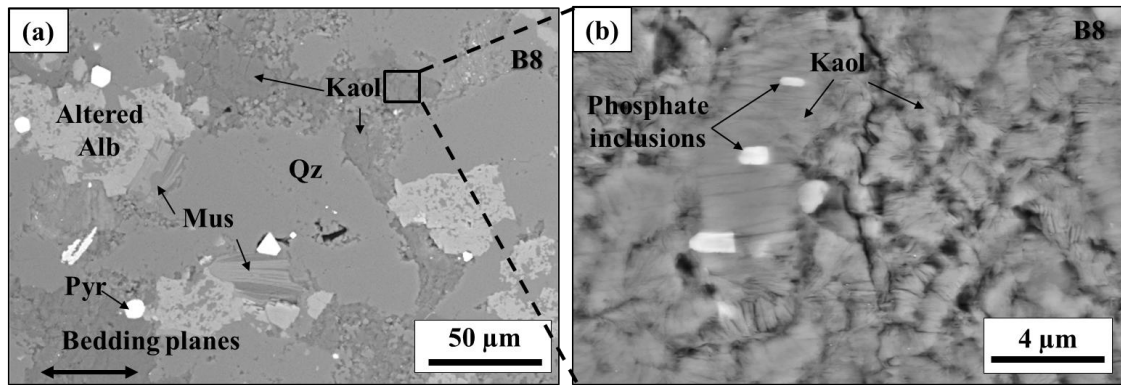


Fig. 11. (a) Randomly orientated kaolinite and muscovite mixed with albite and quartz; (d) large crystalline assemblage of kaolinite with phosphate inclusions in the quartz-rich laminae of B8. [Kaol: kaolinite, Alb: albite, Mus: muscovite, Cal: calcite, Qz: quartz, om: organic matter].

Albites are typically heavily altered, contain many holes partially filled by authigenic quartz, and are bordered by multi-micrometre “booklets” of kaolinite and muscovite. The frequent association of altered albite with authigenic kaolinite and quartz suggests the neoformation of kaolinite from the alteration of albite during burial (Oberlin and Couty, 1970; Boles and Franks 1979).

Idiomorphic ankerite

All shale samples except B2 contain, in various proportions and sizes, very well-formed crystallites of ankerite within the quartz cement, and mixed with calcite in veins. An example from sample B1 is shown in Figure 12a. The size of the ankerite crystals qualitatively varies from a few µm (B7, B8) to 20 µm (B1, B6, B5, B9, B10). The strongly idiomorphic shapes of ankerite and their random orientations suggest that they developed authigenically. Moreover, they crosscut the calcite veins, demonstrating that the ankerite crystals were formed subsequent to veining (Fig. 12 b, c). Quartz cement composed of multi-micrometric grains of quartz partially fills the calcite veins, and crosscuts or surrounds ankerite (Fig. 12 a, d), suggesting that ankerite formation was probably followed by a period of quartz cementation.

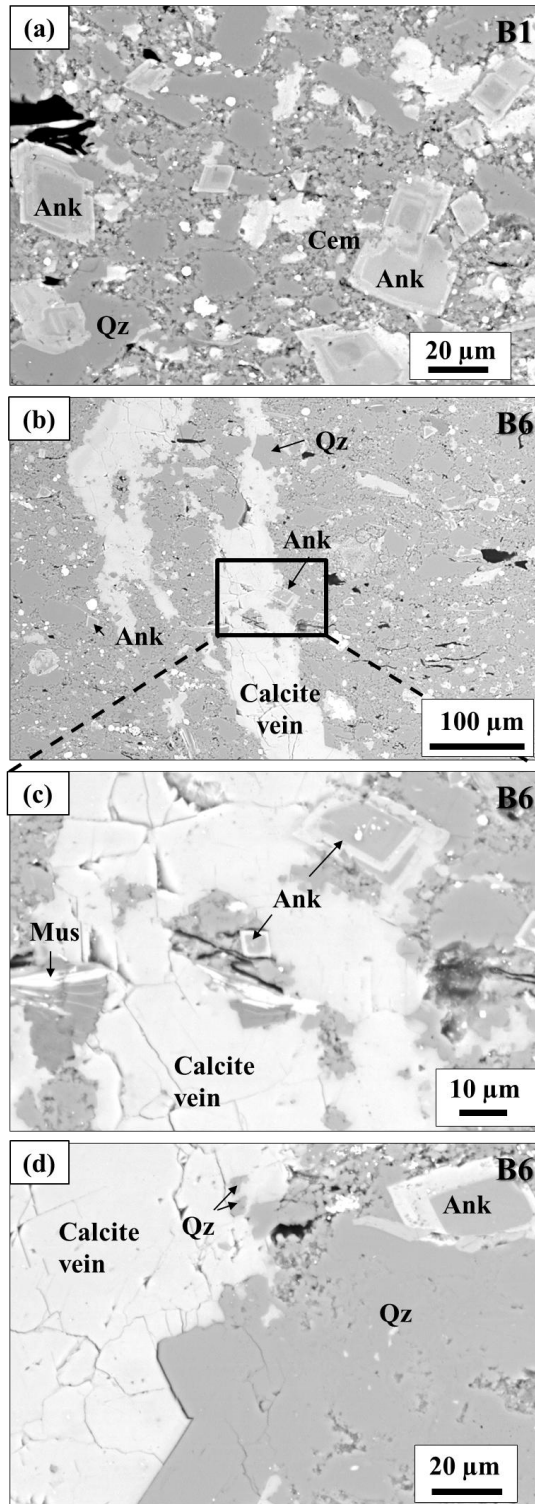


Fig. 12. SEM BSE images of: (a) well-formed ankerite crystallites in the quartz cement of B1; (b) ankerite crossing calcite vein in B6 sample ; (c) magnified view of of b) ; (d) quartz cement crossing well-formed ankerite crystallites and a calcite vein in B6 . [Kaol: kaolinite, Ank: ankerite, Mus: muscovite, Cal: calcite, Qz: quartz, Cem: cement].

319 **4.6. Variability of fractures**

1
2320 Knowledge of the fracture network is important for effective hydraulic treatment design (Gale and
3
4
5321 Holder, 2010). Natural fractures and mechanical discontinuities in general can affect the
6
7322 propagation of hydraulic fractures through delamination for example, which eventually causes
8
9
10323 opening of pathways under high pressure (Warpinski and Teufel 1987; Zhang et al. 2007; Gale et
11
12324 al. 2007; Gale and Holder, 2010).

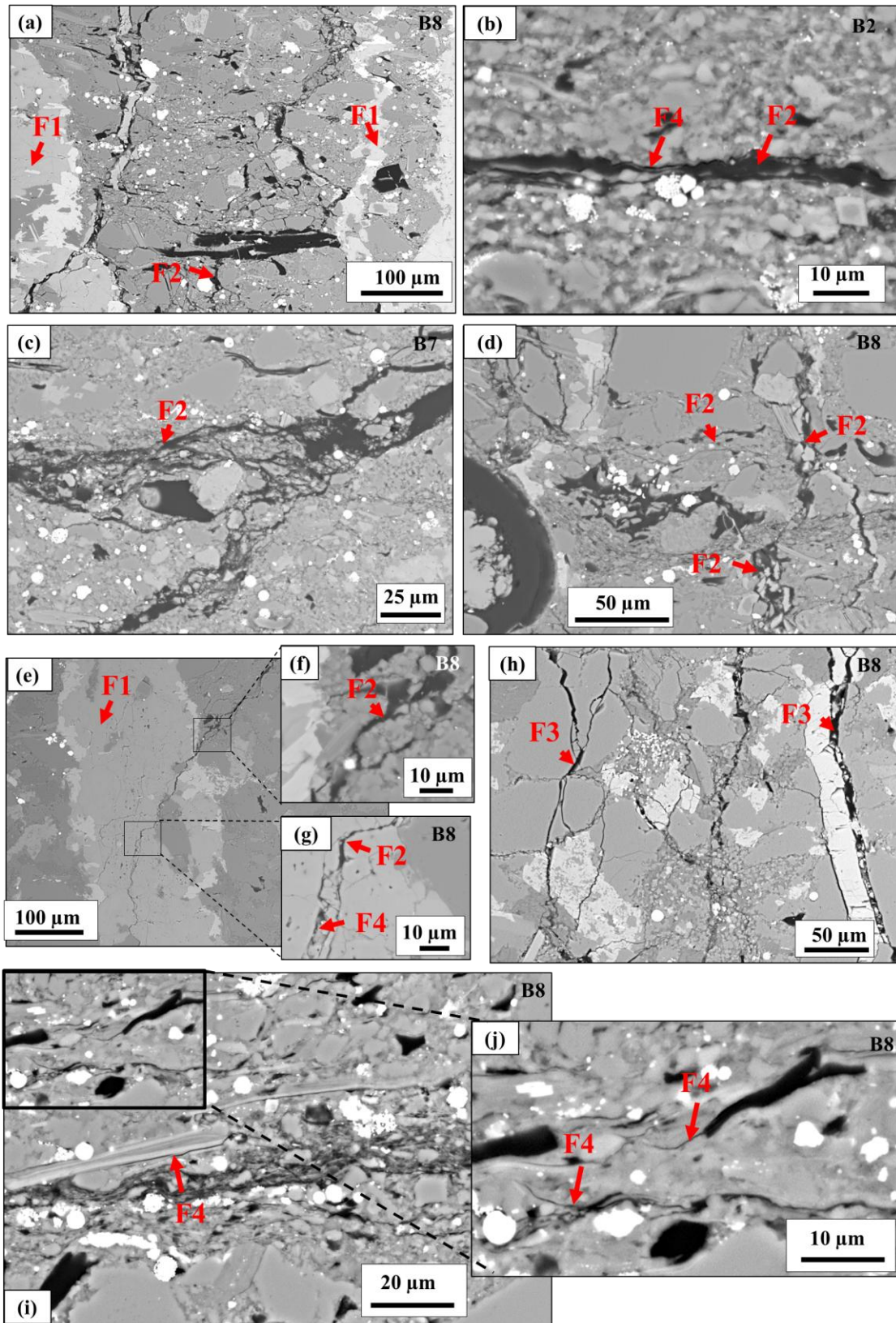


Fig. 13. Fractures (arrows) in Bowland shale. BSE images of : (a) calcite-sealed fracture F1; (b) horizontal bitumen-filled fracture (F2) and empty fracture (F4) along F2; (c) assemblage of thin F2; (d) horizontal and vertical F2; (e) F1 crossed by a bitumen-filled and empty fractures ; (f) inclined

F2 crossing F1 corresponding to the magnified view of (e); (g) vertical empty fracture in F1 in the continuity of F2; (h) resin-filled fractures (F3); (i) empty fractures along organic matter and micas; (j) empty fractures at the extremities of organic matter particles (Om3) in quartz cement.

In this study, four types of fractures were found in Bowland shale:

F1: Mineral-sealed fractures (Figs 8 and 13a). During post-compaction diagenesis, veins were formed as fractures filled with precipitated solids. In this case, the vein-filling phase is mainly calcite and ankerite, and can be termed calcite-sealed fractures. Note that the calcite veins previously described and the calcite-sealed fractures correspond to the same features. The majority of these sealed fractures lie perpendicular to bedding planes but inclined and horizontal fractures are also present. Gale and Holder (2010) showed that Barnett and New Albany shale (USA) samples with natural calcite-sealed fractures display tensile strengths less than 50% of that measured in samples without veins, and will always tend to fail along available fracture planes. Lee et al. (2015) also demonstrated that fractures preferentially refract in the middle of calcite veins during semicircular bending tests on Marcellus Shale. Calcite-sealed fractures are considered to be weak joints because calcite grows between non-carbonate grains without any cement with the border grains (Gale and Holder, 2010; Lee et al. 2015). Despite this tendency, Montgomery et al. (2005) considered that natural calcite-sealed fractures are insignificant for production in the Barnett shale (USA). Shales have usually undergone large amounts of compaction and porosity loss during progressive burial. Thus when vertical planar veins crosscut bedding their formation must have occurred post-compaction strain, when the rock became sufficiently brittle to host fractures.

F2: Natural fractures partially filled by organic matter (Fig. 13 a, b, c, d). The majority of these fractures lie parallel to bedding planes (Fig. 13 b, c), although a significant proportion is inclined or vertical (Fig. 13 a, d, e, f). The horizontal fractures are present in the cement along the boundaries of quartz, calcite, feldspar and mica grains, sometimes crosscutting calcite grains and detrital muscovite. They occur either as discontinuous thin, individual fractures from 1-2µm aperture,

continuous and individual fractures of 5-6 μm aperture (Fig. 13 b), or as a set of thin fractures forming a multi-micrometre fracture assemblage (Fig. 13 c) in the prepared samples. Sample B8 contains the greatest number of calcite veins examined, and a significant number of vertical fractures partially filled by bitumen and impregnation resin (Fig. 13 e-g). The bitumen-bearing fractures mostly lie within the organic-rich laminae, but some are also located along and inside calcite veins in the quartz-rich laminae (Fig. 13 e-g). Their aperture is very variable, from $<1\mu\text{m}$ to approximately 25 μm at the studied scales. A small number of fractures show brecciated aspects with a locally higher concentration of small grains of quartz and broken grains of micas, ankerite and calcite (Fig. 13 d).

F3: Fractures filled by resin (Fig. 13 h). These fractures are located in and on the boundaries of calcite veins, and in the quartz cement. Some of these fractures cut quartz and feldspars, and show brecciated aspects. These fractures transect calcite veins in sample B2, demonstrating that their formation was subsequent to veining. Because they became filled by resin and the sample was cut after impregnation, they could have been formed whilst the rock at depth. They are also likely to have been formed by release of in-situ stresses during extraction from the borehole. Their apertures are generally larger (several micrometres) and more homogeneous than the bitumen-filled fractures. Many of these fractures are connected (Fig. 13 h).

F4: “Empty” fractures (Fig. 13 b, g, i, j). Many of these fractures are horizontal, but vertical empty fractures are also observed. The horizontal empty fractures are located alongside or at the ends of organic matter particles (Om3) in the cement (Fig. 13 b), and at the boundaries of quartz or micas (Fig. 13 i, j). Their aperture is generally less than 1 μm . Figure 11 j shows a high rate of occurrence of these fractures in the cement of B8, but they appear discontinuous and unconnected in 2D. Empty fractures also occur as a continuation of bitumen-filled fractures (Fig. 13 e, g), following the direction of pre-existing fractures and cleavages in calcite veins. They may have been produced by stress release during sample recovery from depth, or during handling, but were too small to give easy access to the impregnation resin.

5. Interpretation and Discussion

5.1. Variability of microtexture

Implications for anisotropy and mechanical properties

The samples analyzed in this study display heterogeneous microstructures in terms of mineralogy, texture and TOC (Table 1, Figs 3,4). Even though the mean mineral proportions determined by XRD may be similar for all shale samples studied (e.g. all are quartz-rich), they have very variable microstructures owing to the presence of variable developments of periodic laminae from the μm to mm scale, which should be expected to cause strong and variable mechanical anisotropy. The comparison between the XRD, TOC, OM and SEM results thus emphasises the fact that XRD results alone are insufficient to classify the different shale samples. Petrographic observations can sometimes be superior to bulk analyses because the local variability of a range of parameters can be evaluated (Hackley and Cardott 2016). Key properties such as organic content, gas content and strength depend on such local variations of individual sedimentary facies (Cuss et al. 2015). It is relatively well-known that the mechanical properties (strength, elastic properties, dilatancy, creep...) of shale are dependent on several parameters such as mineralogy, grain shape and orientation, or porosity related to the orientation of bedding (Bjørlykke and Høeg 1997), and become apparent during unconfined or triaxial compression testing, or during thermal stimulation (Niandou et al. 1989; Ibanez and Kronenberg 1993; Naumann et al. 2007; Gutierrez et al. 2008; Sone and Zoback, 2013; Masri et al. 2014; Cuss et al. 2015; Bonnelye et al. 2016 a,b; Keller et al., 2017). The samples of Lower Bowland shale studied here are very anisotropic with a mineralogic banding plus shape and crystallographic preferred orientation of clays (organic-rich laminae), pyrite and individual organic particles, contrasting with silica-rich laminae. Furthermore, the development of a vertical spatial variability of micro-texture types with variable mineralogy and texture in the sequence of Lower Bowland Shale also induces a coarser vertical degree of development of anisotropy. The laminae have different thickness, from the μm to mm, and may be continuous or

discontinuous, which can lead to local variations of mechanical behavior. Laminae and micro-texture changes induce discontinuities and weak regions that can focus stress concentrations according to corresponding variations in elastic moduli (Lan et al. 2010, Amann et al. 2011), and may provide preferential ways for fracture growth. Variable degrees of development of clay mineral preferred orientation were observed, especially in the laminated micro-texture, ranging from kaolinite mineral grains that are randomly and horizontally arranged in quartz-rich and organic-rich laminae of the laminated mudstones, to laminae in which clay crystallites are strongly oriented as a result of mechanical compaction.

The studied Lower Bowland shale samples therefore display very anisotropic microstructures, but the degree of anisotropy varies with the micro-texture, mainly manifested as a variability of clay orientation and the thickness of laminae.

Primary depositional variability

The Lower Bowland shale samples correspond to hybrid shale in which elements of organic-pyrite-rich mudstone, organic sandstone (quartz-rich laminae of B8 for example) and organic siltstone are intimately interlayered. Turbidite facies have also been found in samples of Bowland shale retrieved from other boreholes (Waters and Davies 2006; Gross et al. 2015). The description of Lower Bowland microfacies herein has shown a wide variation of clastic and carbonate particle sizes and modal proportions, and also of TOC values. These observations reflect a primary variability of depositional controls within the basin, arising from glacio-eustatic fluctuations and tectonic events (Gross et al. 2015; Gawthorpe 1987; Holdsworth and Collinson 1988; Fraser and Gawthorpe 2003; Waters and Condon 2012; Gross et al. 2015).

5.2. High TOC and TOC variability in Lower Bowland shale

The majority of the studied shale samples have TOC higher than 2 wt%, between 1.1 and 6.1 wt% and with an average of 2.88 wt%. The presence of organic matter-rich samples confirms analyses reported in other recent studies (DECC 2010a; Charpentier and Cook 2011; iGas 2012; Andrews

2013). However, the alternation between organic matter-rich and -poor laminae probably acts to decrease the mean value of TOC and clay content at the cm and larger scales. As a consequence, the laminated samples (B7, B8) are classified as low TOC (<2 wt%) shales despite the presence of organic matter-rich laminae. In the same way, the local TOC values at the mm scale could be much higher than the results obtained by bulk TOC measurements at the cm scale for the samples displaying interlaminated facies (B5). SEM observations highlight the fact that the Bowland shale samples in this study contain narrow units (<1 mm) of higher-than-background TOC (but not quantified in this paper) from the μm to the mm scale, and qualitatively confirms the conclusions of Andrews (2013). Similarly, Maynard et al. (1991) measured TOC of two thin Namurian shales from the Upper Carboniferous basin of Northern England with local TOC up to 10 to 13 wt%, but these bands were interbedded within strata of 2 to 3 wt% TOC, which leads to a lower mean TOC.

5.3. *Quartz-rich and clay-poor Lower Bowland shale*

In this study, all shale samples examined are quartz-rich and clay-poor in comparison with some other samples of Bowland shales (ARI 2013; Andrews 2013; EIA 2015; Gross et al. 2015; Ma et al. 2016). Moreover, the clay minerals detected here are mainly kaolinite, whereas other Bowland shale samples may also contain a significant quantity of illite (Gross et al. 2015; Ma et al. 2016) and mixed layer minerals (Gross et al. 2015). In general, shale is predominantly composed of very fine grained particles within an indurated matrix, with or without laminations (Spears 1980; Bates and Jackson 1984; Jackson et al. 2007; Passey et al. 2010; Sondergeld et al. 2010a). Shale is formed by the compaction of clay minerals together with mud or silt-sized framework minerals (Bates and Jackson 1984), and associated with a substantial loss of porosity and development of fissility. A simple definition of shale for gas plays refers to a productive fissile rock containing a significant amount of organic matter from fine-grained rocks which can be carbonate, silica or clay-rich rocks such as the Haynesville, Barnett, Woodford, and Marcellus shales (USA) (Milner et al., 2010; Hammes et al., 2011; Chalmers et al., 2012). Loucks and Ruppel (2007) described shales

containing less than one-third clay minerals as siliceous mudrocks. Various definitions are found in the literature (e.g. Ougier-Simonin and Renard 2016) and the finest grains do not necessarily correspond solely to clay minerals. In the present study, the fine and detrital microstructure of all samples also includes various types of organic matter particles, giving mean whole-rock TOC higher than 2 wt%. Our samples were thus considered as shales even if their clay contents were to be less than 20 wt%. In these rocks, the detrital grains are mixed in a quartz cement rather than a clay matrix, although lenses of clays were also identified in some samples (B5, B8). A low proportion of clay minerals (<35%) is considered to be an advantage to facilitate hydraulic fracturing and gas extraction, because high proportions of tectosilicates (quartz), carbonates and other non-swelling minerals act to limit the rock ductility and to enhance brittleness (Jarvie 2014; Raji et al. 2015). However, Montgomery et al. (2005) and Ross and Bustin (2008) find an inverse relation between silica content and porosity in some areas of Muskwa and Besa River shales, demonstrating that silica content and ability to fracture should be considered alongside other characteristics while estimating potential resource capacities.

Canadian shale from the Muskwa and the Lower Besa River shales in northern British Columbia display similar bulk mineralogy to the Bowland samples used in this study (Ross and Bustin 2008). They are silica-rich (from 58 to 93 wt%), TOC-rich (up to 5 %), and the lowest quartz contents are associated with carbonates such as dolomite (around 40 wt%). Moreover, **clay minerals represent only 1 to 25 wt%**. As with Besa River and Muskwa shales, Bowland shale samples are composed substantially of detrital silica, but subsequent cementation and replacement crystallization of quartz can make the identification of primary silica grains difficult. Consequently, the origin of some of the silica (quartz) is difficult to explain for the Bowland shale samples presented here. The presence of organic matter derived from algal cysts demonstrates a marine depositional environment, but the absence of siliceous fossils such as radiolaria and other microfossils suggests that the high quartz content is not due to biogenic activity.

5.4. Fluid passage and temperature-driven reactions during burial

Using the cross-cutting principle, different events identified can be qualitatively ordered in time sequence. There are (a) feldspar alteration and neoformation of kaolinite, (b) calcite veining, (c) ankeritization of calcite, (d) quartz cementation and (e) organic matter migration through fractures. These features demonstrate a likely late or post diagenetic circulation within or passage of fluids through these Bowland shale samples, accompanied by veining and mineral alteration at low temperatures. It was followed by a second circulation of hydrocarbon-bearing fluids at higher temperatures. These events were not necessarily followed precisely one by the other, but could be partially concurrent in some cases. The description of these events (below) provides preliminary qualitative data on the burial conditions and maturation of Bowland shale in the Preese-Hall-1 borehole, but these conditions must be further studied on a significant quantity of samples from various locations before being generalized for the Bowland shale basin.

Veining episode

Calcite-veins (F1) crosscut all types of laminae, indicating a displacement of fluids subsequent to primary sediment deposition and compaction. Silica-bearing fluids are presumably expelled from greater depths in the sediment pile as a result of the final stages of compaction and diagenetic reactions. The general planar orientation of veins normal to the compaction fabric demonstrates that the veining occurred in the fully-compacted and indurated host-rock. Experimental observations of mechanical compaction and study of natural shale-bearing basins shows that most compaction is completed by much less than 1 km of burial (Rutter et al. 2017). The orientations observed of the calcite veins suggest a simple, transversely isotropic stress field arising from compaction under the weight of overburden. In the range of samples studied, the majority of veins lie perpendicular to bedding planes, forming a vertical polygonal network (although some horizontal and inclined veins are present), indicating that the maximal principal stress arose from the vertical load. Compaction-induced pore fluid overpressuring occurs when the fluid pressure rises to become very close or equal to the least principal stress during burial. In transversely isotropic loading there is little

difference between the least and the intermediate principal stresses in the horizontal plane. In low permeability rock such as shale, fluid cannot be rapidly expelled from the pores, therefore pore pressure may rise sufficiently to cause vertical hydrofracture formation, perhaps assisted by horizontal crystallization pressure if minerals grow in the veins from locally supersaturated solutions. The possibility of penecontemporaneous fracture along bedding planes can also arise, allowing the formation of horizontal calcite veins in shale owing to the lower fracture toughness for bedding-parallel fracture. It can result of the bedding anisotropy coupled with a low differential stress as a consequence of creep deformation, also promoted by a high pore fluid pressure (Stoneley 1983). However, the absence of organic matter inside the calcite veins (at the μm scale), and the dominance of vertical veins suggest that a relatively high vertical principal stress suppressed significant formation of bedding-parallel veins. Horizontal calcite veins can also form in rocks via the Poisson ratio effect when differential stresses have been relaxed by creep and there is a degree of vertical depressurization through an erosional episode.

The Visean shales of the Bowland basin were deposited during the syn-rift stage of a Lower Carboniferous back-arc basin, and are restricted to graben and half-graben separated by platforms and tilt-block highs (Leeder 1982, 1988; Warr 2000; Waters and Davies 2006). The Namurian shales were deposited in the subsequent thermal subsidence stage (Leeder 1988; Waters and Davies 2006), which is emphasized at small scales with localized extension and compression episodes in the Pennine Basin in Northern England (Waters et al. 1994). Rocks of the Craven group, which includes Visean and Namurian shales in the Bowland sequence elsewhere in the basin, was subjected to tectonic activity during the late Chadian to early Arundian and from the late Asbian until the early Brigantian stages. Evidence of hydrothermal precipitation is very poorly documented within the scientific literature on the Bowland sequence, and it is difficult to discern how long after deposition the carbonate veining occurred. Isotopic and dating measurements of calcite minerals would be required to resolve this question.

In shales, the formation of calcite veins usually occurs at temperatures between 20 and 60°C at shallow to intermediate burial depths (up to hundreds of meters deep) (Al-Aasm et al. 1992), but formation of calcareous mineralization at up to 2.3 km depth has been inferred for some shale formations, such as the middle Devonian shale from the Appalachian plateau (USA) (Evans 1995).

Clay minerals

Quartz-rich laminae within laminated facies contain significant quantities of altered albite, together with micrometric kaolinite with “booklet” shapes. Alteration of detrital albite to authigenic kaolinite in shale is commonly due to a temperature-dependent reaction and pore fluid interactions during burial (Boles and Franks, 1979; Tieh et al., 1986). This reaction occurred in Wilcox shale at temperatures between 100 to 120 °C (Boles and Franks 1979). In the present study, the samples show that a first type of kaolinite resulted from primary deposition (oriented crystals in organic-rich laminae) and a second type (randomly oriented authigenic kaolinite in quartz-rich laminae) that corresponds to the alteration of feldspars (albite).

Ankerite neoformation and quartz cementation

At temperatures higher than 100 °C, iron and magnesium in solution may react with kaolinite to produce chlorite, and/or with calcite to produce ankerite (Boles and Franks 1979). Iron and magnesium generally originate from illitization. Ma et al. (2016) found 23 wt% of illite and 2 wt% of kaolinite in Bowland shale sourced from the Swinden borehole in the west of the Bowland basin. Illite is not present in the XRD analyses of the samples studied here, whereas a few illite grains are seen in a small number of SEM images (in B5 for example). As a result, the sources of iron and magnesium are not yet understood. In general, ankerite is more abundant in sequences of thin sandstones associated with thick shale layers, than it is in thick sandstone layers (Boles and Franks 1979). This generalization was confirmed to be the case for the Bowland shale in Preese Hall-1 by the laminated and interlaminated micro-texture types, and agrees with the observations and inferences of Waters and Davis (2006) and Andrews (2013). Their strong crystallographic forms

and their location in veins as a calcite substitute suggest an authigenic origin and formation subsequent to veining.

Quartz cement partially infills calcite veins and crosscuts authigenic ankerite minerals, revealing that quartz cementation was a late event, occurring after veining and ankerite formation. The presence of veins, crystalline quartz cement and crystalline kaolinite, plus Ti and Fe oxides inside veins, may also imply a passage or circulation of fluids through these laminae, and may partially explain the feldspar alteration to kaolinite.

The quartz cementation is particularly present in quartz-rich laminae of the laminated mudstones which are siltstone to sandstone according to their grain size, and in the unlaminated mudstone samples. In relatively porous, quartz-rich sandstones, large volumes of water can pass through the pore system, permitting cementation in areas where pressure solution is absent (Boles and Franks 1979). Siltstone, sandstone and mudstone are usually studied independently but in our case, they are dispersed periodically and vertically throughout the sample set. In the Wilcox sequence in Texas (USA), the majority of pore waters derived from the original compaction of shale moved through the (more permeable) interbedded sandstones, despite shales representing the majority of the stratigraphic section (Burst 1969). Waters passing from shales to siltstone and sandstones during diagenesis should facilitate chemical component transfers, which may enable the formation of sandstone cement (Curtis 1978; Boles and Franks 1979). The laminated mudstone microtextures of the Bowland shale samples presented here are composed of organic-rich laminae, wherein detrital grains are mixed in a fine cement of quartz and clay lenses, interbedded with quartz-rich laminae, which appear similar to quartz-cemented siltstone and sandstones. These quartz-rich laminae are composed of large grains of quartz cemented by fine-grained quartz grains. Following a hypothesis of Curtis (1978), water could pass from the organic-rich to quartz-rich laminae and its transfer could facilitate the quartz cementation. The very low clay content in Bowland shale samples allows us to admit this hypothesis as possible. However, a low content of primary clay minerals does not necessarily mean that porosity and permeability are high enough to permit this

process. Porosity and permeability data are few for Bowland shale (Andrews 2013), but are commonly very low in shale formations (e.g. Rutter and Mecklenburgh 2017), hence the latter hypothesis could also explain the quartz cementation. The SEM observations suggest that the quartz cementation occurs late, after the veining and ankerite formation (if there is only one period of cementation).

5.5. Organic matter migration during thermal maturation

Migration through fractures

The samples studied here show a high variability of fracture types, in terms of their content (carbonate, bitumen, resin, empty), orientation and size. The opening of fractures generated by the expansion of organic matter is traditionally thought to be caused by pore fluid overpressuring through organic decomposition and petroleum generation, which happens in the 80-150 °C temperature range (Bjørlykke 2010; Kobchenko et al., 2011; Goultly et al., 2012). Very low heating rates between 1-2 °C/Ma have been inferred, but sometimes reaching as high as 10 °C/Ma (Bjørlykke 2010). The late bitumen-filled fractures F2 crosscut the shale microfabric, ankerite grains, quartz cement and carbonate veins, showing the migration of organic-matter occurred subsequently to the formation of all these features.

Fracture orientation

In shales in general, bitumen-bearing horizontal fractures are significantly more common than vertical fractures. For example, horizontal bitumen-filled fractures are found in the clay matrix of organic-rich laminae in the lower half of the Upper Devonian Dunkirk Shale alongside a smaller population of vertical bitumen-filled fractures (Lash and Engelder 2005). These fracture populations also typify the Oligocene Frio shale (Capuano 1993) and Upper Devonian Strachan shale in the Alberta basin (Marquez and Mountjoy 1996) in the USA. The majority of their bitumen-filled fractures are oriented parallel to the bedding planes. This is an important initial

anisotropy caused by the horizontal laminae and clay grain fabric and by many kerogen grains lying flattened parallel to bedding, which can correspond to Om2 and Om3 in our case. When interconnected, these horizontal fractures may aid the migration of hydrocarbons into reservoir rocks (Momper 1978; du Rouchet 1981; Talukdar et al. 1987; Ozkaya 1988; Capuano 1993; Marquez and Mountjoy 1996; Lash and Engelder 2005).

The Upper Devonian Strachan shale in the Alberta basin (USA) and the black shale of the Bluefish basin (Canada) also feature many horizontal fractures (Al-Aasm et al. 1992; Marquez and Mountjoy 1996). Diagenesis generates vertical compaction and smaller induced horizontal stresses during burial, but the horizontal stresses may become larger than the vertical stress as a result of differential stress relaxation during creep, coupled with removal of overburden through erosion, which will facilitate the formation of late horizontal fractures along bedding planes (Turcotte and Schubert 2002; du Rouchet 1981; Spencer 1987).

The Bowland shale samples contain horizontal bitumen-filled (F2) and empty fractures (F4) which are very similar to those observed by Lash and Engelder (2005). However, the samples also contain a significant number of vertical bitumen-filled fractures, especially in dense calcitic-vein areas as in sample B8, and unlike the North American shales described above. Moreover, the vertical bitumen-bearing fractures (F2) systematically crosscut calcite veins and isolated calcite grains in the cement. These late, radially distributed, vertical bitumen-bearing fractures were interpreted to have formed from fractures branching from pre-existing calcite veins owing to reduced fracture toughness at their margins.

6. Conclusions

In this study the variability of the microstructure of the Lower Bowland shale was highlighted from the cm to μm scale using the traditional techniques of microscopy combined with XRD and TOC measurements. The samples show a high variability of : (i) micro-texture types (unlaminated, interlaminated and laminated quartz-rich mudstones and weakly interlaminated calcite-rich

mudstone), (ii) mineralogy, (iii) TOC (from 0.5 to 6.1 wt%), (iv) organic-matter particles (micrometric particles with and without macropores, multi-micrometre layers, submicrometre particles in the cement and particles in oversize pores), and (v) fractures which are organized in a complex network (calcite-sealed, bitumen-filled, empty and resin-filled fractures). The planar geometry of the vertical veins means that the rock was compacted and lithified prior to the formation of the carbonate-sealed fractures. The vertical bitumen-bearing fractures were interpreted as being due to the influence of weak joints generated by the previous carbonate veining episode, which increases the brittleness of the shale. Moreover, the microstructural and mineralogical heterogeneities in areas heavily affected by veins may preferentially facilitate formation of open fractures (resin-filled and empty) during specimen recovery and handling.

The majority of samples are quartz-rich and high TOC (>2 wt%). Some samples have low overall TOC but their microstructure shows local cyclicity between organic-rich and organic-poor laminae. This confirms the presence of narrow (<1 mm) and periodic, qualitatively organic-rich deposits in Bowland shale as has been previously suggested in the literature. The low clay content (<20wt%), the high detrital and cemented quartz content (>50wt%), and the presence of a complex and multi-scale fracture network support the developing interest in the Lower Bowland shale as a potential hydrocarbon resource.

The planar geometry of the vertical calcite veins means that the rock was already compacted and lithified before the carbonate-sealed fractures could form. Subsequently, mineral replacements and authigenic growths of clay minerals and secondary carbonate grains (calcite and ankerite) formed. Later, horizontal bitumen-bearing fractures provided routes for hydrocarbon migration and may have formed as maximum principal stress became horizontal as a result of stress relaxation during creep coupled with erosional offloading. The vertical bitumen-bearing fractures were interpreted as being due to the influence of weak joints generated by the previous carbonate veining episode, which increases the brittleness of the shale. The microstructural and mineralogical heterogeneities

in areas heavily affected by veins may have preferentially facilitated formation of open fractures (resin-filled and empty) during specimen recovery and handling.

The identification of various micro-texture types and their heterogeneities in terms of mineralogy and structure (fractures, laminae) will aid the selection of specific types of samples for 2D and 3D high-resolution imaging in the cement and clay lenses, and for geomechanical characterization. In the same way, the description of the various organic matter particles should guide the selection of key particles for characterization of the pore network within kerogen and bitumen-filled fractures. Evidence of a range of geological episodes such as carbonate-veining, feldspar alteration to kaolinite, ankerite neoformation and bitumen-driven fracturing highlight periods of fluid passage or circulation within the Bowland sequence and temperature-driven reactions occurring during burial, for over the temperature range between approximately 30 and 150 °C. The evidence presented here provides new aspects to aid understanding of the geological history of the Lower Bowland sequence, which should aid in the development of a more generalized understanding of the sequence through future studies across larger sample quantities.

In future studies of Lower Bowland Shale microstructure, a regular separation distance between the samples should be taken and further observations of the cement should be made to evaluate the connectivity of the various fractures, especially the numerous horizontal micrometer-scale empty fractures F4, and to make a better estimation of mineralogy and modal fraction of clays present.

Acknowledgments

The following people contributed to the completion of this paper: Dr Katie Cunnea, Dr Alex C. Leung, Dr Sara Nonni and Mr Paul Waters. We thank the British Geological Survey (Nottingham, UK) for the Bowland Shale samples. This project has received funding from the European Union's Horizon 2020 716 Research and Innovation Programme under the ShaleXenvironment project, (grant no. 640979), with facilities and support also provided by the Research Complex at Harwell,

680 funded in part by NERC (NE/M001458/1) and EPSRC (EP/I02249X/1). Data Statement:
1
2 681 representative research data is presented in the images and graphs in this manuscript.
3
4
5
6
7
8
9
10
11
12
13
14
15
16
17
18
19
20
21
22
23
24
25
26
27
28
29
30
31
32
33
34
35
36
37
38
39
40
41
42
43
44
45
46
47
48
49
50
51
52
53
54
55
56
57
58
59
60
61
62
63
64
65

References

- 1 Abrams, M.A. 2014. Petroleum System Charge Analysis for Liquid-Rich Unconventional Plays.
2
3
4
5 *Unconventional Resources Technology Conference (URTEC)*.
6
- 7 Al-Aasm, I.S., Muir, I. and Morad, S. 1992. Diagenetic conditions of fibrous calcite vein formation
8
9 in black shales: petrographic, chemical and isotopic evidence. *Bulletin of Canadian Petroleum*
10
11
12 *Geology*, **41(1)**, 45-56.
13
- 14 Amann, F., Button, E.A., Evans, K.F., Gischig, V.S. and Blümel, M. 2011. Experimental study of
15
16 the brittle behavior of clay shale in rapid unconfined compression. *Rock mechanics and rock*
17
18
19 *engineering*, **44(4)**, 415-430.
20
21
- 22 Andrews, I. J. 2013. The Carboniferous Bowland Shale gas study: geology and resource estimation.
23
24
25
26 *NERC report*.
27
- 28 Bates, R. L., and Jackson, J. A. 1984. Dictionary of geological terms. Third Edition. *Anchor Books*,
29
30
31 *New York*.
32
- 33 Bjørlykke, K. and Høeg, K. 1997. Effects of burial diagenesis on stresses, compaction and fluid
34
35 flow in sedimentary basins. *Marine and Petroleum Geology*, **14(3)**, 267–276.
36
- 37 Bjørlykke, K. (2010), *Petroleum Geoscience: From Sedimentary Environments to Rock Physics*,
38
39
40
41 Springer, Berlin, Germany.
42
- 43 Boles, J.R., and Franks, S.G. 1979. Clay diagenesis in Wilcox sandstones of southwest Texas:
44
45
46 implications of smectite diagenesis on sandstone cementation. *Journal of Sedimentary*
47
48
49 *Research*, **49**.
50
- 51 Bonnellye, A., Schubnel, A., David, C., Henry, P., Guglielmi, Y., Gout, C., Fauchille, A.L. and
52
53
54
55
56
57
58
59
60
61
62
63
64
65

- Bonnelye, A., Schubnel, A., David, C., Henry, P., Guglielmi, Y., Gout, C., Fauchille, A.L. and Dick, P., 2016. Elastic wave velocity evolution of shales deformed under uppermost - crustal conditions. *Journal of Geophysical Research: Solid Earth* **131**, doi : 10.1002/2016JB013540.
- Borer, J.M. and Harris, P.M. 1991. Lithofacies and cyclicity of the Yates Formation; Permian Basin: implications for reservoir heterogeneity. *AAPG Bulletin*, **75(4)**, 726–779.
- Burst, J.F. 1969. Diagenesis of Gulf Coast clayey sediments and its possible relation to petroleum migration. *AAPG bulletin*, **53(1)**, 73-93.
- Capuano, R. M. 1993. Evidence of fluid flow in microcracks in geopressed shales. *AAPG Bulletin*, **77(8)**, 1303–1314.
- Caracciolo L., Arribas J., Ingersoll R.V. and Critelli S. 2013. The diagenetic destruction of porosity in plutoniclastic petrofacies: The Miocene Diligencia and Eocene Maniobra formations, Orocopia Mountains, southern California, USA. In: Scott, R. A., Smyth, H. R., Morton, A. C. & Richardson, N. (eds) *Sediment Provenance Studies in Hydrocarbon Exploration and Production*. Geological Society, London, Special Publications, 386.
- Chalmers, G.R.L. and Bustin, R.M. 2007. The organic matter distribution and methane capacity of the Lower Cretaceous strata of northeastern British Columbia, *Int. J. Coal Geol.*, **70(1)**, 223–239.
- Chalmers, G.R., Bustin, R.M. and Power, I.M. 2012. Characterization of gas shale pore systems by porosimetry, pycnometry, surface area, and field emission scanning electron microscopy/transmission electron microscopy image analyses: Examples from the Barnett, Woodford, Haynesville, Marcellus, and Doig units. *AAPG bulletin*, **96(6)**, 1099-1119.
- Charpentier, R.R. and Cook, T.A. 2011. USGS Methodology for Assessing Continuous Petroleum Resources. *U.S. Geological Survey Open-File Report*.

- Clarke, H., Eisner, L., Styles, P., and Turner, P. 2014. Felt seismicity associated with shale gas hydraulic fracturing: The first documented example in Europe. *Geophysical Research Letters*, **41(23)**, 8308-8314.
- Curtis, C.D. 1978. Possible links between sandstone diagenesis and depth-related geochemical reactions occurring in enclosing mudstones. *Jour. Geol. Soc. London*, **135(1)**, 107-117.
- Curtis, J.B. 2002. Fractured shale-gas systems. *AAPG bulletin*, **86(11)**, 1921-1938.
- Cuss, R.J., Wiseall, A.C., Hennissen, J.A.I., Waters, C.N., Kemp, S.J., Ougier-Simonin, A., Holyoake, S. and Haslam, R.B. 2015. Hydraulic-fracturing: a review of theory and field experience, *European M4ShaleGas Consortium*.
- Davies, J. R., Riley, N. J., and Wilson, D. 1989. The distribution of Chadian and earliest Arundian strata in North Wales: implications for Dinantian (Carboniferous) lithostratigraphy and palaeogeography. *Geological Journal*, **24(1)**, 31-47.
- Davies, S.J. 2008. The record of Carboniferous sea-level change in low-latitude sedimentary successions from Britain and Ireland during the onset of the late Paleozoic ice age. *Geological Society of America Special Papers*, **441**, 187-204.
- DECC, 2010. The unconventional hydrocarbon resources of Britain's onshore basins - shale gas. *DECC Promote website of December 2010*.
- De Pater, C.J. and Baisch, S. 2011. Geomechanical Study of Bowland shale seismicity, *synthesis report 57. Cuadrilla resources*.
- Dewhurst, D.N., Aplin, A.C. and Sarda, J.P. 1999a. Influence of clay fraction on pore-scale properties and hydraulic conductivity of experimentally compacted mudstones, *J. Geophys. Res.*, **104(B12)**, 29261–29274.

- Dewhurst, D.N., Yang, Y. and Aplin, A.C. 1999b. Permeability and fluid flow in natural mudstones, A.C. Aplin, A.J. Fleet, J.H.S. Macquaker (Eds.), *Muds and Mudstones: Physical and Fluid Flow Properties. Geological Society, London, Special Publications*, 125–136.
- EIA, (US) 2013. Technically recoverable shale oil and shale gas resources: an assessment of 137 shale formations in 41 countries outside the United States. *Report June 2013*.
- EIA, (US) 2015a. Technically recoverable shale oil and shale gas resources: United Kingdom. *Report September 2015*.
- EIA, (US) 2015b. *Annual Energy Outlook 2015. Department of Energy*.
- Eisner, L., Janská, E. , Opršal, I. and Matoušek, P. 2011. Seismic analysis of the events in the vicinity of the Preese Hall well, *Report from Seismik to Cuadrilla Resources Ltd*.
- Evans, M.A. 1995. Fluid inclusions in veins from the Middle Devonian shales: A record of deformation1 conditions and fluid evolution in the Appalachian Plateau. *Geological Society of America Bulletin*, **107(3)**, 327-339.
- Evans, D.J., and Kirby, G.A. 1999. The architecture of concealed Dinantian carbonate sequences over the Central Lancashire and Holme highs, northern England. *Proceedings of the Yorkshire Geological Society*, **52(3)**, 297-312.
- Fischer, M.P., Higuera-Díaz, I.C., Evans, M.A., Perry, E.C. and Lefticariu, L. 2009. Fracture-controlled paleohydrology in a map-scale detachment fold: Insights from the analysis of fluid inclusions in calcite and quartz veins. *Journal of Structural Geology*, **31(12)**, 1490-1510.
- Fisher, D. and Byrne, T., 1987. Structural evolution of underthrust sediments, Kodiak Islands, Alaska. *Tectonics*, **6(6)**, 775-793.
- Fraser, A.J., and Gawthorpe, R. L. 2003. An Atlas of Carboniferous basin evolution in northern England. *Geological Society Memoir*, **28**, 79.

- Gale, J.F.W., Reed, R. M. and Holder, J. 2007. Natural fractures in the Barnett Shale and their importance for hydraulic fracture treatments. *American Association of Petroleum Geologists Bulletin*, **91**(4), 603–622.
- Gale, J.F.W. and Holder, J. 2010. Natural fractures in some US shales and their importance for gas production. *Geological Society, London, Petroleum Geology Conference Series*, **7**, 1131-1140.
- Gawthorpe, R.L. 1987. Tectono-sedimentary evolution of the Bowland Basin, northern England, during the Dinantian. *Journal of the Geological Society (London)*, **144**(1), 59-71.
- Charpentier, R.R. and Cook, T.A. 2011. USGS Methodology for Assessing Continuous Petroleum Resources. U.S. *Geological Survey Open-File Report 2011*, 1167.
- Goult, N.R., Ramdhan, A.M. and Jones, S.J. 2012. Chemical compaction of mudrocks in the presence of overpressure. *Petroleum Geoscience*, **18**(4), 471-479.
- Gross, D., Sachsenhofer, R.F., Bechtel, A., Pytlak, L., Rupprecht, B. and Wegerer, E. 2015. Organic geochemistry of Mississippian shales (Bowland Shale Formation) in central Britain: Implications for depositional environment, source rock and gas shale potential, *Marine and Petroleum Geology*, **59**, 1-21.
- Gutierrez, M., Nygård, R., Høeg, K., and Berre, T. 2008. Normalized undrained shear strength of clay shales. *Engineering Geology*, **99**(1), 31-39.
- Hackley, P.C. and Cardott, B.J. 2016. Application of organic petrography in North American shale petroleum systems: a review, *International Journal of Coal Geology*, **163**, 8-51.
- Hammes, U., Hamlin, H.S. and Ewing, T.E., 2011. Geologic analysis of the Upper Jurassic Haynesville Shale in east Texas and west Louisiana. *AAPG bulletin*, **95**(10), 1643-1666.
- Hampson, G.J., Elliott, T., and Davies, S.J. 1997. The application of sequence stratigraphy to Upper Carboniferous fluvio-deltaic strata of the onshore UK and Ireland: implications for the southern North Sea. *Journal of the Geological Society*, **154**(4), 719-733.

- Ibanez, W.D., and Kronenberg, A.K. 1993. Experimental deformation of shale: Mechanical properties and microstructural indicators of mechanisms. *International journal of rock mechanics and mining sciences*, **30(7)**, 723-734.
- IGas, 2012. Results presentation and shale update. *Online presentation*.
www.igasplc.com/uploads/analystpresentationjune2012final.pdf.
- Jackson, J.A., Mehl, J.P., Neuendorf, K.K.E. and American Geological Institute 2007. *Glossary of geology*. In: Springer (ed.). American Geological Institute, Alexandria, Va.
- Jarvie, D.M., Hill, R.J., Ruble, T.E. and Pollastro, R.M. 2007. Unconventional shale gas systems: the Mississippian Barnett Shale of north-central Texas as one model for thermogenic shale gas assessment, *Am. Assoc. Pet. Geol. Bull.*, **91(4)**, 475–499.
- Jarvie, D.M. 2014. Components and processes affecting producibility and commerciality of shale resource systems, *Special Publication Geologica Acta*, **12(4)**, 307–325.
- Keller, L.M., Schwiedrzik, J.J., Gasser, P. and Michler, J. 2017. Understanding Anisotropic Mechanical Properties Of Shales At Different Length Scales: In-Situ Micropillar Compression Combined With Finite Element Calculations. *Journal of Geophysical Research: Solid Earth*.
- Lan, H., Martin, C.D. and Hu, B. 2010. Effect of heterogeneity of brittle rock on micromechanical extensile behavior during compression loading. *Journal of Geophysical Research: Solid Earth*, **115 (B1)**.
- Lash, G.G. and Engelder, T. 2005. An analysis of horizontal microcracking during catagenesis: Example from the Catskill delta complex. *AAPG bulletin*, **89(11)**, 1433-1449.
- Leckie, D.A., Singh, C., Goodarzi, F. and Wall, J.H. 1990. Organic-rich, radioactive marine shale: a case study of a shallow-water condensed section, Cretaceous Shaftesbury Formation, Alberta, Canada. *Journal of Sedimentary Research*, **60(1)**.

- Lee, H.P., Olson, J.E., Holder, J., Gale, J.F., and Myers, R.D. 2015. The interaction of propagating opening mode fractures with preexisting discontinuities in shale. *Journal of Geophysical Research: Solid Earth*, **120**(1), 169-181.
- Leeder, M.R. 1982. Upper Palaeozoic basins of the British Isles—Caledonide inheritance versus Hercynian plate margin processes. *Journal of the Geological Society*, **139**(4), 479-491.
- Leeder, M.R. 1988. Recent developments in Carboniferous geology: a critical review with implications for the British Isles and NW Europe. *Proceedings of the Geologists' Association*, **99**(2), 73-100.
- Loucks, R. G. and Ruppel, S. C. 2007. Depositional setting and lithofacies of the Mississippian Deepwater Barnett Shale in the Forth Worth Basin, Texas. *American Association of Petroleum Geologists Bulletin*, **91**(4), 579– 601.
- Ma, L., Taylor, K.G., Lee, P.D., Dobson, K.J., Dowey, P.J., and Courtois, L. 2016. Novel 3D centimetre-to nano-scale quantification of an organic-rich mudstone: The Carboniferous Bowland Shale, Northern England. *Marine and Petroleum Geology*, **72**, 193-205.
- Marquez, X.M., and Mountjoy, E.W. 1996. Microcracks due to overpressures caused by thermal cracking in well-sealed Upper Devonian reservoirs, deep Alberta basin. *AAPG Bulletin*, **80**(4), 570–588.
- Masri, M., Sibai, M., Shao, J.F. and Mainguy, M., 2014. Experimental investigation of the effect of temperature on the mechanical behaviour of Tournemire shale, *International Journal of Rock Mechanics and Mining Science*, **70**, 185-191.
- Maynard, J.R., Wignall, P.B. and Varker, W.J. 1991. A 'hot' new shale facies from the Upper Carboniferous of Northern England. *Journal of the Geological Society*, **148**(5), 805-808.
- Mckernan R., Mecklenburgh, J., Rutter, E. and Taylor, K.G. 2017. Microstructural controls on the pressure-dependent permeability of Whitby mudstone. In: (E. Rutter, J. Mecklenburgh and K.

- Taylor, eds) Geomechanical and Petrophysical Properties of Mudrocks, *Geological Society of London Special Publication*, **454**, doi:.org/10.1144/SP454 (in press).
- Milner, M., McLin, R. and Petriello, J. 2010. Imaging texture and porosity in mudstones and shales: Comparison of secondary and ion-milled backscatter SEM methods. In *Canadian Unconventional Resources and International Petroleum Conference*. Society of Petroleum Engineers.
- Montgomery, S.L., Jarvie, D.M., Bowker, K.A., and Pollastro, R.M. 2005. Mississippian Barnett Shale, Fort Worth basin, north-central Texas: Gas-shale play with multi-trillion cubic foot potential. *AAPG bulletin*, **89(2)**, 155-175.
- Naumann, M., Hunsche, U. and Schulze, O. 2007. Experimental investigations on anisotropy in dilatancy, failure and creep of Opalinus Clay. *Physics and Chemistry of the Earth, Parts A/B/C*, **32(8)**, 889-895.
- Niandou, H., Shao, J.F., Henry, J.P. and Fourmaintraux, D. 1989. Laboratory Investigation of the mechanical behaviour of Tournemire shale, *International Journal of Rock Mechanics and Mining Science*, **34(1)**, 3-16.
- Oberlin, A. and Couty, R. 1970. Conditions of kaolinite formation during alteration of some silicates by water at 200 C. *Clays and Clay minerals*, **18**, 347-356.
- Ougier-Simonin, A., and Renard, F. 2016. Microfracturing and microporosity in shales, *Earth Science Reviews*, **162**, 198-226.
- Ozkaya, I. 1988. A simple analysis of oil-induced fracturing in sedimentary rocks. *Marine and Petroleum Geology*, **5(3)**, 293-297.
- Passey, Q.R., Bohacs, K.M., Esch, W.L., Klimentidis, R. and Sinha, S. 2010. From Oil-Prone Source Rock to Gas-Producing Shale Reservoir - Geologic and Petrophysical. Characterization

- of Unconventional Shale Gas Reservoirs. *Petroleum Engineers Unconventional Gas Conference*, Pittsburgh, Pennsylvania.
- Perri, F. 2008. Clay mineral assemblage of the Middle Triassic-Lower Jurassic mudrocks from Western-Central Mediterranean Alpine Chains. *Periodico di Mineralogia*, **77**, 23-40.
- Perri, F., Cirrincione, R., Critelli, S., Mazzoleni, P. and Pappalardo, A. 2008. Clay mineral assemblages and sandstone compositions of the Mesozoic Longobucco Group (north-eastern Calabria): implication for burial history and diagenetic evolution. *International Geology Review*, **50**, 1116-1131.
- Perri F., Caracciolo L., Cavalcante F., Corrado S., Critelli S., Muto F. and Dominici R. 2016. Sedimentary and thermal evolution of the Eocene-Oligocene mudrocks from the southwestern Thrace Basin (NE Greece). *Basin Research*, **28**, 319-339.
- Raji, M., Grocke, D., Greenwell, H.C., Gluyas, J.G. and Cornford, C. 2015. The effect of interbedding on shale reservoir properties. *Marine and Petroleum Geology*, **67**, 154-169.
- Rouchet (du), J. 1981. Stress fields, a key to oil migration, *AAPG Bulletin*, **65**(1), 445–459.
- Ross, D.J.K. and Bustin, R.M. 2007. Shale gas potential of the Lower Jurassic Gordondale Member, northeastern British Columbia, Canada, *Bull. Can. Pet. Geol.*, **55**(1), 51–75.
- Ross, D.J.K, and Bustin, R.M. 2008. Characterizing the shale gas resource potential of Devonian–Mississippian strata in the Western Canada sedimentary basin: Application of an integrated formation evaluation. *AAPG bulletin*, **92**(1), 87-125.
- Rossi, C., Kalin, O., Arribas, J., Tortosa, A. 2002. Diagenesis, provenance and reservoir quality of Triassic Tagi sandstones from Ourhoud Field, Berkine (Ghadames) Basin, Algeria. *Marine and Petroleum Geology*, **19**, 117- 142.
- Rutter, E. H., Mecklenburgh, J. and Taylor, K. G. 2017. Geomechanical and petrophysical properties of mudrocks: introduction In: Rutter, E. H., Mecklenburgh, J. & Taylor, K. G.

- (eds) Geomechanical and Petrophysical Properties of Mudrocks. *Geological Society, London, Special Publications*, **454**.
- Rutter, E.H. and Mecklenburgh, J. 2017. Hydraulic conductivity of bedding-parallel cracks in shale as a function of shear and normal stress. In: Rutter, E.H., Mecklenburgh, J. & Taylor, K.G. (eds) Geomechanical and Petrophysical Properties of Mudrocks. *Geological Society, London, Special Publications*, **454**.
- Schieber, J., 1996. Early diagenetic silica deposition in algal cysts and spores: a source of sand in black shales? *Journal of Sedimentary Research*, **66**(1).
- Schieber, J., Krinsley, D. and Riciputi, L. 2000. Diagenetic origin of quartz silt in mudstones and implications for silica cycling. *Nature*, **406**(6799), 981-985.
- Sone, H. and Zoback, M.D. 2013. Mechanical properties of shale-gas reservoir rocks—Part 1: Static and dynamic elastic properties and anisotropy. *Geophysics*, **78** (5), D381-392.
- Spears, D.A. 1980. Towards a classification of shales. *Journal of the Geological Society*, **137**(2), 125-129.
- Spears, D.A. and Amin, M.A. 1981. Geochemistry and mineralogy of marine and non-marine Namurian black shales from the Tansley borehole. *Sedimentology*, **28**(3), 407-417.
- Spencer, C. W. 1987. Hydrocarbon generation as a mechanism for overpressuring in Rocky Mountain region. *AAPG Bulletin*, **71**(4), 368–388.
- Stoneley, R. 1983. Fibrous calcite veins, overpressures, and primary oil migration. *AAPG Bulletin*, **67**(9), 1427-1428.
- Talukdar, S., Gallango, O., Vallejos, C., and Ruggiero, A. 1987. Observations on the primary migration of oil in the La Luna source rocks of the Maracaibo Basin, Venezuela. *B. Doligez, Eds., Migration of hydrocarbons in sedimentary basins: Paris, Editions Technip*, 59–78.

- Tieh, T.T., Berg, R.R., Popp, R.K., Brasher, J.E. and Pike, J.D. 1986. Deposition and diagenesis of upper Miocene arkoses, Yowlumne and Rio Viejo fields, Kern County, California. *AAPG Bulletin*, **70(8)**, 953-969.
- U.S. Energy Information Administration (USEIA) 2011. World Shale Gas Resources: an initial assessment of 14 regions outside the United States. *Report prepared by Advanced Resources International Inc.* www.eia.gov/analysis/studies/worldshalegas/.
- Warpinski, N.R. and Teufel, L.W. 1987. Influence of geologic discontinuities on hydraulic fracture propagation. *Journal of Petroleum Technology*, **39(02)**, 209–220.
- Warr, L.N. 2000. The Variscan Orogeny: The welding of Pangea, in Woodcock, N. and Strachan, R. eds, *Geological History of Britain and Ireland*: Blackwell, Oxford, 271–391.
- Waters, C.N., Glover, B.W., and Powell, J.H. 1994. Structural synthesis of S Staffordshire, UK: implications for the Variscan evolution of the Pennine Basin. *Journal of the Geological Society*, **151(4)**, 697-713.
- Waters, C.N. and Davies, S.J. 2006. Carboniferous: extensional basins, advancing deltas and coal swamps. *The geology of England and Wales/edited by PJ Brenchley and PF Rawson. London: Geological Society of London 2006*, 173-223.
- Waters, C.N., Waters, R.A., Barclay, W.J. and Davies, J.R. 2009. A lithostratigraphical framework for the Carboniferous successions of southern Great Britain (onshore). *British Geological Survey Research Report RR/09/01*.
- Waters, C.N. and Condon, D.J. 2012. Nature and timing of Late Mississippian to MidPennsylvanian glacio-eustatic sea-level changes of the Pennine Basin, UK. *Journal of Geological Society*, **169(1)**, 37-51.

Figure captions

Fig. 1. Location of the Preese Hall-1 borehole in: (a) the United Kingdom and (b) the Bowland Basin (adapted from Evans & Kirby 1999; mapsofworld 2015).

Fig. 2. Bowland basin stratigraphy in the Preese Hall-1 borehole, showing the stratigraphic locations of the samples studied, which lie within the Bowland-Hodder group.

Fig. 3. XRD patterns corresponding to the samples (a) B8 and (b) B5.

Fig. 4. (a) Variability of mineralogical composition of all samples, and (b) Mineralogy of all samples represented on a ternary diagram plotting proportions of clays, quartz and carbonates.

Fig. 5. Variability of mudstone micro-texture types of Bowland Shale from at the cm and mm scales : macroscopic views (a-f) and optical images (g-l).

Fig. 6. Variability of mudstone micro-texture types of Bowland Shale at the μm scale by back-scattered electron (BSE) images under SEM : (a,b) unlaminated quartz-rich mudstone, (c,d) weakly interlaminated calcite-rich mudstone, (e-i) interlaminated quartz-rich mudstone, (j-o) laminated quartz-rich mudstone. [Cal: calcite, Qz: quartz, Ank: ankerite, Om: organic matter, Qz: quartz, Pyr: pyrite, Cem: cement, Kaol: kaolinite, Alb: albite].

Fig. 7. Various types of organic matter particles in Bowland shale under SEM: (a) micrometric particles of organic matter without macropores (Om1-a); (b) micrometric particles of organic matter with macropores (Om1-b); (c) micrometric layers of organic matter (Om2); (d) Sub-micrometric organic matter particles in cement (Om3); (e) organic matter in oversize pores.

Fig. 8. SEM-BSE images of features attributable to fluid circulation in Bowland shale (examples from samples B6 and B8): (a) two veins of calcite perpendicular to bedding planes in sample B6; (b) fractures in vertical calcite vein in sample B6; (c) horizontal calcite vein in sample B8; (d) and (e) vertical veins of calcite which cross organic Om1-a and Om2 in sample B8; (f) **close-up** of the organic matter in (e). [Cal: calcite, Qz: quartz].

Fig. 9. SEM BSE images of (a) micrometric chlorite and altered albite on the boundaries of a calcite vein ; (b) well-shaped micrometric chlorite on the boundary of a calcite vein. [Chl: chlorite, Alb: albite, Qz: quartz, om :organic matter].

Fig. 10. SEM BSE images of (a) rutile inclusions in a calcite vein perpendicular to bedding planes in B8 at low magnification; (b) enlarged area of a) at high magnification ; (c) detrital rutile grain [Chl: chlorite, Alb: albite, Qz: quartz].

Fig. 11. (a) Randomly orientated kaolinite and muscovite mixed with albite and quartz; (d) large crystalline assemblage of kaolinite with phosphate inclusions in the quartz-rich laminae of B8. [Kaol: kaolinite, Alb: albite, Mus: muscovite, Cal: calcite, Qz: quartz, om: organic matter].

Fig. 12. SEM BSE images of: (a) well-formed ankerite crystallites in the quartz cement of B1; (b) ankerite crossing calcite vein in B6 sample ; (c) magnified view of of b) ; (d) quartz cement crossing well-formed ankerite crystallites and a calcite vein in B6 . [Kaol: kaolinite, Ank: ankerite, Mus: muscovite, Cal: calcite, Qz: quartz, Cem: cement].

Fig. 13. Fractures (arrows) in Bowland shale. BSE images of : (a) calcite-sealed fracture F1; (b) horizontal bitumen-filled fracture (F2) and empty fracture (F4) along F2; (c) assemblage of thin F2; (d) horizontal and vertical F2; (e) F1 crossed by a bitumen-filled and empty fractures ; (f) inclined F2 crossing F1 corresponding to the magnified view of (e); (g) vertical empty fracture in F1 in the continuity of F2; (h) resin-filled fractures (F3); (i) empty fractures along organic matter and micas; (j) empty fractures at the extremities of organic matter particles (Om3) in quartz cement.

Table 1. Mineral proportion obtained by X-Ray Diffraction and Total Organic Content measurements for all samples (1 : Pendleide limestone, 2 : Worston shale).

Figure1

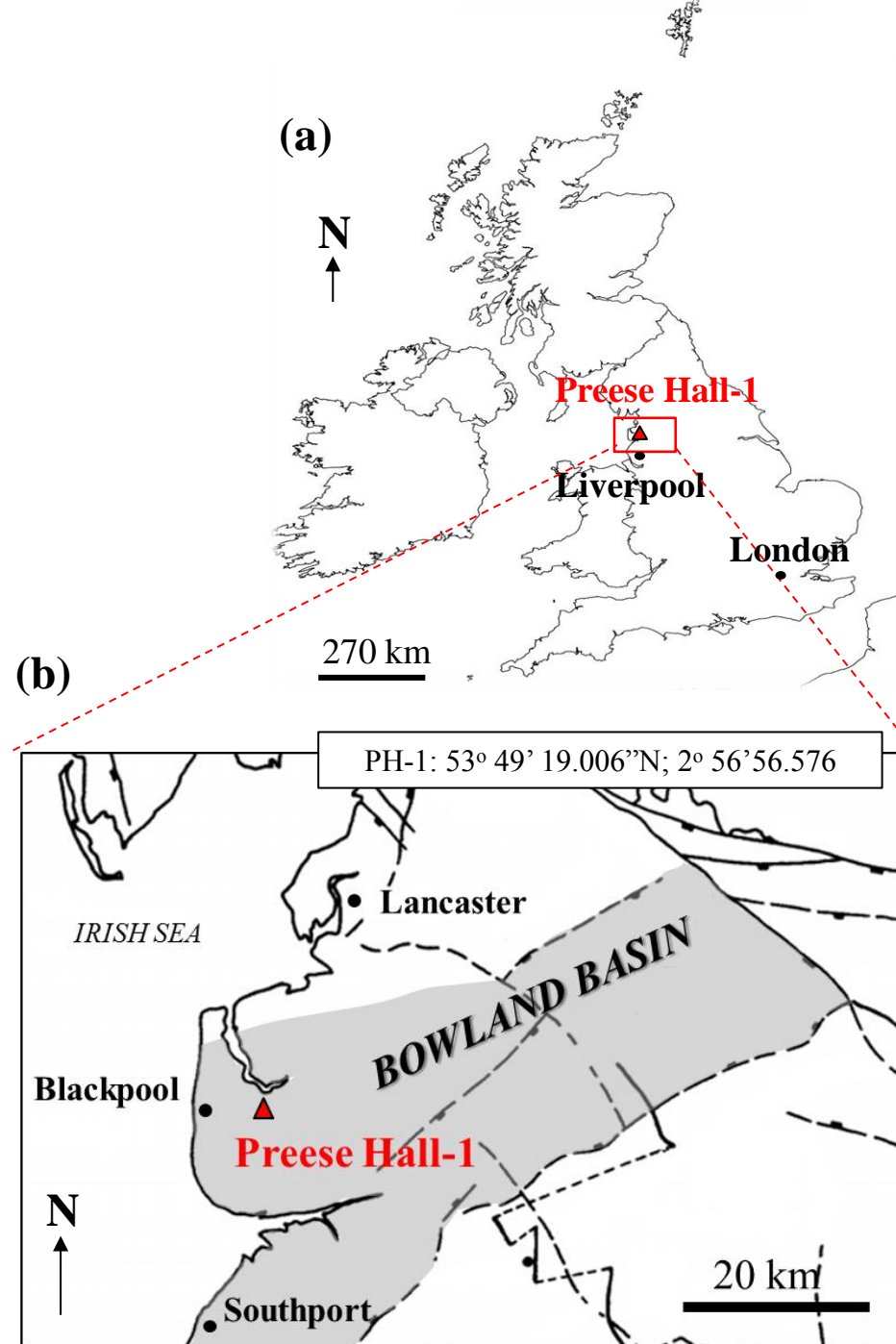


Figure2

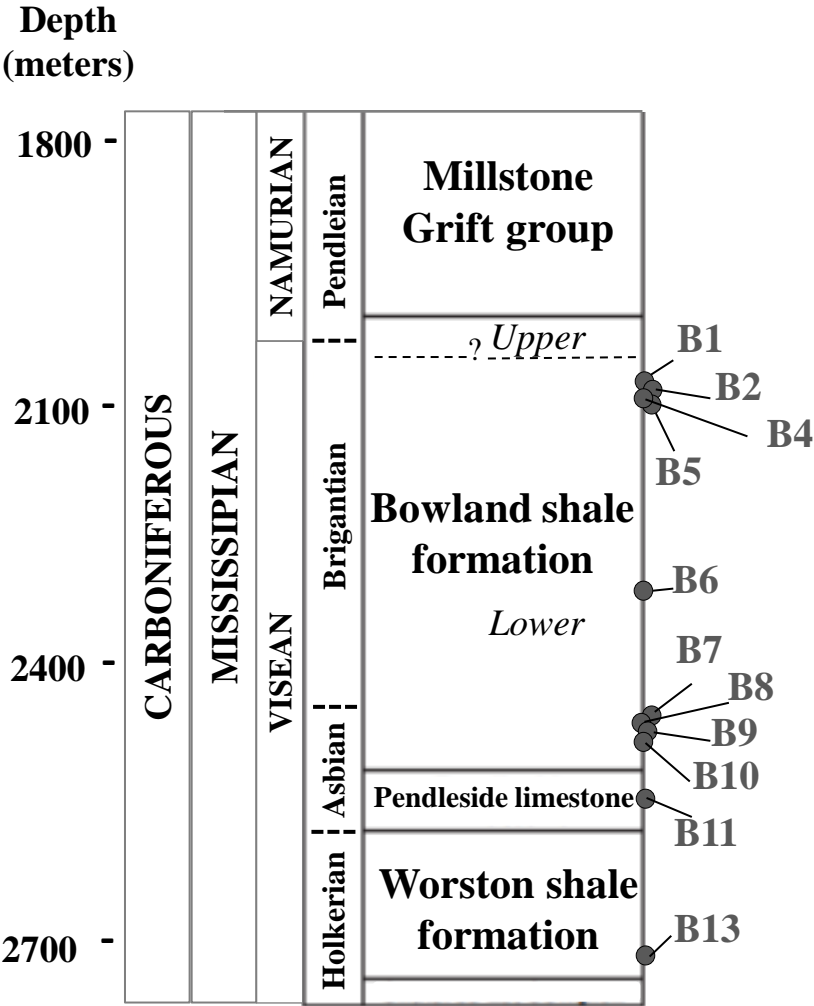


Figure3

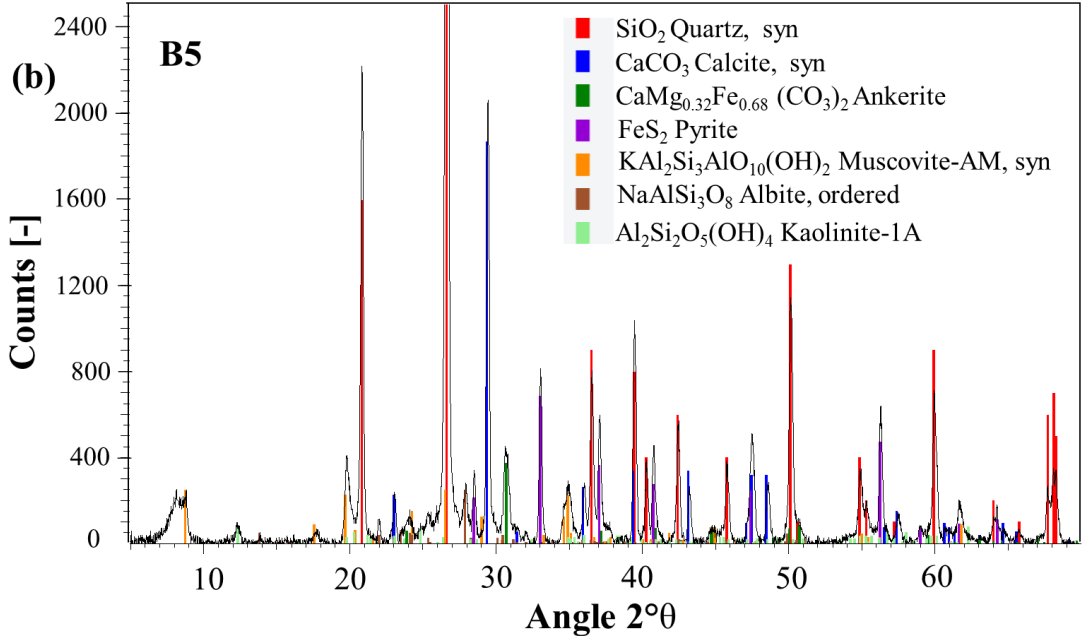
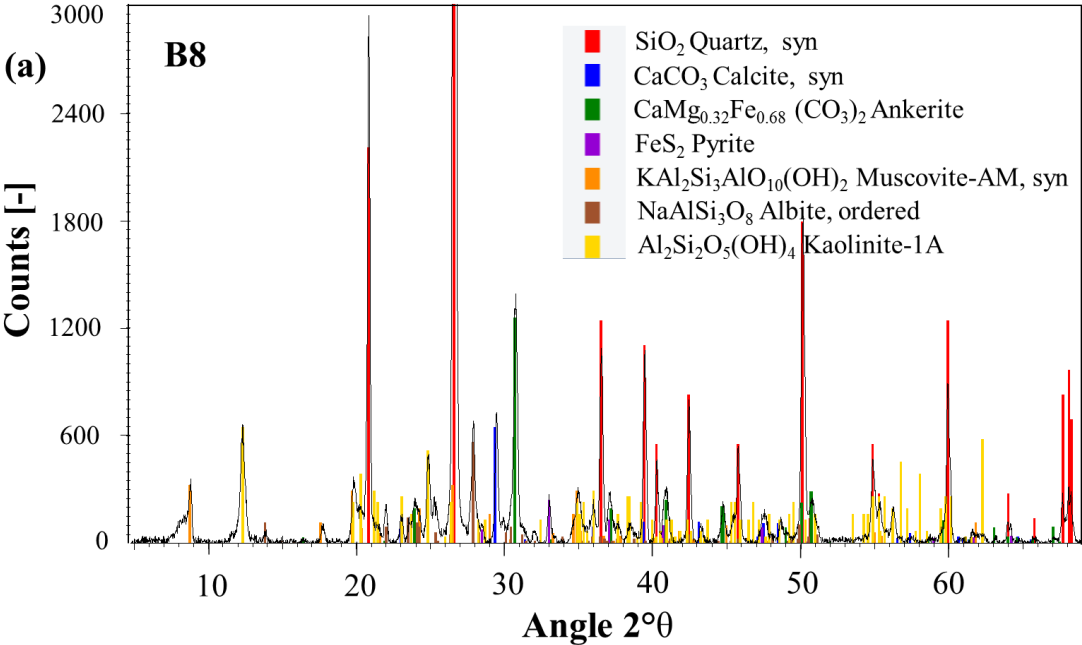


Figure4

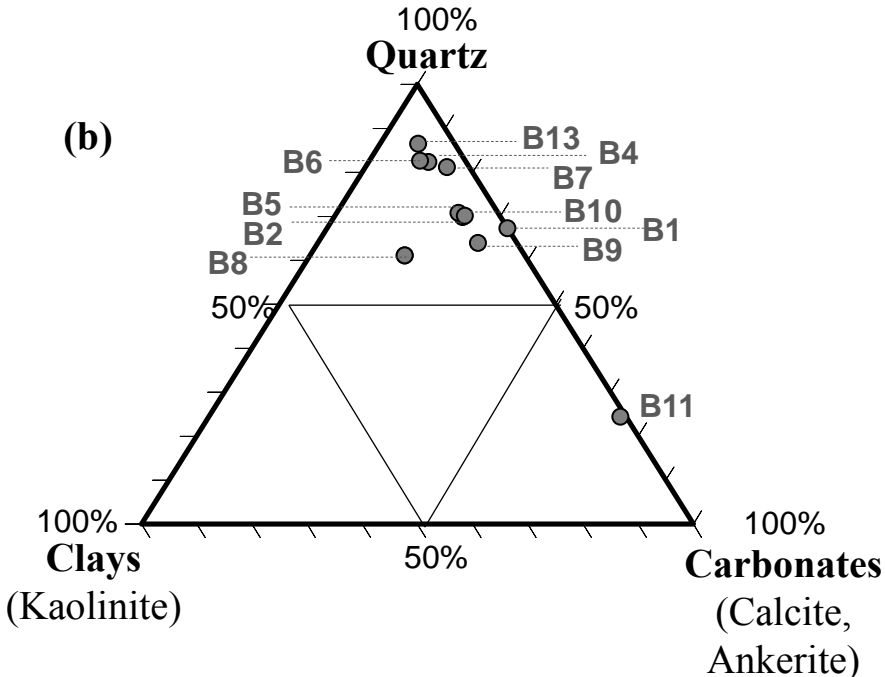
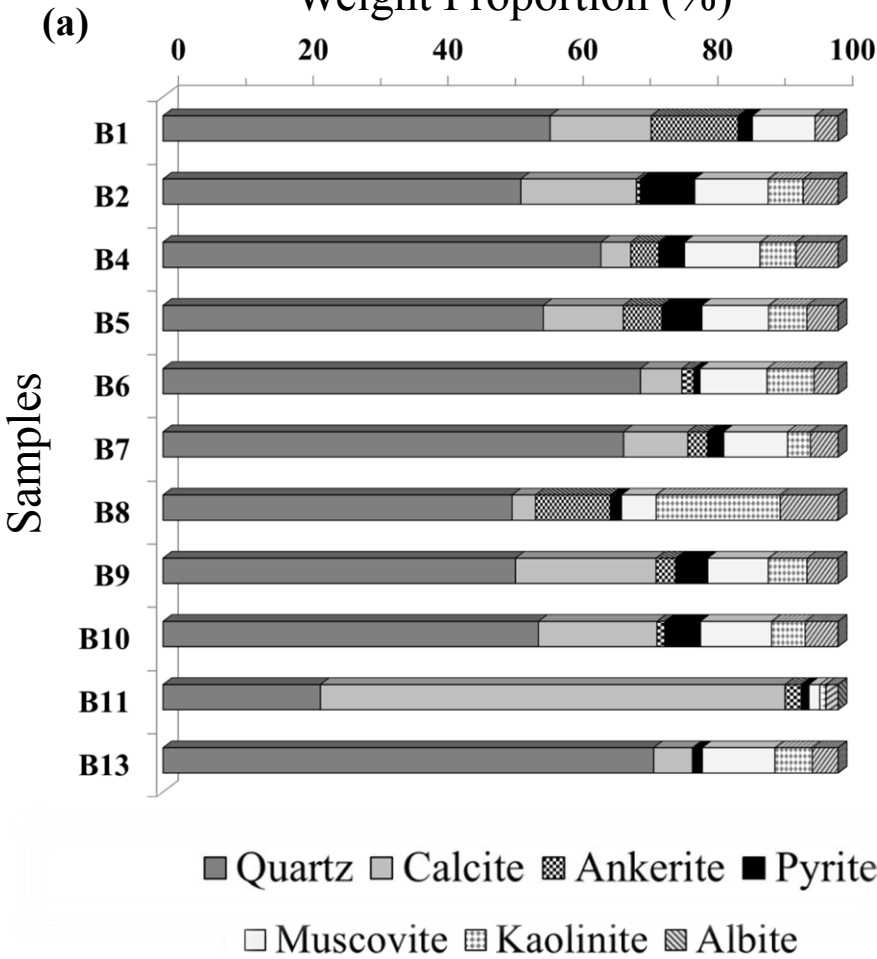
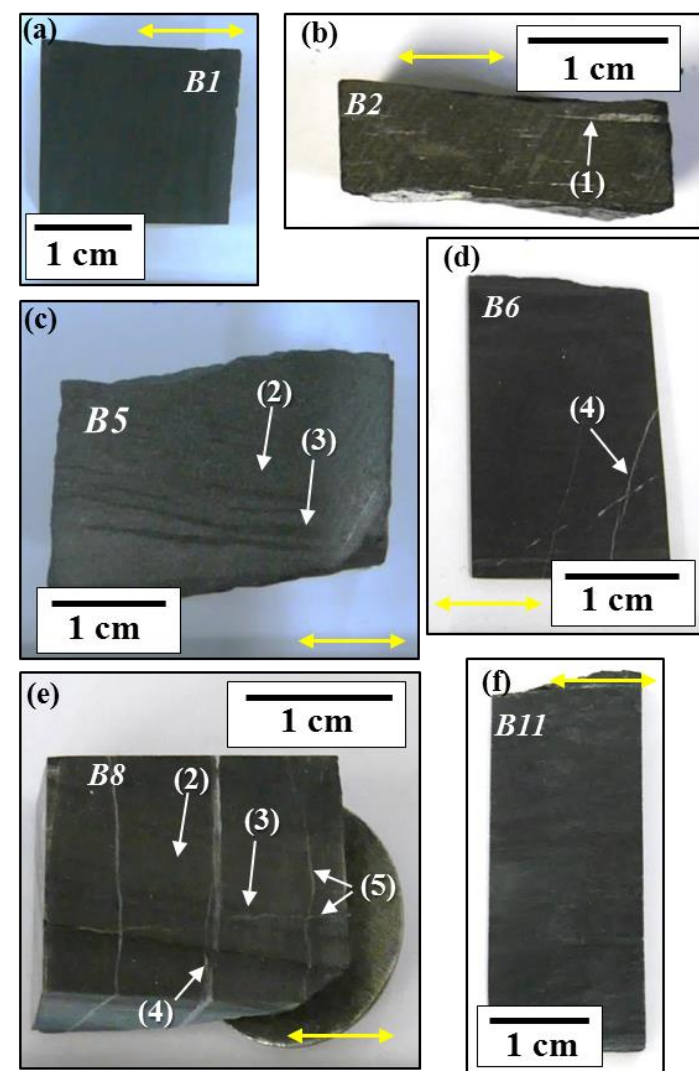
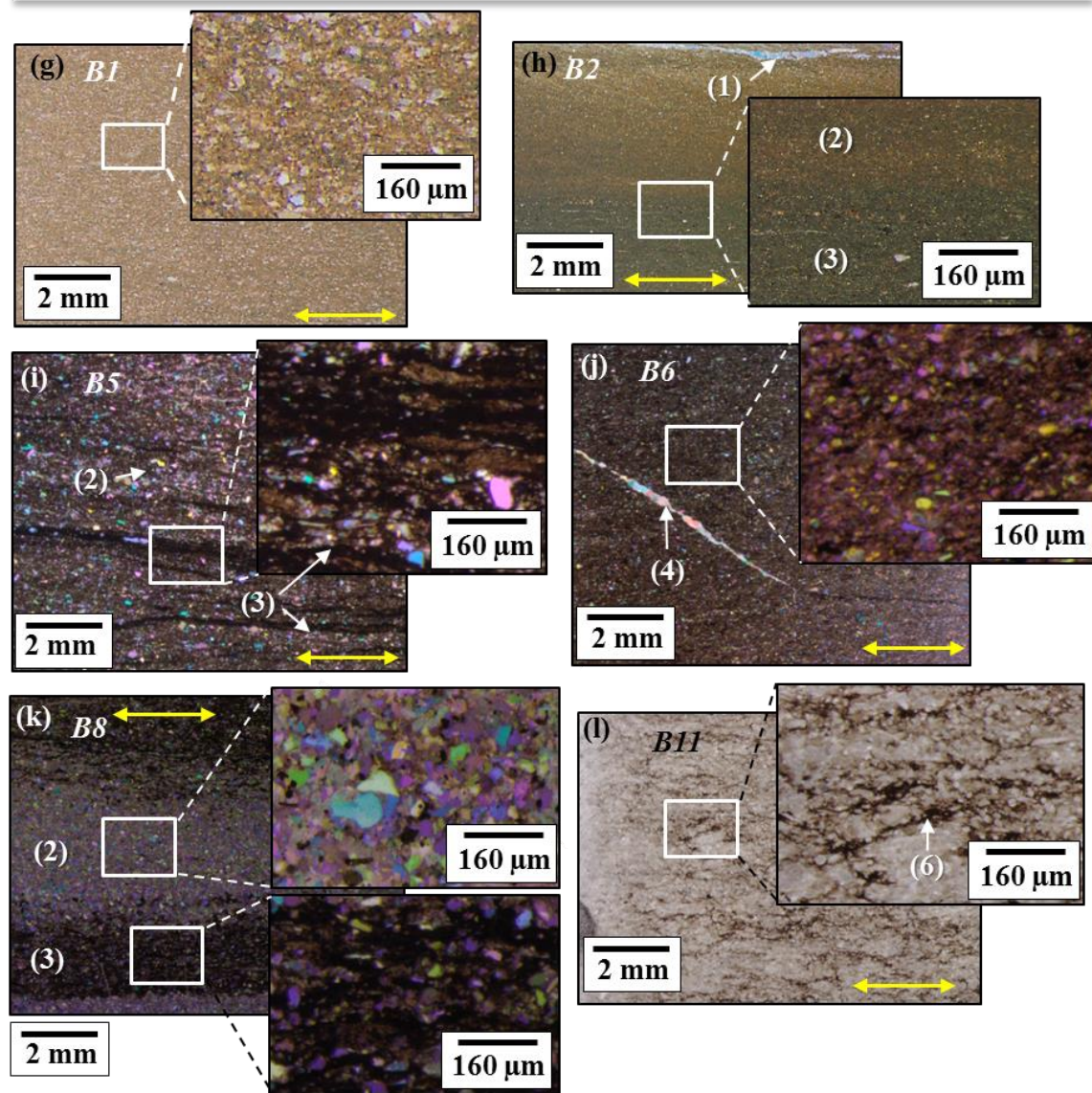


Figure5

Centimetre scale



Millimetre scale



- (1) Cluster of carbonates
- (2) Quartz-rich lamina
- (3) Organic and pyrite-rich lamina
- (4) Calcite vein
- (5) Empty fractures
- (6) Pyrite-rich lamina


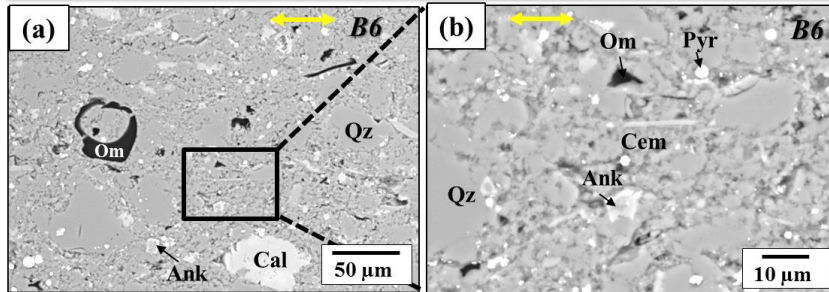
 Trace of bedding planes

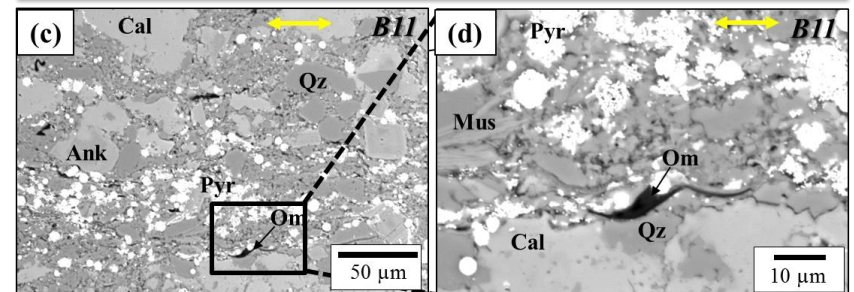
Figure6

Micrometre scale

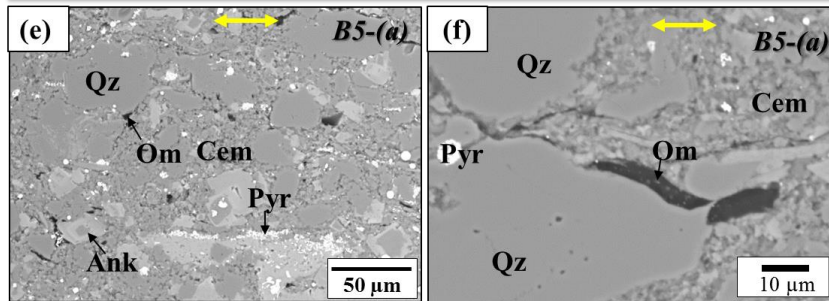
Unlaminated quartz-rich mudstone



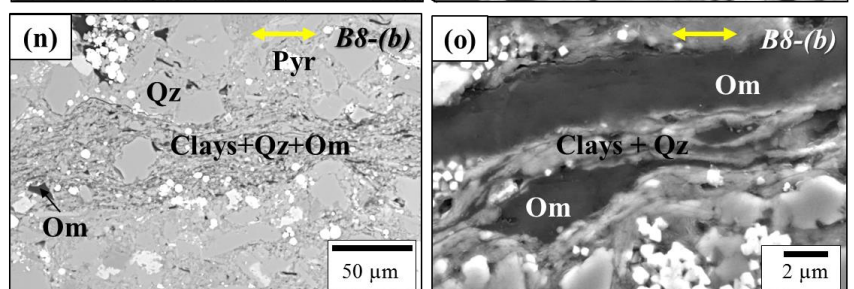
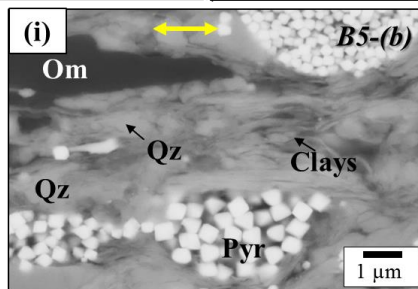
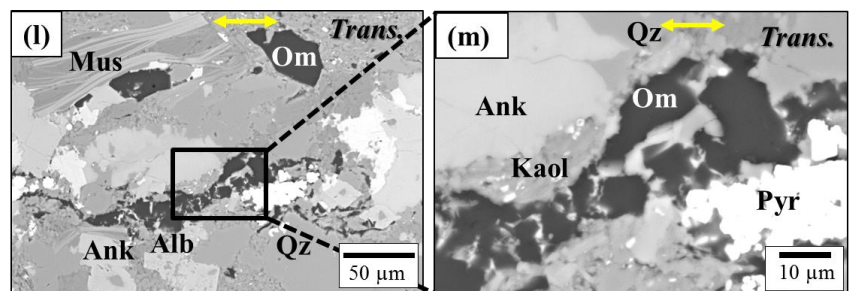
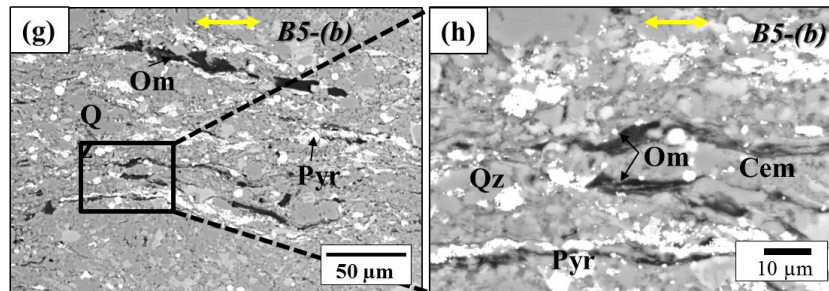
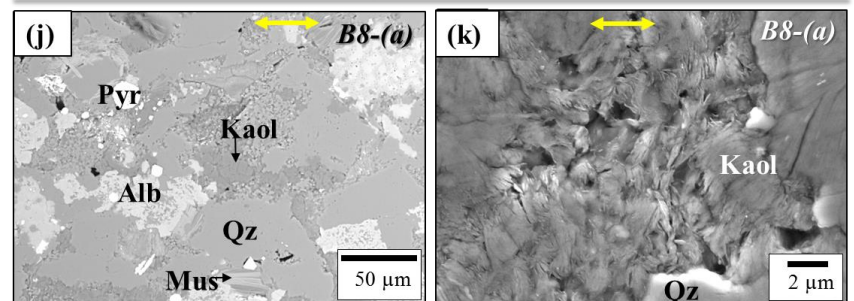
Weakly interlaminated calcite-rich mudstone



Interlaminated quartz-rich mudstone



Laminated quartz-rich mudstone



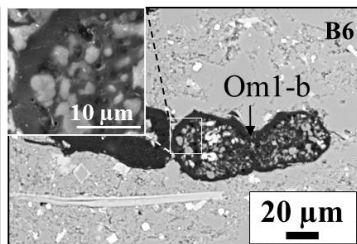
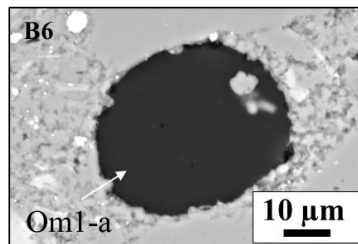
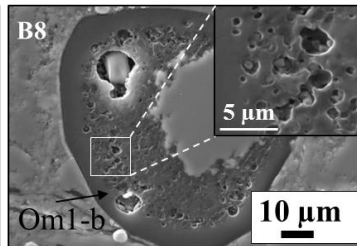
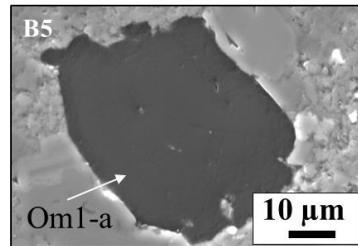
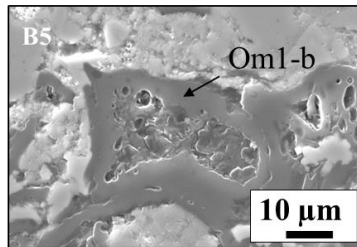
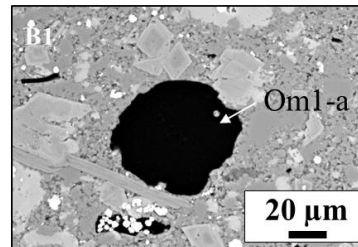
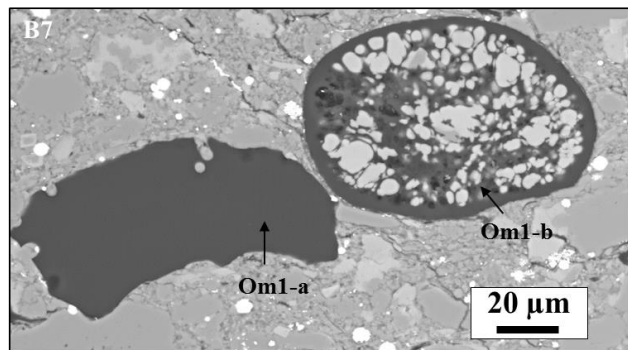
Trace of bedding planes

Figure 7

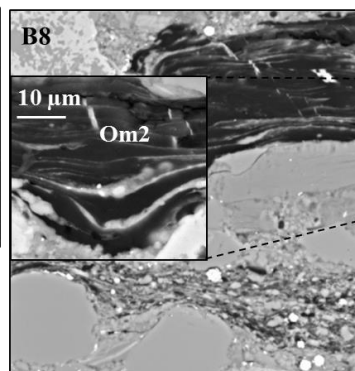
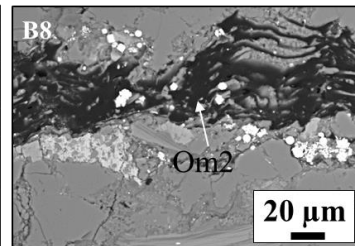
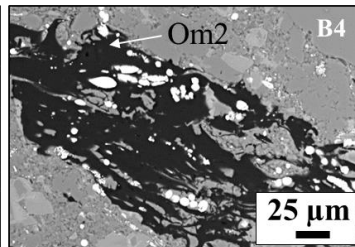
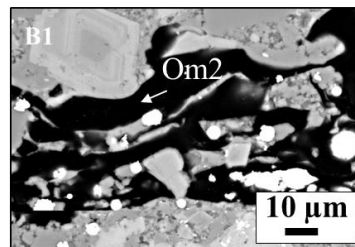
Om1 : Micrometre particles

(a) *Om1-a : without macropores*

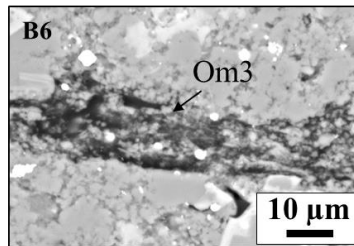
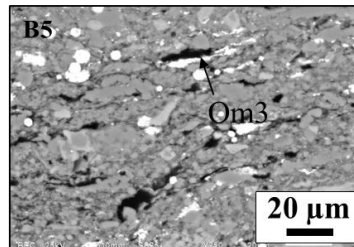
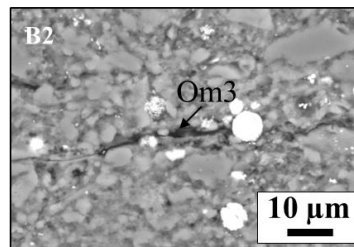
(b) *Om1-b : with macropores*



(c) **Om2 : Micrometre layer**



(d) **Om3 : Particles < μm in cement and clays**



(e) **Om4 : in oversize pores**

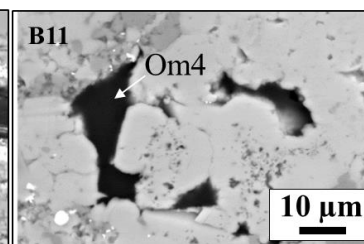
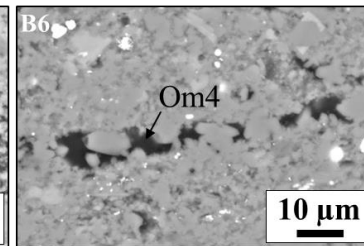
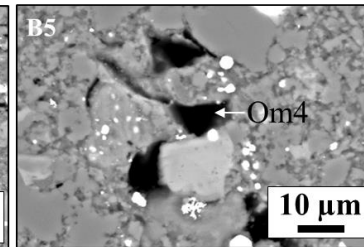
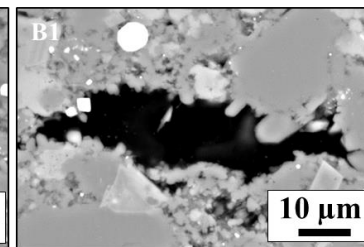


Figure8

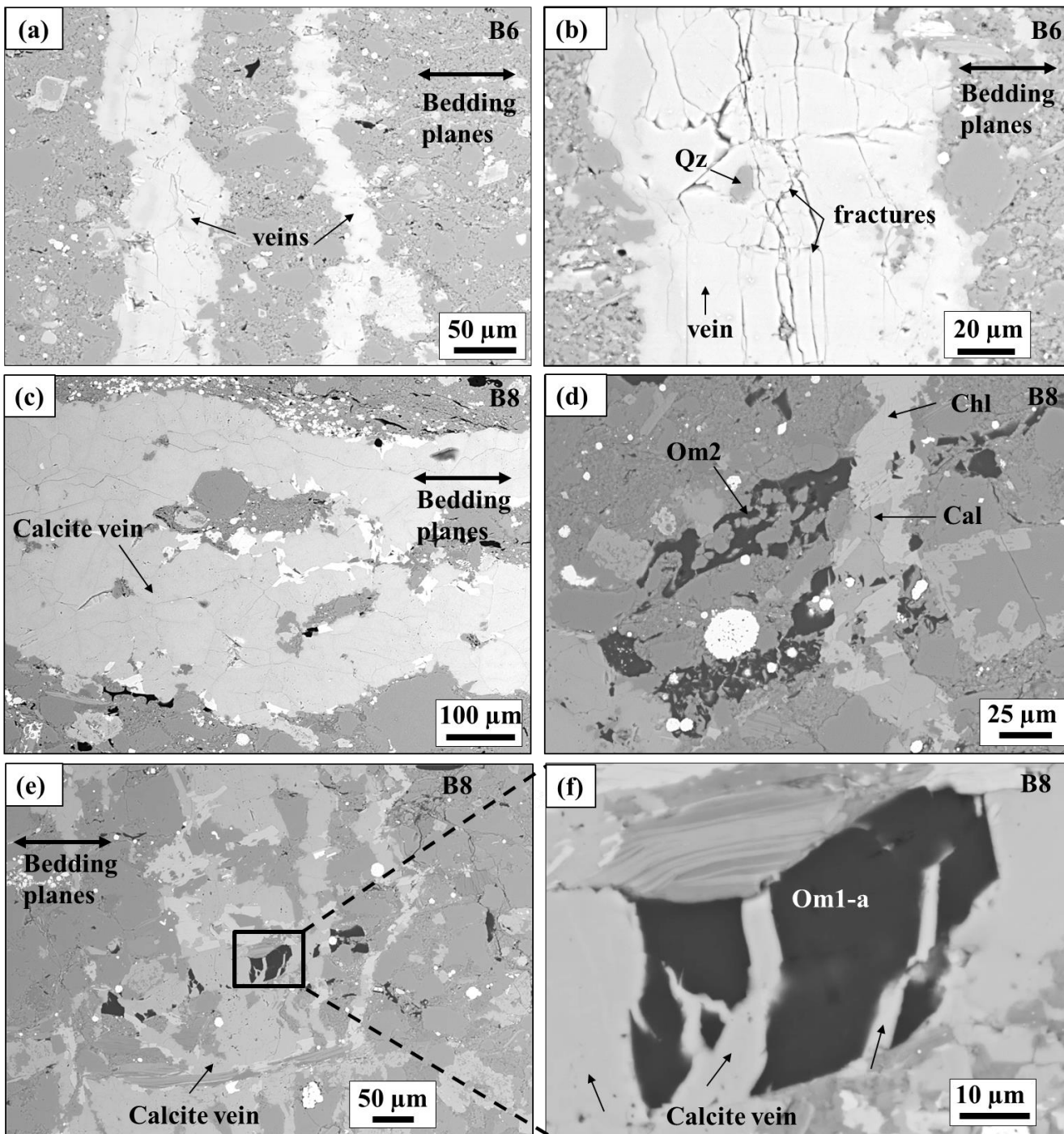


Figure9

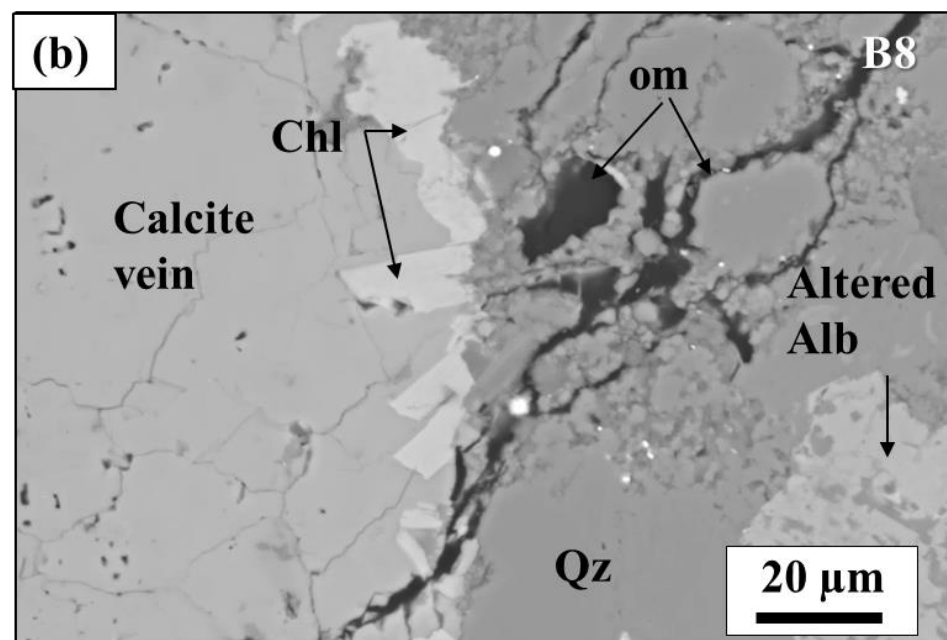
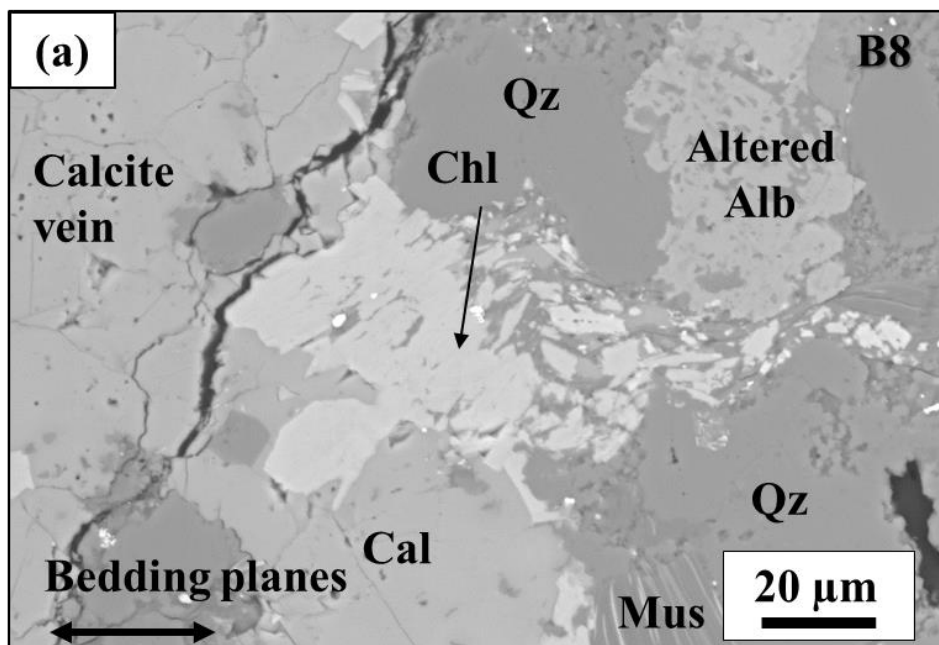


Figure10

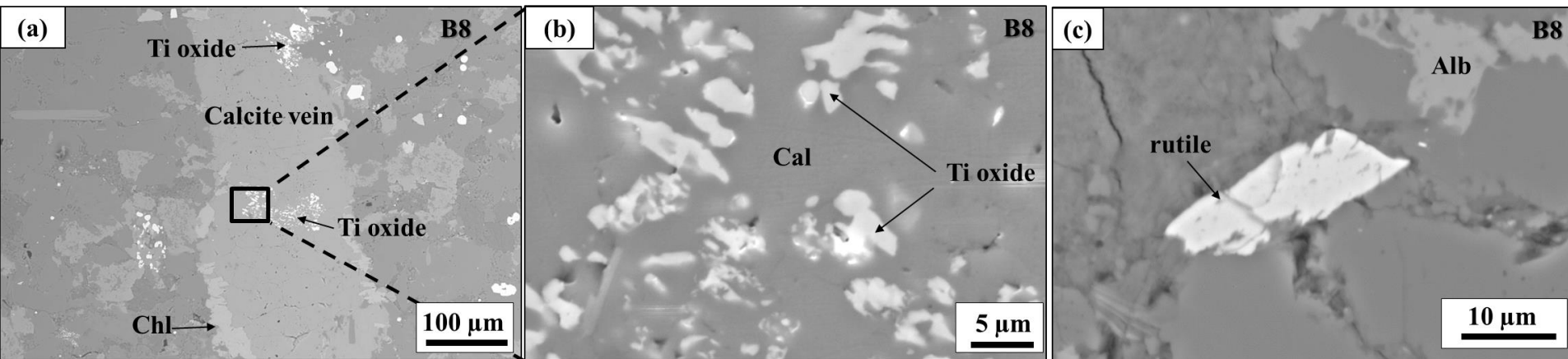


Figure11

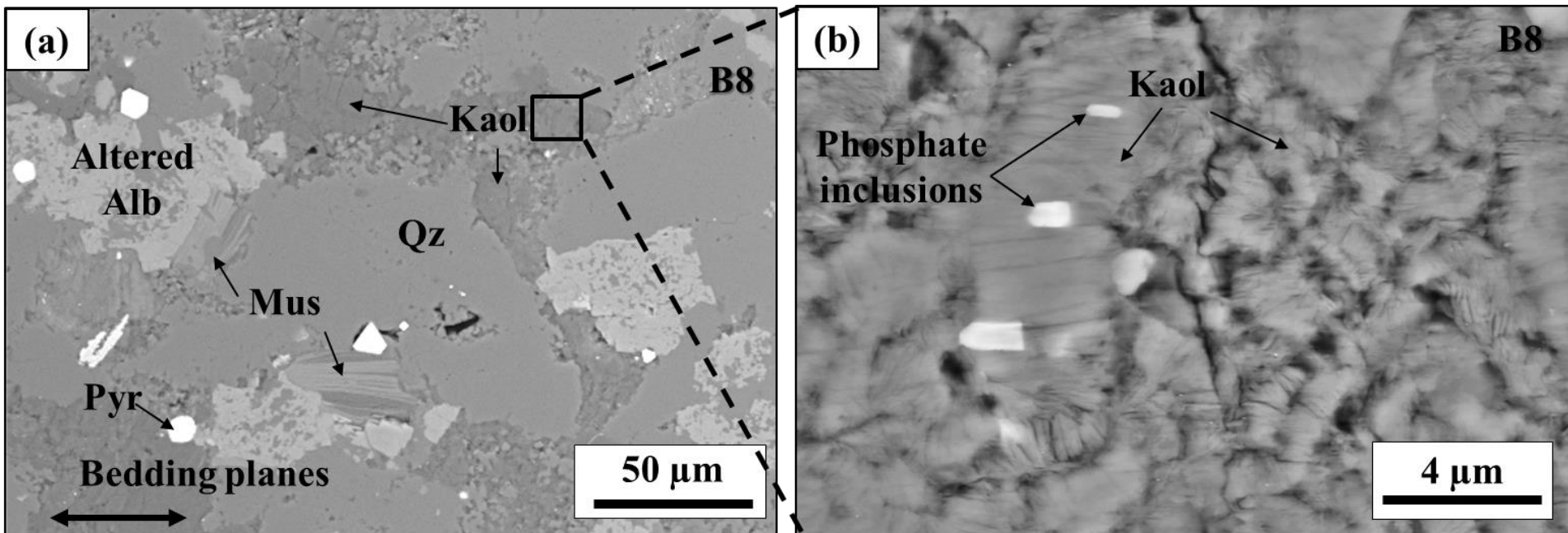


Figure12

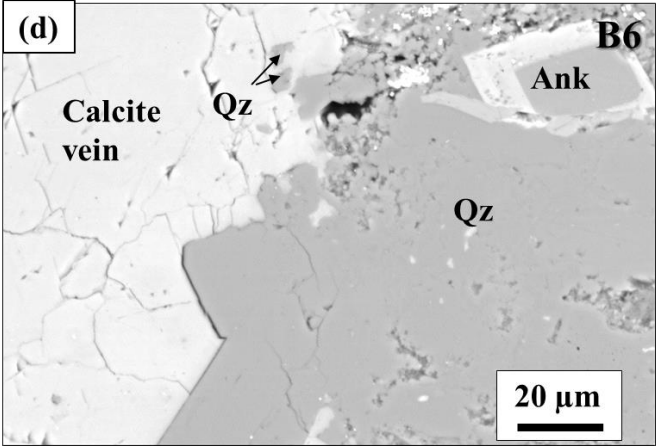
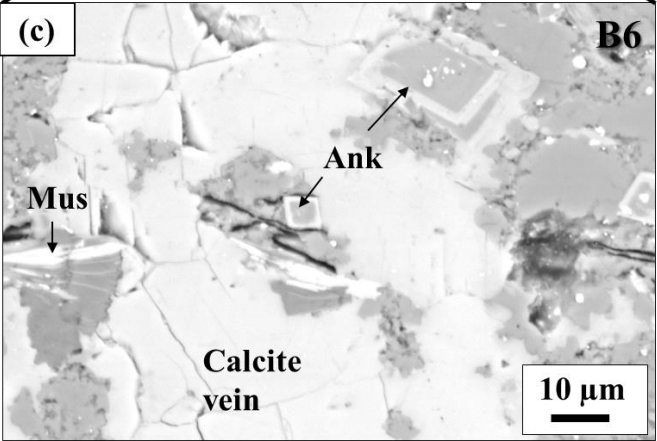
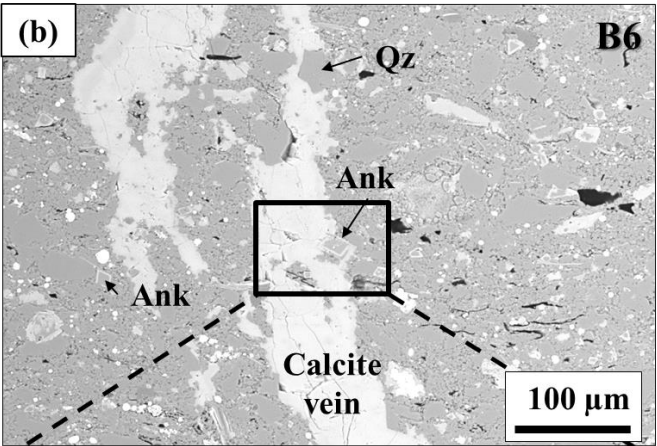
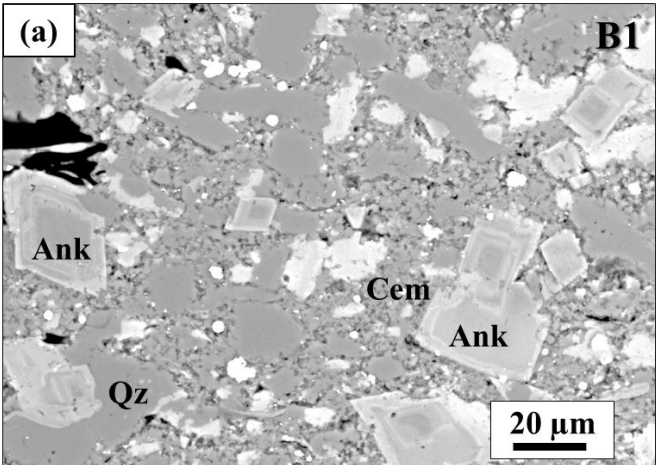


Figure13

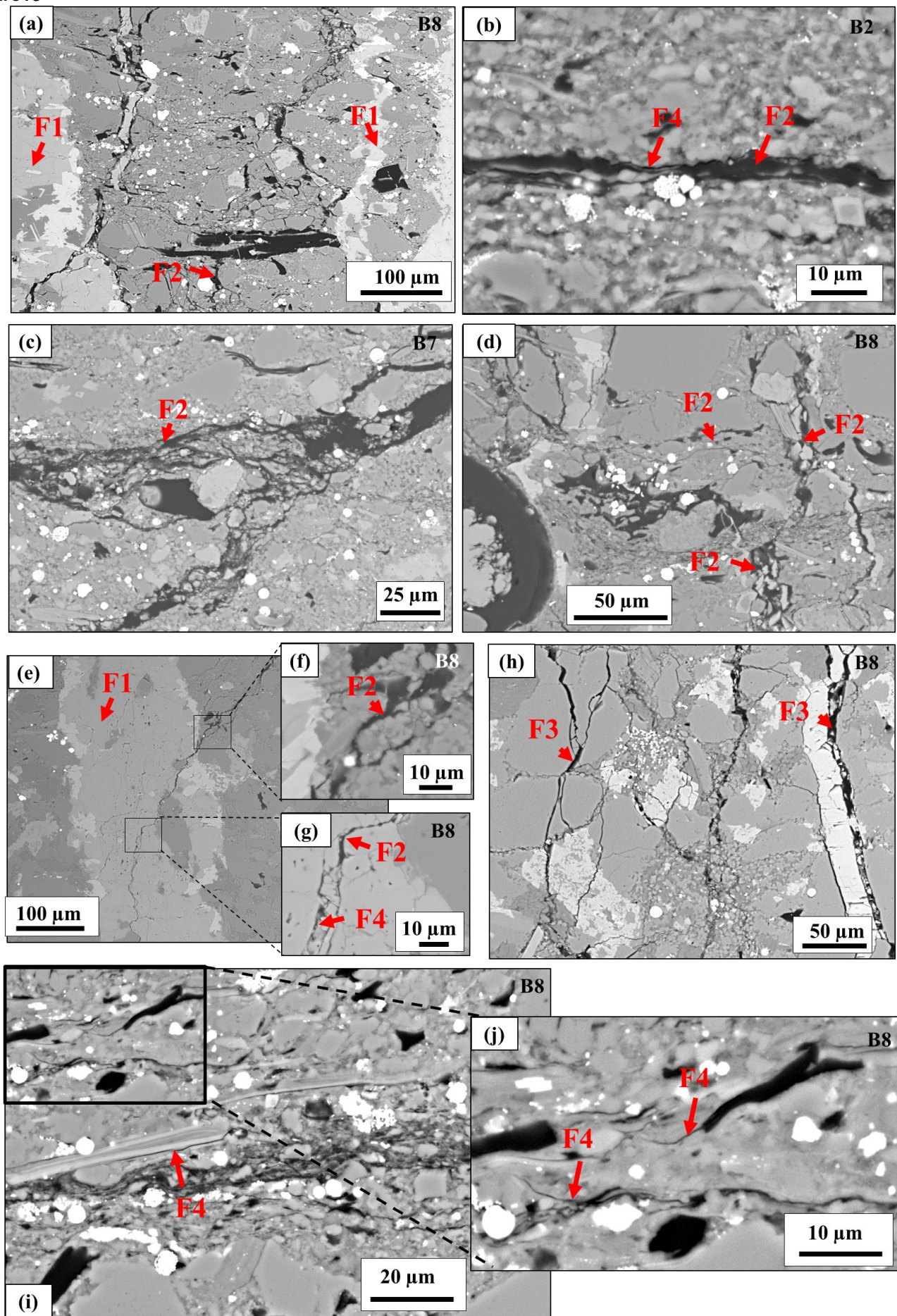


Table1

1

				Proportions (wt%)								
		Samples	Depth (meters)	Facies	Kaolinite	Quartz	Calcite	Ankerite	Pyrite	Muscovite	Albite	TOC
Bowland-Hodder unit	Lower Bowland shale	B1	2073.34	Unlaminated quartz-rich	0	58	15	13	2	9	3	1.4
		B2	2081.27	Transition un- to interlaminated quartz-rich	5	53	17	1	8	11	5	4.1
		B4	2089.83	Unlaminated quartz-rich	5	65	4	5	4	11	6	1.7
		B5	2091.69	Interlaminated quartz-rich	6	56	12	6	6	10	4	3.2
		B6	2344.70	Unlaminated quartz-rich	7	71	6	2	1	10	3	6.1
		B7	2488.84	Interlaminated quartz-rich	3	68	10	3	2	10	4	1.5
		B8	2495.27	Laminated quartz-rich	18	52	3	11	2	5	9	1.1
		B9	2496.92	Unlaminated quartz-rich	6	52	21	3	5	9	4	2.1
		B10	2500.49	Unlaminated quartz-rich	5	56	18	1	5	10	5	2.0
	P.L ¹	B11	2586.29	Unlaminated Calcite-rich	1	23	69	2	1	2	2	0.5
W.S ²	B13	2710.40	-	5	73	6	0	1	11	4	5.6	

2

3